

Simula SpringerBriefs on Computing 13

Reports on Computational Physiology

Kimberly J. McCabe *Editor*



Computational Physiology

Simula Summer
School 2022 – Student
Reports

simula

OPEN ACCESS



Springer

Simula SpringerBriefs on Computing

Reports on Computational Physiology

Volume 13

Series Editors

Kimberly J. McCabe Simula Research Laboratory, Oslo, Norway

Andrew D. McCulloch, Institute for Engineering in Medicine, University of California San Diego, La Jolla, California, USA; Department of Bioengineering, University of California San Diego, La Jolla, California, USA

Managing Editor

Jennifer Hazen, Simula Research Laboratory, Oslo, Norway

Editor-in-Chief

Aslak Tveito, Simula Research Laboratory, Oslo, Norway

About this series

In 2016, Springer and Simula launched an Open Access series called the Simula SpringerBriefs on Computing. This series aims to provide concise introductions to the research areas in which Simula specializes: scientific computing, software engineering, communication systems, machine learning and cybersecurity. These books are written for graduate students, researchers, professionals and others who are keenly interested in the science of computing, and each volume presents a compact, state-of-the-art disciplinary overview and raises essential critical questions in the field.

Simula's focus on computational physiology has grown considerably over the last decade, with the development of multi-scale mathematical models of excitable tissues (brain and heart) that are becoming increasingly complex and accurate. This sub-series represents a new branch of the SimulaSpringer Briefs that is specifically focused on computational physiology. Each volume in this series will explore multiple physiological questions and the models developed to address them. Each of the questions will, in turn, be packaged into a short report format that provides a succinct summary of the findings and, whenever possible, the software used will be made publicly available.

Kimberly J. McCabe
Editor

Computational Physiology

Simula Summer School 2022 – Student
Reports

simula

 Springer

Preface

Since 2014, we have organized an annual summer school in computational physiology. The school starts in June each year and the graduate students spend two weeks in Oslo learning the principles underlying mathematical models commonly used in studying the heart and the brain. At the end of their stay in Oslo, the students are assigned a research project to work on over the summer. In August the students travel to the University of California, San Diego to present their findings. Each year, we have been duly impressed by the students' progress and we have often seen that the results contain the rudiments of a scientific paper.

Starting in the 2021 edition of the summer school, we have taken the course one step further and aim to conclude every project with a scientific report that passes rigorous peer review as a publication in this new series called *Simula SpringerBriefs on Computing – reports on computational physiology*.

One advantage of this course adjustment is that we have the opportunity to introduce students to scientific writing. To ensure the students get the best introduction in the shortest amount of time, we have commissioned a professional introduction to science writing by Nature. The students participate in a 2-day *Nature Masterclasses* workshop, led by two editors from Nature journals, in order to strengthen skills in high quality scientific writing and publishing. The workshop is tailored to publications in the field of computational physiology and allows students to gather real-time feedback on their reports.

We would like to emphasise that the contributions in this series are brief reports based on the intensive research projects assigned during the summer school. Each report addresses a specific problem of importance in physiology and presents a succinct summary of the findings (8-15 pages). We do not require that results represent new scientific results; rather, they can reproduce or supplement earlier computational studies or experimental findings. The physiological question under consideration should be clearly formulated, the mathematical models should be defined in a manner readable by others at the same level of expertise, and the software used should, if possible, be made publicly available. All reports in this series are subjected to peer-review by the other students and supervisors in the program.

We would like to express our gratitude for the very fruitful collaboration with Springer -Nature and in particular with Dr. Martin Peters, the Executive Editor for Mathematics, Computational Science and Engineering.

The editors of *Simula SpringerBriefs on Computing – reports on computational physiology*:

Oslo, Norway
December 2022

Kimberly J McCabe
Andrew D McCulloch
Jennifer L Hazen
Aslak Tveito

Acknowledgements

The Simula Summer School in Computational Physiology is a team effort, with many scientists contributing their time to give lectures and advise projects for the students. We would like to thank the lecturers and project advisors for their expertise and willing participation in the course: Dr. Hermenegild Arevalo, Dr. Gabriel Balaban, Dr. Jonas van den Brink, Dr. Francisco Contijoch, Dr. Cécile Daversin-Catty, Dr. Andrew Edwards, Dr. Ada Johanne Ellingsrud, Dr. Nickolas Forsch, Dr. Ingeborg Gjerde, Dr. Ilse van Herck, Dr. Glenn Lines, Dr. Molly Maleckar, Dr. Kimberly McCabe, Dr. Andrew McCulloch, Lena Myklebust, Oscar Odeigah, Dr. Marie Rognes, Dr. Joakim Sundnes, Dr. Aslak Tveito, Julie Uv, Dr. Daniela Valdez-Jasso, Dr. Samuel Wall, and Kei Yamamoto.

Administrative support for the school was provided by Dr. Kimberly McCabe, Dr. Nickolas Forsch, Dr. Rachel Thomas, Dr. Stian Engen, and Hanie Tampus. At UCSD, we received vital administrative support from Jennifer Stowe and Marlene San Pedro. Formatting support for this volume was provided by Dr. Jennifer Hazen.

The Simula Summer School in Computational Physiology is supported through the Simula-UiO-UCSD Research PhD Training Programme (SUURPh), an endeavour funded by the Norwegian Ministry of Education and Research. Additional financial support is derived from SIMENT, an INTPART mobility grant from the Norwegian Research Council. The school also received funding from Digital Life Norway (DLN) to support student mobility.

Contents

1	An Automated Cardiac Constitutive Modelling Framework with Evolutionary Strain Energy Functions	1
	Kristin Ludwicki*, Leto L Riebel*, Sophia Ohnemus*, Frida M E Westby, Nickolas Forsch, and Gabriel Balaban	
	* These authors contributed equally to this work	
1.1	Introduction	2
1.2	Methods	3
1.2.1	Basic Principles of Hyperelastic Continuum Mechanics ..	3
1.2.2	Representation of the Strain-Energy Functions as Function Trees	4
1.2.3	Fitting the Strain-Energy Functions to Experimental Data	6
1.2.4	Evolutionary Symbolic Regression Algorithm	7
1.3	Results	11
1.3.1	Trial 1: SEF Describing the Shear Data	11
1.3.2	Trial 2: SEF Describing the Shear and Biaxial Data	13
1.4	Discussion	14
1.5	Conclusions	15
	References	16
2	Electromechanical <i>In Silico</i> Testing Alters Predicted Drug-Induced Risk to Develop Torsade de Pointes	19
	Anna Busatto, Jonathan Krauß, Evianne Kruithof, Hermenegild Arevalo, and Ilse van Herck	
2.1	Introduction	20
2.2	Methods	20
2.2.1	Drug Implementation	21
2.2.2	SimCardEMS Simulations	21
2.2.3	Evaluation	22
2.3	Results	24
2.3.1	Action Potential Duration	24

2.3.2	Electromechanical Window	25
2.3.3	Maximum Active Tension	26
2.3.4	<i>In Silico</i> and <i>in Vitro</i> TdP Risk Classifications	27
2.4	Conclusions	27
	References	29
3	<i>In silico</i> Investigation of Sex-Specific Osteoarthritis in Human Articular Chondrocytes	31
	Khoa Ngo, Nathaniel T Herrera, Milda Folkmanaite, Kei Yamamoto, and Mary M Maleckar	
3.1	Introduction	32
3.2	Methods	33
3.2.1	Modeling Ionic Changes Induced by Osteoarthritis in Male and Female Chondrocytes	35
3.2.2	Generation of a Population of Models	35
3.2.3	Model Parameter Sensitivity Analysis	36
3.3	Results	36
3.3.1	Modeling the Impact of Sex-Specific OA on Resting Membrane Potential	36
3.3.2	Population of Models	37
3.3.3	Parameter Sensitivity Analysis	37
3.3.4	Inhibiting I_{NaK} Restores Normal Resting Membrane Potential in OA Chondrocytes	38
3.4	Discussion	40
3.5	Conclusions	42
	References	43
4	Recapitulating Functional Heterogeneity in Electrophysiologically Active Tissues	45
	Meye Bloothoof, Joseph G Shuttleworth, Gabriel Neiman, Ishan Goswami, and Andrew G Edwards	
4.1	Introduction	46
4.2	Methods	47
4.2.1	Cardiomyocytes	48
4.2.2	Islet β -cells	51
4.3	Results	52
4.3.1	Cardiomyocyte PoM	52
4.3.2	Islet β -cell PoM	56
4.4	Discussion	59
	References	61

5	Realizing Synaptic Signal Transmission During Astrocyte-Neuron Interactions within the EMI Framework	65
	Julia Gorman, Konstantin Holzhausen, Joyce Reimer, and Jørgen Riseth	
5.1	Introduction	66
5.2	Methods	67
5.2.1	Representation of the Computational Domain	68
5.2.2	Mathematical Modeling of Glutamate Dynamics	69
5.2.3	Modeling AMPA Gating Dynamics	69
5.2.4	Estimation of Model Parameters	70
5.2.5	Numerical Methods	71
5.3	Results	72
5.4	Discussion	75
	References	77
6	Inducing Flow Instabilities in Aneurysm Geometries via the Reynolds-Orr Method	79
	Alessandro Contri, Christina Taylor, Justin Tso, and Ingeborg Gjerde	
6.1	Introduction	79
6.2	Methods	81
6.2.1	Reynolds-Orr Instability	81
6.2.2	Unsteady Navier-Stokes FEM Discretization	83
6.3	Results	84
6.4	Discussion	86
	References	89
7	Impact of Pathological Vascular Remodelling on Right Ventricular Mechanics	91
	Jiaxin (Katie) Cui*, Mariluz Rojo Domingo*, Ryan Konno*, Claudia A Manetti*, George Kagugube*, Oscar Odeigah, and Joakim Sundnes	
	* These authors contributed equally to this work	
7.1	Introduction	92
7.2	Methods	93
7.2.1	Base Model of PAH	93
7.2.2	Ventricular Interaction and the Pericardium	95
7.2.3	Right Ventricular Remodelling and Baroreflex	97
7.2.4	Atrial Septostomy	97
7.2.5	Right Ventricular Assistive Device (RVAD)	98
7.3	Results	98
7.3.1	Sensitivity Analysis	100
7.3.2	Ventricular Interaction and the Pericardium	100
7.3.3	Remodelling the Right Ventricle	102
7.3.4	Atrial Septostomy	103
7.3.5	Right Ventricular Assistive Device	104
7.4	Discussion	105

7.5 Conclusion..... 106
References 108



Chapter 1

An Automated Cardiac Constitutive Modelling Framework with Evolutionary Strain Energy Functions

Kristin Ludwicki*, Leto L Riebel*, Sophia Ohnemus*, Frida M E Westby, Nickolas Forsch, and Gabriel Balaban

* These authors contributed equally to this work

Abstract Heart disease is the leading cause of mortality worldwide. Many cardiac diseases are associated with altered elastic energy relations of the heart tissue. However, the strain energy functions describing these characteristics are limited since they were designed manually for highly specific experimental setups. In this study, we develop CHESRA (Cardiac Hyperelastic Evolutionary Symbolic Regression Algorithm), an automated constitutive modelling framework, to derive cardiac elastic strain energy functions directly from experimental data. Our results indicate that CHESRA finds functions that reproduce mechanical tissue properties from experimental data whilst controlling function complexity. Our novel approach has the potential to find strain-energy functions that fit to various experimental data sets and may contribute to automatically building mathematical models to understand clinical observations of heart diseases.

Kristin Ludwicki

Department of Physiology and Biophysics, Weill Cornell Medicine, New York, USA

Leto L Riebel

Department of Computer Science, University of Oxford, UK

Sophia Ohnemus

Institute for Experimental Cardiovascular Medicine, University Heart Center Freiburg - Bad Krozingen, Medical Center and Faculty of Medicine, University of Freiburg, DE

Frida M E Westby

Department of Informatics, University of Oslo, NO, Department of Computational Physiology, Simula Research Laboratory, NO

Nickolas Forsch

Department of Computational Physiology, Simula Research Laboratory, NO

Gabriel Balaban (corresponding author)

Department of Computational Physiology, Simula Research Laboratory, NO e-mail: gabrib@simula.no

1.1 Introduction

Cardiovascular disease is the leading cause of mortality worldwide, accounting for around 19 million deaths in 2020 [1]. In many cardiac diseases, the mechanical and structural properties of the heart are altered. Examples include hypertrophic cardiomyopathy, which is characterized by a thickening of the heart walls [2] and dilated cardiomyopathy, a disease which causes the ventricular walls to thin and stretch [3]. Another example is myocardial infarction, commonly known as a heart attack, during which oxygen and nutrient supply to the cardiac tissue is interrupted [4]. Myocardial infarction results in altered mechanical loading conditions [5], structural changes, increased tissue stiffness, and ultimately ventricular dysfunction [6]. A better understanding of these pathological mechanisms may improve clinical diagnosis and treatment options.

To characterize the elastic properties of the heart, stress-strain relations of the myocardium have been extensively studied experimentally. Assessment of passive shear properties of pig ventricular myocardium by Dokos et al. [7] indicates that the myocardium presents as an orthotropic material since the shear response differs along three mutually orthogonal directions. Demer and Yin [8] and Yin et al. [9] measured the stress-strain relationship of passive non-contracting canine myocardium for simultaneous biaxial stretching and observed highly nonlinear, anisotropic, and viscoelastic behavior. Novak et al. [10] performed more biaxial experiments in canine myocardium from different regions of the left ventricle and found that qualitatively the mechanical properties were similar, but quantitatively they differed. For example, samples from sub-endocardium and sub-epicardium of the left ventricular free wall tended to be more rigid than samples from the mid-myocardium.

In order to mathematically represent the mechanical properties of the heart tissue, a number of strain-energy functions (SEF) have been proposed. These SEF describe the potential energy density of the heart tissue depending on its deformation and have been developed based on a few key considerations. Considerations include structural metrics and other experimental results, as well as assumptions on physical properties of the system. Although the myocardium appears to be a viscoelastic material, the relaxation time of the viscoelastic response is long compared to the cardiac cycle [11]. Therefore, most SEF, with exceptions as presented in [12], model it as hyperelastic for simplicity reasons. Examples for SEF based on the assumption of transverse isotropy are given in [13, 14], whereas [11, 15, 16, 17] introduce orthotropic models. However, creating these SEF is labor intensive as they must be derived manually and, thus, only a limited amount of experimental data can be considered.

Evolutionary algorithms have the potential to automatically find functions that describe experimental data with minimal human guidance. This has been applied already to various research fields; for example, Doglioni et al. used evolutionary polynomial regression (EPR) to build a function for the relationship between air and water temperature [18]. Their method not only considered suitability of the discovered function to describe the given data, but also aimed to minimise the complexity of the formula. Montes et al. used a modified EPR framework to create

self-cleansing models for new sewer systems [19] and several different machine learning methods, including EPR, were used by Jamei et al. to model the density of hybrid nanofluids [20]. Furthermore, Javadi et al. established an EPR method to build constitutive equations describing the deformation of bridges and tunnels [21].

In this work we present the development of a Cardiac Hyperelastic Evolutionary Symbolic Regression Algorithm (CHESRA) that derives hyperelastic SEF for ventricular myocardium. In contrast to EPR algorithms, CHESRA is not restricted to polynomials, but searches the whole space of mathematical functions for SEF describing the given experimental data. Our results highlight the potential to automatically find SEF which reproduce experimental findings of cardiac elastic properties of different species.

1.2 Methods

In the following subsections we outline the individual components of CHESRA. First, in 1.2.1 we briefly introduce the physical principles of hyperelastic continuum mechanics that we use to define the SEF. Then, in 1.2.2 we outline how we represent the SEF computationally as function trees. Subsequently, we explain how we fit the SEF to experimental data in 1.2.3. Lastly, we go through the individual steps of the evolutionary symbolic regression (ESR) algorithm in detail in 1.2.4.

1.2.1 Basic Principles of Hyperelastic Continuum Mechanics

In order to define our SEF, we build upon the framework developed by Holzapfel and Ogden for cardiac hyperelasticity [11]. Here, the structure of the myocardium is characterized by three orthonormal basis vectors: the fibre axis f associated with the prevailing cell orientation, the sheet axis s defined as the direction in the plane of the cell sheets perpendicular to the fibre direction, and the sheet-normal axis n perpendicular to f and s .

Any point within the material can be described by a vector $\mathbf{X} = \sum_{i=f,s,n} c_i \mathbf{e}_i$, where \mathbf{e}_i denote the basis vectors of the f , s , and n axis. Upon deformation, the position of each point changes and the new position can be described by a vector \mathbf{x} . The fundamental quantity describing such a deformation is the deformation gradient \mathbf{F} , defined by $F_{ij} = \partial x_i / \partial X_j$ with $i, j = f, s, n$ and where $J = \det \mathbf{F} = 1$ for an incompressible material such as the myocardium. The right Cauchy-Green tensor

$$\mathbf{C} = \mathbf{F}^T \mathbf{F}, \quad (1.1)$$

and the Green-Lagrange strain tensor

$$\mathbf{E} = \frac{1}{2}(\mathbf{C} - \mathbf{I}), \quad (1.2)$$

are associated with \mathbf{F} , with \mathbf{I} being the identity tensor.

Since these quantities do not only account for deformation but also for rotation and translation, in the following, we consider the invariants of \mathbf{C} which are defined as

$$\begin{aligned} I_1 &= \text{tr}\mathbf{C}, & I_2 &= \frac{1}{2}[I_1^2 - \text{tr}\mathbf{C}] & I_3 &= \det \mathbf{C}, \\ I_{4i} &= \mathbf{e}_i^T (\mathbf{C}\mathbf{e}_i), & I_{5i} &= \mathbf{e}_i^T (\mathbf{C}^2\mathbf{e}_i), & I_{8ij} &= \mathbf{e}_i^T (\mathbf{C}\mathbf{e}_j), \end{aligned} \quad (1.3)$$

with $i \neq j \in \{f, s, n\}$. Defining a SEF based on these invariants ensures objectivity. The SEF proposed by Holzapfel and Ogden [11] is given by

$$\begin{aligned} \psi &= \frac{a}{2b} \exp[b(I_1 - 3)] + \sum_{i=f,s} \frac{a_i}{2b_i} \left\{ \exp[b_i(I_{4i} - 1)^2] - 1 \right\} \\ &+ \frac{a_{fs}}{2b_{fs}} \left\{ \exp[b_{fs}I_{8fs}^2] - 1 \right\}. \end{aligned} \quad (1.4)$$

Here, a , b , a_f , b_f , a_s , b_s , a_{fs} , and b_{fs} are material parameters chosen to either fit the corresponding Cauchy stress tensor

$$\boldsymbol{\sigma} = J^{-1} \mathbf{F} \sum_k \frac{\partial \psi}{\partial I_k} \frac{\partial I_k}{\partial \mathbf{F}} \quad (1.5)$$

to the shear data from Dokos et al. [7], or the associated second Piola-Kirchhoff stress tensor

$$\mathbf{S} = J\mathbf{F}^{-1} \boldsymbol{\sigma} \mathbf{F}^{-T} \quad (1.6)$$

to the biaxial stretch data by Yin et al. [9] (see Section 1.2.3.1 for details about these experimental data sets).

1.2.2 Representation of the Strain-Energy Functions as Function Trees

In CHESRA, SEF are represented as a list of nodes composing function trees. Details on function tree implementation and use cases can be drawn from [22, 23]. In our implementation, each node in the function tree has a type, a value, up to one parent, and up to two children (one left and one right). Only the root node of the function tree has no parent, further explained in 1.2.4.1. Nodes with no children are called 'leaves'. Sub-trees within the function tree represent individual terms of the SEF.

Nodes are either a symbol, an operand, or a pre-operand. Nodes of type symbol can either be a constant material parameter or an invariant. Material parameters are represented by the symbols $\{p_1, p_2, p_3, p_4, p_5, p_6, p_7, p_8\}$. These material parameters are later replaced by a constant real number to fit the SEF to experimental data, as described in 1.2.3. Similarly, invariant nodes are assigned a symbol from

the set of invariants $\{I_1, I_2, I_3, I_{4f}, I_{4s}, I_{4n}, I_{5f}, I_{5s}, I_{5n}, I_{8fs}, I_{8fn}, I_{8ns}\}$, as defined in Equation 1.3. Operand nodes can either have the value + (addition), - (subtraction), \div (division) or * (multiplication); and pre-operands are either *pow* (to the power of 2), *exp* (euler's number 'e' to the power of) or - (negation). While operands require two terms, for example $x + y$, a pre-operand requires only one, for instance e^x , which is written before the term in many coding languages, such as in python: *pow*($x, 2$). An example function tree is shown in Figure 1.1.

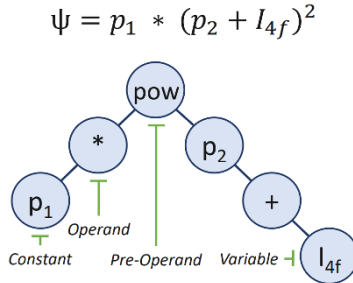


Fig. 1.1: Example SEF ψ and corresponding function tree with node types indicated. The function tree is converted to a real function ψ by applying an in-order traversal.

If a node of type symbol, *i.e.* either a material parameter or an invariant, has a parent node, it has to be either an operand or a pre-operand to be a valid function. Similarly, symbol nodes can only have children of type operand. Pre-operands are applied to terms, and hence can only have exactly one child, which has to be of type symbol or pre-operand. Their parent has to be either an operand or another pre-operand. Operands have a parent and exactly one child, both of which cannot be another operand. If an operand is a right child, its child needs to also be a right child and vice versa, to avoid two symbols next to each other. These rules are summarised in Table 1.1. We apply brackets only around the terms pre-operators are applied to, all other operations are carried out according to their priority, *e.g.* * before +.

Using the rules summarized in Table 1.1, to convert our function trees into functions we apply an in-order traversal, where any node is read out as: value of its left child, its own value, value of its right child. Figure 1.1 shows an example of a function and one of its possible corresponding function trees, depending on the order the terms are created in. Note that since our algorithm does not perform any searches within the tree, there is no need for it to be balanced.

Representing SEF as function trees has several benefits. Firstly, individual terms can be identified as sub-trees, allowing for pre-operands to be applied to parts of the equation only. This would be more difficult, for example, in a linked list structure. Secondly, terms can be manipulated, swapped, and deleted easily during mutation and mating, which are explained in 1.2.4.2.

Type	Value	Rules
Symbol	Invariant (variable), material parameter (const)	-Parent has to be an operand or pre-operand -Child has to be an operand
Operand	+, -, *, ÷	-Has exactly one parent of type symbol -Has exactly one child of type symbol/pre-operand
Pre-Operand	e^x , x^2 , $-x$	-Parent has to be an operand or pre-operand -Child has to be a symbol or pre-operand

Table 1.1: Summary of node types, possible node values, and node connection rules within the function tree.

1.2.3 Fitting the Strain-Energy Functions to Experimental Data

For each SEF ψ we fit the material parameters p_n to experimental data sets in a separate step, in order to ensure that only the material parameters differ for different experimental setups while the general form of the SEF is the same. In this work we consider the shear data of Dokos et al. [7] and the biaxial stretch data by Yin et al. [9], which we briefly describe in the following.

1.2.3.1 Experimental Data under Consideration

Dokos et al. [7] measured the shear stress, corresponding to the Cauchy stress tensor components σ_{ij} versus the amount of shear γ in a cube of pig left ventricular myocardium sheared in the fs , fn , or ns plane (see Figure 1.2a). They considered different shear modes (ij) referring to shear in the ij plane in j direction with $i \neq j \in \{f, s, n\}$.

The biaxial stretch data from Yin et al. [9] was collected in canine left ventricular tissue which was stretched simultaneously in the fibre and sheets direction. Figure 1.2b shows the measured second Piola-Kirchhoff stress S_{ff} versus strain E_{ff} and respectively S_{ss} versus E_{ss} for three different constant strain ratios $r = E_{ff}/E_{ss}$.

For both data sets, we used the digitizer software WebPlotDigitizer [24] to digitize the data from the graphs shown in [7] and [9].

1.2.3.2 Fitting to the Experimental Data

In order to fit the material parameters p_n of a SEF ψ to the shear data set we calculated the predicted Cauchy stress tensor components σ_{ij} according to Equation 1.5. Then, we used the Python package lmfit [25] to minimize the residuals,

$$res_k = s_{ij}(\gamma_k) - \sigma_{ij}(\gamma_k), \quad (1.7)$$

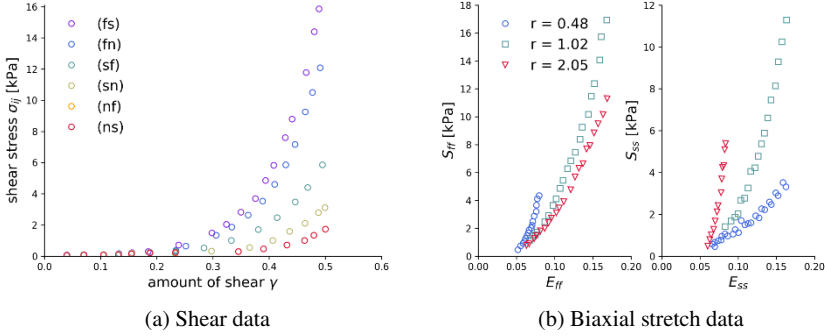


Fig. 1.2: Experimental data sets under consideration. (a) Plot of the digitized data collected by Dokos et al. [7] in pig left ventricular myocardium for shear stress σ_{ij} versus the amount of shear γ for shear (ij) in the ij plane in j direction with $i \neq j \in \{f, s, n\}$. Results for (nf) and (ns) shear are identical. (b) Visualization of the data by Yin et al. [9] for biaxial loading in the fs plane of canine left ventricular myocardium. The left plot shows the stress S_{ff} versus strain E_{ff} in the fibre direction and the right plot S_{ss} versus E_{ss} in the sheets direction for three different strain ratios $r = E_{ff}/E_{ss} = 2.05$ (triangles), 1.02 (squares) and 0.48 (circles). In both cases we used WebPlotDigitizer [24] to digitize the data shown in [7] and [9].

between experimental data points s_{ij} and the corresponding calculated stress tensor component σ_{ij} for all shear modes (ij) and all amounts of shear γ_k in the data set simultaneously.

Analogously, for fitting the material parameters to the biaxial data set we calculated the diagonal components of the second Piola-Kirchhoff stress tensor S_{ii} according to Equation 1.6. We used the same Python package for simultaneously minimizing the residuals

$$res_k = s_{ii}(E_{ii,k}) - S_{ii}(E_{ii,k}), \quad (1.8)$$

with $i = f, s$, for all Green-Lagrange strain tensor components $E_{ii,k}$ and strain ratios $r = E_{ff}/E_{ss}$ in the data set.

1.2.4 Evolutionary Symbolic Regression Algorithm

To develop CHESRA, we build upon the traditional ESR framework. First, populations of random SEF are created (see Section 1.2.4.1). Then, every equation within each iteration, or generation, is assigned an error-score based on a user-designed fitness function. Our fitness function assesses the complexity of the SEF and how well it fits to the shear and/or biaxial data set (see Section 1.2.4.3). The individuals

with the best fitness are then selected, mated to generate a new population, and mutated to ensure diversity for the next generation (see Section 1.2.4.2). This multi-step process continues until the maximum number of generations is reached. A schematic representation of CHESRA is illustrated in Figure 1.3.

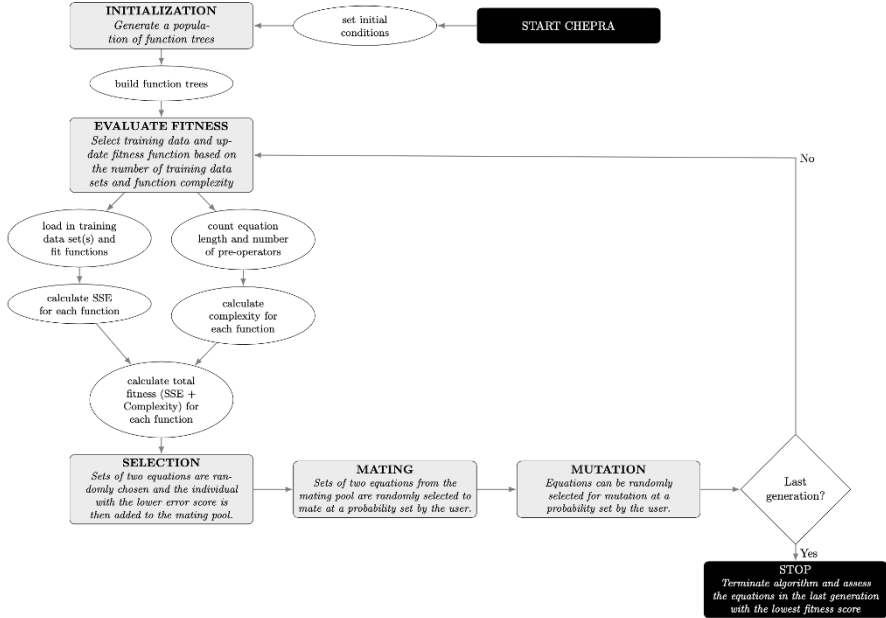


Fig. 1.3: The main workflow of CHESRA.

1.2.4.1 Setup and Initialisation

To initialise SEF and their corresponding function trees, a maximum function length, set of invariants, and material parameters are defined. First, our algorithm creates a root node, which is always an invariant or a material parameter. Second, it picks a random length within the given maximum and extends the function tree until this chosen length is reached. The function can either be extended by adding a pre-operand in front of a term, or by attaching an operand and a new symbol (i.e., an invariant or material parameter) to an existing symbol. For the latter, the selected existing symbol may have at most one child. Details concerning function development can be found in Section 1.2.2.

1.2.4.2 Mutation and Mating of Strain-Energy Functions

We mutate SEF by randomly selecting a node from the corresponding function tree to be mutated. The selected node is then replaced by a randomly chosen element of the same type (see 1.4).

To mate two parent SEF and create two new children, our algorithm creates a deep copy of each parent function tree, chooses one random sub-tree per copy, and then swaps them over. To make sure the resulting children SEF are valid functions, we restrict the chosen sub-trees to be proper terms and hence start with a symbol or pre-operand. Alternatively, one may also choose to ensure the sub-trees to be swapped to start with a node of the same type. Our chosen sub-trees may be of different size and hence children SEF may be of different lengths than their parents (see 1.5).

Mutation and mating are important to increase population diversity in CHESRA. However, too much diversity could also prohibit convergence towards an optimal solution. Therefore, we set rates that will dictate the probability of a given individual to mate, p_{mate} , and/or mutate, p_{mutate} . These rates were set to $p_{\text{mate}} = 20\%$ and $p_{\text{mutate}} = 80\%$ in all CHESRA experiments.

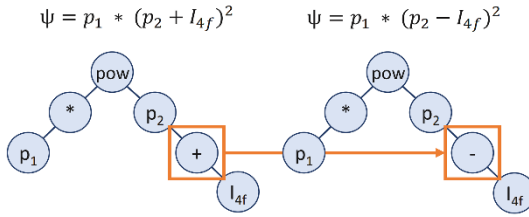


Fig. 1.4: An exemplary function tree representing a SEF ψ is mutated by choosing a random item and replacing it with a random value of the same type, as highlighted by the orange boxes.

1.2.4.3 Scoring Fitness of Strain-Energy Functions

We designed a fitness function to ensure that CHESRA can penalize against poor fitting SEF with high complexity. Therefore, each SEF, or individual, in each generation is evaluated based on its complexity and how well it reproduces the results of a specific experimental data set. It is this evaluation that allows the best individuals to be selected for mating, mutation, and population of the following generation.

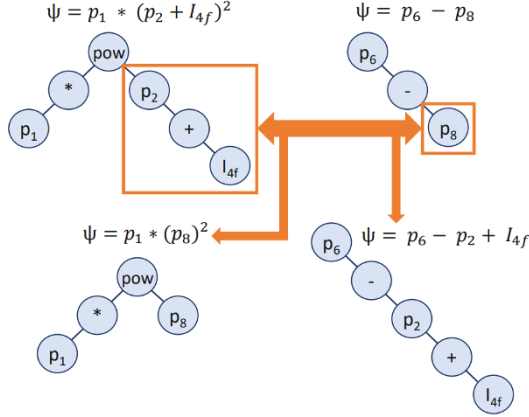


Fig. 1.5: Mating between two parent SEF to generate two children SEF is implemented by swapping two random subtrees from the corresponding function trees as highlighted in the orange boxes.

To evaluate the fitness of each equation, first we quantify its complexity as the sum of the function length l_{eq} (i.e., the number of nodes it consists of), and the number of pre-operators $n_{\text{pre-op}}$ that it contains. The pre-operator count allows for penalization against nestedness, or the creation of functions with pre-operators within themselves.

$$\text{Complexity} = l_{\text{eq}} + n_{\text{pre-op}}. \quad (1.9)$$

Second, we assess how well each individual SEF reproduces experimental data. For this, the material parameters of each equation are first fitted to the experimental data as described in 1.2.3.2. Then, for each equation the sum of squared errors (SSE) is calculated as the sum of the squared residuals res_k between the experimental data points and the fit,

$$SSE = \sum_k res_k^2, \quad (1.10)$$

with res_k as defined in Equation 1.7 for the shear data or in Equation 1.8 for the biaxial stretch data.

The final fitness score is then given by

$$\text{Fitness} = (\alpha * \text{Complexity}) + SSE, \quad (1.11)$$

where the hyperparameter α ensures appropriate balance between fitting and complexity. Numerical experiments conducted to find a suitable α can be found in Section 1.3.1.

Where CHESRA is given N data sets, the fitness function can be extended to

$$\text{Fitness} = (\alpha * \text{Complexity}) + \sum_N SSE_N. \quad (1.12)$$

Hence, in the following section 1.3.1 we used Equation 1.11 in order to find a SEF that can reproduce the shear data alone, while in section 1.3.2 we used Equation 1.12 to consider both the shear and the biaxial data set.

1.3 Results

1.3.1 Trial 1: SEF Describing the Shear Data

In our first trial, we ran CHESRA while fitting the SEF to the shear data set from Dokos et al. [7]. We chose the hyperparameter α of the fitness function (see Equation 1.10) by running CHESRA with $\alpha = 10^{-5}, 10^{-3}, 10^{-1}, 1, 2,$ and 5 for 50 generations and 100 individuals each. 1.6 indicates that a value of $\alpha = 0.1$ lead to the best result as it allowed for SEF with low SSE and minimal complexity. Using this hyperparameter, the fitness score of the best SEF gradually decreased over the generations until a plateau was reached (see 1.7).

In this run, the SEF with the lowest fitness score derived using CHESRA reproduces the shear data well (see 1.8a) and is given by

$$\psi_1 = \exp(p_1 I_{5s} + p_2 I_{5f} + 2I_2 - I_{4n} - p_3). \quad (1.13)$$

In order to assess whether CHESRA is reproducible, we repeated this trial twice, with the best SEF given by

$$\psi_2 = -(I_{5f} - p_1)^2 + p_2 I_{5f} ((I_5 + p_3)^2 + I_{4s})^2, \quad (1.14)$$

$$\psi_3 = \exp(p_1^2 I_{5f} + (p_2 + p_3 - 1) I_{8fs} + p_4 I_{4f} + I_1 + 2I_2 - I_{4n} + p_5). \quad (1.15)$$

The equations derived from the three trial runs have unique material parameters that can be found in 1.2. 1.8 shows a good fit to the shear data for all three SEF found.

Trial run	p_1	p_2	p_3	p_4	p_5
1	0.77	2.00	9.92	-	-
2	1.47	0.20	0.50	-	-
3	0.86	1.44	0.04	1.38	510.06

Table 1.2: Material parameters to fit the SEF defined in Equation 1.13 (trial run 1), 1.14 (trial run 2), 1.15 (trial run 3) to the shear data set by Dokos et al. [7]

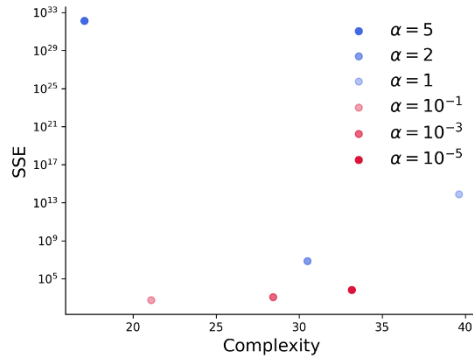


Fig. 1.6: SSE vs. complexity for different hyperparameters α in the fitness function (see Equation 1.11). Six runs of CHESRA were completed in which each was run with one of the unique α values listed in the legend. For experiment 1, we chose $\alpha = 0.1$ since it lead to SEF with low SSE and function complexity.

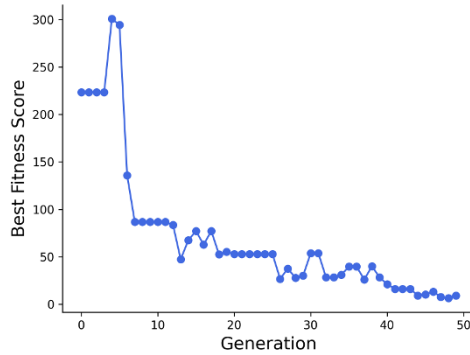


Fig. 1.7: Evolution of 100 individual SEF for 50 generations. Each point represents the fitness of the best SEF from each generation.

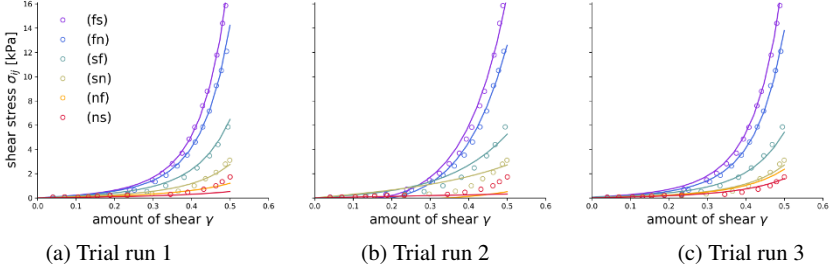


Fig. 1.8: In our numerical experiment 1, CHESRA found a SEF that reproduces the shear data of Dokos et al. [7] in all 3 trial runs. Markers represent the experimental data points whereas solid lines show the fit of the SEF derived using CHESRA.

1.3.2 Trial 2: SEF Describing the Shear and Biaxial Data

As a next step, we extended CHESRA to find a SEF that reproduces the results of multiple experimental data sets. Therefore, we ran CHESRA with the same setup as in trial 1, but updated the fitness function to incorporate the SSE of both the shear and the biaxial data set, as described in Equation 1.12. Moreover, in this numerical experiment we used $\alpha = 0$ in order to assess quality of fit without penalizing for equation complexity. In addition, $\alpha = 0$ allowed convergence in a shorter number of generations as fitting to two different data sets is a challenging optimization problem.

The SEF found using CHESRA is given by

$$\psi = \left(p_1 p_2 I_{4f} - I_{4f}^2 + \frac{p_1}{I_{5n}} - I_{4s} [p_1 p_2 I_{5n} I_{4f} - p_3 p_4^2 I_1 + p_5 + p_6 + p_7]^2 - p_4 p_6 - p_1 - p_6 + p_7 \right)^2, \quad (1.16)$$

where the material parameter values are provided in Table 1.3. Figure 1.9 shows that the equation derived in experiment 2 has a better fit to the biaxial data than to the shear data.

Data	p_1	p_2	p_3	p_4	p_5	p_6	p_7
Shear	0.00	433.64	33.52	0.31	1.85	3.08	4.95
Biaxial	0.49	1.34	1.24	1.11	2.56	0.04	2.06

Table 1.3: Material parameters for fitting the SEF defined in Equation 1.16 to the shear and biaxial data sets.

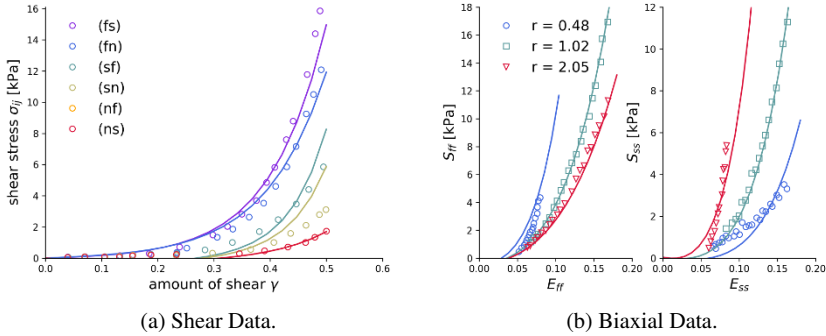


Fig. 1.9: In experiment 2, CHESRA was extended to find a single SEF aimed to reproduce both the shear data from Dokos et al. (a) and biaxial stretch data from Yin et al. (b). Solid lines show the fit of the SEF found using CHESRA to the experimental data represented by the markers.

1.4 Discussion

CHESRA automatically generates functions which reproduce experimental data of cardiac hyperelastic properties. The results of trial 1 indicate that CHESRA can derive SEF that fit the shear data from Dokos et al. [7] well. However, the quality of fit was not equal for all shear directions. Specifically, in all trial runs the derived SEF did not fit to the shear data for the (nf) and (ns) direction, as shown in Figure 1.8. As the magnitude of shear stress is much lower in those cases, it is likely that the fitness function neglects these shear modes. Previous studies have used coefficient of determination in the fitness function [18, 21], which will be a key consideration in our future work.

To extend CHESRA to multiple experimental data sets, we included both shear [7] and biaxial data [9] in trial 2. Here, the biaxial data was fitted at the expense of the shear data. A possible cause for this could be a non-optimal individual and generation number. Since more data sets were given to the algorithm, optimization is challenging in only 50 generations. Therefore, increasing the number of generations and individuals may allow for better convergence and a more universal SEF to be found.

Ensuring that CHESRA derives simple equations was important to this study. Therefore, we included the hyperparameter α to the fitness function to ensure penalization against long equations with nesting. While this is a valuable proof-of-concept, it has limitations. Specifically, it does not take computational time into consideration. Long but simple equations might be penalized more compared to shorter, but more complex or nested functions. The time it takes for an equation to be calculated may be a better measure of simplicity and will be explored in next steps.

Moreover, the current version of CHESRA can only generate SEF using quadratic and exponential functions; however, this could be widened to a larger function space. In addition, CHESRA may be extended to even more experimental data sets. Future work may also investigate to what extent the functions generated by CHESRA fulfill the mathematical requirements of SEF, such as convexity and strong ellipticity [11]. Lastly, it would be interesting to compare our method to a Multivariate Adaptive Regression Spline (MARS) model since studies by Jamei et al. [20] suggest that this can be more accurate than ESR.

1.5 Conclusions

In this work we present CHESRA, an ESR framework for automatically deriving strain-energy functions of the myocardium. Our algorithm allows for controlling function complexity and inputting multiple experimental data sources.

References

1. CW Tsao, AW Aday, ZI Almarzooq, A Alonso, AZ Beaton, MS Bittencourt, et al. Heart disease and stroke statistics – 2022 update: A report from the american heart association. *Circ.*, 145:e152–e639, 2022.
2. Barry J Maron, Paolo Spirito, Yvonne Wesley, and Javier Arce. Development and progression of left ventricular hypertrophy in children with hypertrophic cardiomyopathy. *New England Journal of Medicine*, 315(10):610–614, 1986.
3. Naila Choudhary, Gangadhara Kabbli, Lynette J Duncanson, Michael Passick, Kathy Halloran, and Jie J Cao. Comparison of myocardial mechanical properties in patients with dilated cardiomyopathy with and without acute heart failure. *Journal of Cardiovascular Magnetic Resonance*, 16(1):1–2, 2014.
4. Lei Lu, Min Liu, RongRong Sun, Yi Zheng, and Peiying Zhang. Myocardial infarction: symptoms and treatments. *Cell biochemistry and biophysics*, 72(3):865–867, 2015.
5. Martin G St John Sutton and Norman Sharpe. Left ventricular remodeling after myocardial infarction: pathophysiology and therapy. *Circulation*, 101(25):2981–2988, 2000.
6. Michael A Garza, Emily A Wason, and John Q Zhang. Cardiac remodeling and physical training post myocardial infarction. *World journal of cardiology*, 7(2):52, 2015.
7. Socrates Dokos, Bruce H Smaill, Alistair A Young, and Ian J LeGrice. Shear properties of passive ventricular myocardium. *American Journal of Physiology-Heart and Circulatory Physiology*, 283(6):H2650–H2659, 2002.
8. Linda L Demer and FC Yin. Passive biaxial mechanical properties of isolated canine myocardium. *The Journal of physiology*, 339(1):615–630, 1983.
9. Frank CP Yin, Robert K Strumpf, Paul H Chew, and Scott L Zeger. Quantification of the mechanical properties of noncontracting canine myocardium under simultaneous biaxial loading. *Journal of biomechanics*, 20(6):577–589, 1987.
10. Vincent Paul Novak, FCP Yin, and JD Humphrey. Regional mechanical properties of passive myocardium. *Journal of biomechanics*, 27(4):403–412, 1994.
11. Gerhard A Holzapfel and Ray W Ogden. Constitutive modelling of passive myocardium: a structurally based framework for material characterization. *Philosophical Transactions of the Royal Society A: Mathematical, Physical and Engineering Sciences*, 367(1902):3445–3475, 2009.
12. Jacques M Huyghe, Dick H van Campen, Theo Arts, and Robert M Heethaar. The constitutive behaviour of passive heart muscle tissue: a quasi-linear viscoelastic formulation. *Journal of biomechanics*, 24(9):841–849, 1991.
13. JD Humphrey and FCP Yin. On constitutive relations and finite deformations of passive cardiac tissue: I. a pseudostrain-energy function. *Journal of biomechanical engineering*, 109:298–304, 1987.
14. JD Humphrey, RK Strumpf, and FCP Yin. Determination of a constitutive relation for passive myocardium: I. a new functional form. *Journal of biomechanical engineering*, 112:333–339, 1990.
15. Kevin D Costa, Jeffrey W Holmes, and Andrew D McCulloch. Modelling cardiac mechanical properties in three dimensions. *Philosophical transactions of the Royal Society of London. Series A: Mathematical, physical and engineering sciences*, 359(1783):1233–1250, 2001.
16. H Schmid, MP Nash, AA Young, and PJ Hunter. Myocardial material parameter estimation—a comparative study for simple shear. *Journal of biomechanical engineering*, 128:742–750, 2006.
17. Martyn P Nash and Peter J Hunter. Computational mechanics of the heart. *Journal of elasticity and the physical science of solids*, 61(1):113–141, 2000.
18. A Doglioni, O Giustolisi, DA Savic, and BW Webb. An investigation on stream temperature analysis based on evolutionary computing. *Hydrological Processes: An International Journal*, 22(3):315–326, 2008.
19. Carlos Montes, Luigi Berardi, Zoran Kapelan, and Juan Saldarriaga. Predicting bedload sediment transport of non-cohesive material in sewer pipes using evolutionary polynomial

- regression–multi-objective genetic algorithm strategy. *Urban Water Journal*, 17(2):154–162, 2020.
20. Mehdi Jamei, Masoud Karbasi, Mehdi Mosharaf-Dehkordi, Ismail Adewale Olumegbon, Laith Abualigah, Zafar Said, and Amin Asadi. Estimating the density of hybrid nanofluids for thermal energy application: Application of non-parametric and evolutionary polynomial regression data-intelligent techniques. *Measurement*, 189:110524, 2022.
 21. Akbar A Javadi and Mohammad Rezaia. Intelligent finite element method: An evolutionary approach to constitutive modeling. *Advanced Engineering Informatics*, 23(4):442–451, 2009.
 22. B Baka. Python data structures and algorithms: Improve the performance and speed of your applications. 2017.
 23. TH Cormen. Introduction to algorithms (3rd ed.). 2009.
 24. A Rohatgi. Webplotdigitizer version 4.5. <https://automeris.io/WebPlotDigitizer>, 2021. Accessed August 2022.
 25. M Newville, T Stensitzki, D Allen, and ALMFIT Ingargiola. Lmfit: Non-linear least-squares minimization and curve-fitting for python. *Chicago, IL*, 2015.

Open Access This chapter is licensed under the terms of the Creative Commons Attribution 4.0 International License (<http://creativecommons.org/licenses/by/4.0/>), which permits use, sharing, adaptation, distribution and reproduction in any medium or format, as long as you give appropriate credit to the original author(s) and the source, provide a link to the Creative Commons license and indicate if changes were made.

The images or other third party material in this chapter are included in the chapter's Creative Commons license, unless indicated otherwise in a credit line to the material. If material is not included in the chapter's Creative Commons license and your intended use is not permitted by statutory regulation or exceeds the permitted use, you will need to obtain permission directly from the copyright holder.





Chapter 2

Electromechanical *In Silico* Testing Alters Predicted Drug-Induced Risk to Develop Torsade de Pointes

Anna Busatto, Jonathan Krauß, Evianne Kruithof, Hermenegild Arevalo, and Ilse van Herck

Abstract Torsade de Pointes (TdP) is a type of ventricular tachycardia that can occur as a side effect of several medications. The Comprehensive *in vitro* Proarrhythmia Assay (CiPA) is a novel testing paradigm that utilizes single cell electrophysiological simulations to predict TdP risk for drugs that could potentially be used clinically. However, the effects on mechanical performance and mechano-electrical feedback are neglected. Here, we demonstrate that including electromechanical simulations in CiPA testing can provide additional insights into the predicted drug-induced TdP risk. In this work, we analyzed six drugs, namely flecainide, ibutilide, metronidazole, mexiletine, quinidine and ranolazine. We compared previously classified risks (low, intermediate, high) with our fully coupled electromechanical simulation results based upon the action potential, the electromechanical window, and the maximum active tension [1]. For ranolazine and metronidazole the predicted risk changed from low to intermediate and intermediate to high, respectively. For the latter, while electrophysiological markers indicated a low risk, the active tension decreased by 58% which can result in a loss of heart function. Therefore, adding mechanics to CiPA testing results in an altered prediction of drug-related TdP risk.

Anna Busatto

Department of Biomedical Engineering, University of Utah, USA, Scientific Computing and Imaging Institute, University of Utah, USA

Jonathan Krauß

Institute of Biomedical Engineering, Karlsruhe Institute of Technology, DE

Evianne Kruithof

Eindhoven University of Technology, NL

Hermenegild Arevalo

Department of Computational Physiology, Simula Research Laboratory, NO

Ilse van Herck (corresponding author)

Department of Computational Physiology, Simula Research Laboratory, NO e-mail: ilse@simula.no

2.1 Introduction

Torsade de Pointes (TdP) is a form of abnormal heart rhythm often preceded or caused by a prolonged QT-interval of the ECG [2]. Due to the high risk of unwanted and dangerous side-effects, promising new drugs with a potential TdP risk have been excluded from the research and drug-development pipeline. This, in combination with the long and complicated process of drug approval, led to a lack of new drugs on the market for cardiac disease. Therefore, the Comprehensive *in vitro* Proarrhythmia Assay (CiPA) is performed to better predict the TdP risk for drugs that could potentially be used in the clinic. However, some of the tests can result in inaccurate predictions of the actual outcomes and lead to restrictive results, limiting the number of drugs allowed on the market.

There has been ongoing research on improving these models to increase the predictability of drug-induced effects in the heart [3]. Llopis *et al.* proposed CiPA testing using a population of models approach to obtain more accurate risk predictions by simulating the effects of altered ion channel functions on the electrophysiological behavior of cardiac cells [1].

The electromechanical window (EM_w) is a biomarker for TdP risk introduced by Passini *et al.* for *in silico* drug testing [4]. Clinically, EM_w is defined as the difference between the duration of electrical and mechanical systole [4]. However, for the *in silico* test, they defined the EM_w as the time difference between calcium transient duration at 90% repolarization ($CaTD_{90}$) and action potential duration at 90% repolarization (APD_{90}) [4]. This assumption makes the simulation computationally less expensive and complex, but this simplification reduces accuracy in the mechanical component.

In previous work, the effects of electromechanical feedback are neglected and no insight into the mechanical function is obtained. This feedback alters the electrophysiological results, especially the calcium transient, and affects the biomarkers used to predict TdP risk. However, the effect of drugs on the mechanical performance can be investigated with electromechanical simulations. Therefore, in this work, a fully coupled electromechanical simulator SimCardEMS is used to perform CiPA tests [5]. Here, the cardiac mechanical function can be analyzed in terms of active tension, tissue deformations and EM_w , where the latter can be altered due to electromechanical feedback. We performed several tests to compare our predicted TdP risks to previous classifications such as the ones found in Llopis *et al.* [1].

2.2 Methods

To assess TdP risk, we focused on selected biomarkers, namely maximum active tension $T_{a,max}$ [kPa], APD_{90} [ms], $CaTD_{90}$ [ms], and the EM_w [ms]. Using these metrics, we analyzed six different drugs from CiPA: flecainide, ibutilide, metronidazole, mexiletine, quinidine, and ranolazine with known cardiac effects. Each of the drugs has been classified as high, intermediate, or low risk for TdP in Llopis *et*

al. [1]. Here, the indicated risks are compared with the risks predicted by a fully coupled electromechanical model to investigate whether the mechanical biomarkers should also be taken into account for risk classification.

2.2.1 Drug Implementation

The cardiac effects of the drugs are tested for three different plasma concentrations (PC). For each of the concentrations, the ion channel conductances (g) are multiplied with scaling factors (SF) representing the effect of the tested drug. The SF values are calculated using the drug PC , the inhibitory concentration (IC_{50}) and Hill coefficient (h) value of the targeted ion channel:

$$SF = \frac{g_{\text{drug}}}{g} = [1 + (\frac{PC}{IC_{50}})^h]^{-1} \quad (2.1)$$

Table 2.1: Ion channel scaling factors (SF) for quinidine using three different plasma concentrations (PC). Scaling factors for seven ion channels were calculated with Equation 2.1.

Scaling factor	$PC_{0.5}$	$PC_{1.0}$	$PC_{2.0}$
SF_{K_r}	0.375	0.231	0.130
SF_{Na}	0.936	0.863	0.730
SF_{NaL}	0.585	0.429	0.285
SF_{CaL}	0.970	0.941	0.889
SF_{K_s}	0.985	0.967	0.929
SF_{K1}	0.983	0.977	0.970
SF_{to}	0.731	0.524	0.309

Equation 2.1 is derived from the standard Hill equation [1]. The PC , IC_{50} and h values are taken from Llopis *et al.*. The SF values are calculated for the considered ion channels I_{K_r} , I_{Na} , I_{NaL} , I_{CaL} , I_{K_s} , I_{K1} and I_{to} at three different PC s which are half ($PC_{0.5}$), normal ($PC_{1.0}$) and double ($PC_{2.0}$) the effective free therapeutic plasma concentration [1]. As an example, specific SF values used to simulate the effect of quinidine are shown in Table 2.1.

2.2.2 SimCardEMS Simulations

The calculated SF values are finally used as input for the SimCardEMS solver, which is implemented in FEniCS [6], to simulate the effects of drugs on an endocardial tis-

sue block. We solved the electrophysiological O’Hara-Rudy model which is strongly coupled with the mechanical Land model via intracellular calcium concentration and stretch activated channels [7, 8]. The active tension was scaled by a factor of five. The Holzapfel model was used to describe the tissue material properties, where we increased the stiffness by a factor of ten [9].

The simulations were performed on a 6x3x3 mm mesh representing an endocardial tissue slab with 1 mm and 0.5 mm spatial resolution for the mechanical and electrophysiological parts, respectively (Fig. 2.1). One corner of the mesh was fixed, and each of the connected planes were fixed in their respective normal directions, allowing the simulation of free contraction. The fibers were aligned in the longitudinal direction of the mesh and the tissue was activated by stimulating the entire mesh.

To reach steady state, 40 beats of 1000 ms each were simulated and used as control. Thereafter, the drugs were added into the simulation by loading the calculated SFs . Each of these simulations was run either for five or ten beats (1000 ms each) depending on when steady state was reached; the goal was to investigate the effect of each tested drug on the electrophysiological and mechanical behavior of the cells. The biomarkers used for the analysis were extracted from the center of the mesh for the last beat of each simulation.

2.2.3 Evaluation

The TdP risk classifications were based upon maximum active tension $T_{a,max}$, APD_{90} , $CaTD_{90}$, and EM_w where

$$EM_w = CaTD_{90} - APD_{90} \quad (2.2)$$

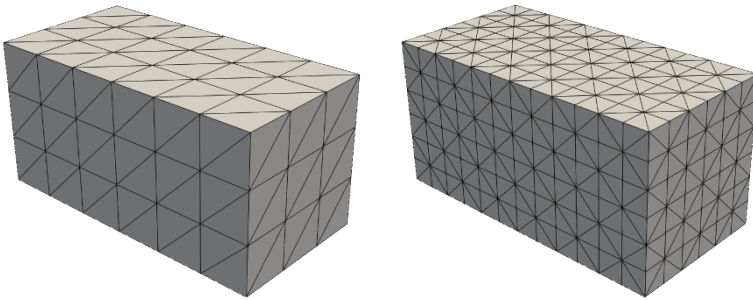


Fig. 2.1: (Left) Mechanical mesh 6x3x3 mm with 1 mm resolution. (Right) Electrophysiological mesh 6x3x3 mm with 0.5 mm resolution. Three planes are fixed in their normal direction to allow free contraction of the material.

The metrics used for evaluation are visualized in Fig. 2.2. TdP risk was classified as high or intermediate respectively in the following situations:

- $T_{a,max}$ decreases by more than 50% (high) or between 20% and 50% (intermediate) compared to control. Clinically, a decrease in ejection fraction from 60% to 35% is considered dangerous [10]. We assumed that a 50% drop in $T_{a,max}$ represented a similar level of danger for the patient since $T_{a,max}$ affects the contraction;
- APD_{90} increases by more than 10% (high) or between 6% and 10% (intermediate) compared to control [11, 12];
- EM_w decreases by more than 20% (high) or between 10% and 20% (intermediate) compared to control [4].

If none of these criteria were met, the drug was considered safe and classified as low risk.

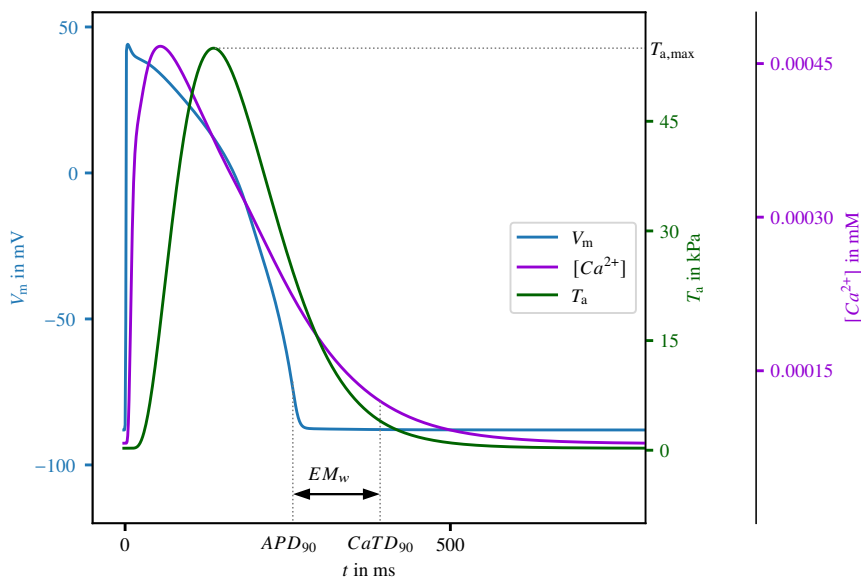


Fig. 2.2: Transmembrane voltage, calcium concentration, and active tension for control. The metrics used to evaluate the results are indicated in the figure with dashed lines.

2.3 Results

The biomarkers extracted for all simulations are shown in Table 2.2. For the control simulation we found a $T_{a,max}$ of 55.0 kPa, APD_{90} of 258 ms and EM_w of 134 ms. The associated risk classification thresholds for $T_{a,max}$ were 44.0 kPa (intermediate) and 27.5 kPa (high). For APD_{90} , the thresholds were 273 ms (intermediate) and 284 ms (high), while for EM_w they were 121 ms (intermediate) and 107 ms (high).

2.3.1 Action Potential Duration

The resulting action potentials for control as well as the six examined drugs at $PC_{1.0}$ are shown in Fig. 2.3. Ibutilide, quinidine and flecainide have APD_{90} values of 597 ms, 446 ms and 352 ms respectively which are above the threshold for high risk drugs. Ranolazine has an APD_{90} of 283 ms at $PC_{1.0}$ which fits in the range of intermediate risk drugs. APD_{90} values for metronidazole and mexiletine are below

Table 2.2: Overview of the extracted biomarkers, $T_{a,max}$ [kPa], APD_{90} [ms], $CaTD_{90}$ [ms], EM_w [ms] and TdP risk classifications for all performed simulations. $PC_{0.5}$, $PC_{1.0}$ and $PC_{2.0}$ results are given in this order for each of the six tested drugs.

Drug	$T_{a,max}$	APD_{90}	$CaTD_{90}$	EM_w	<i>in vitro</i> risk	<i>in silico</i> risk
Control	55.0	258	392	134	-	-
Flecainide	61.0	316	404	88	High	High
	66.4	352	412	60		
	75.4	400	425	25		
Ibutilide	50.8	531	541	9	High	High
	46.1	597	560	3		
	43.8	644	641	-3		
Metronidazole	28.8	249	393	145	Intermed	High
	22.9	252	396	144		
	17.8	263	401	138		
Mexiletine	54.8	253	390	136	Low	Low
	54.3	251	388	137		
	53.2	250	386	136		
Quinidine	56.1	372	425	53	High	High
	57.3	421	446	25		
	61.9	470	469	-2		
Ranolazine	68.7	272	391	119	Low	Intermed
	79.5	283	391	107		
	96.1	303	392	89		

the intermediate threshold and should therefore be classified as low risk if only the APD_{90} is considered.

All the chosen drugs were then examined for $PC_{0.5}$ and $PC_{2.0}$ as well. An example of the differences of action potential shape for quinidine based on the PC is shown in Fig. 2.4. A concentration dependent effect is observed for APD_{90} as it is the smallest for $PC_{0.5}$ and increases with an increase in PC. An overview of the APD_{90} values for each of the examined drugs at $PC_{0.5}$, $PC_{1.0}$, and $PC_{2.0}$ is given in Table 2.2.

2.3.2 Electromechanical Window

Looking at the EM_w values, high risk drugs were classified by 20% decrease compared to control; flecainide, ibutilide, and quinidine returned values below this threshold, indicating high risk, while metronidazole and mexiletine returned values above it. Finally, for ranolazine the decrease was slightly less than 20% which, in combination with the remaining biomarkers, led us to classify it as an intermediate risk drug. For all the drugs, the TdP risk classification based on the EM_w was the same as APD_{90} risk classifications. In four out of the six analyzed drugs, the EM_w pro-

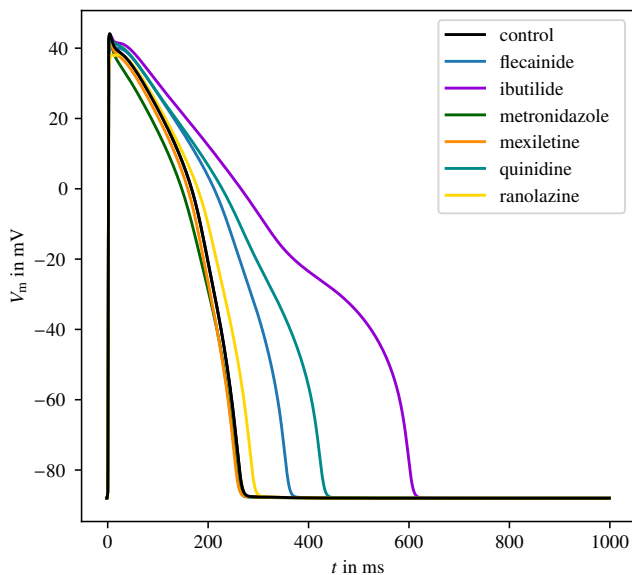


Fig. 2.3: Action potentials for control and six tested drugs at $PC_{1.0}$. Based on these results, ibutilide, quinidine and flecainide are classified as high risk. Ranolazine is classified as intermediate risk for this drug concentration.

gressively decreased with higher drug concentration compared to control. However, addition of metronidazole at $PC_{0.5}$ increased the EM_w initially while for higher concentrations of metronidazole ($PC_{2.0}$) the EM_w decreased again. The addition of mexiletine changed the EM_w by only 3 ms while both the APD_{90} and $CaTD_{90}$ remained similar to control. All results are shown in Table 2.2.

2.3.3 Maximum Active Tension

Applying metronidazole, the maximum active tension decreased from 55.0 kPa to 28.8 kPa, 22.9 kPa, and 17.8 kPa for $PC_{0.5}$, $PC_{1.0}$ and $PC_{2.0}$, respectively. This represents a decrease in $T_{a,max}$ of 48%, 58%, and 68%. For ranolazine, the $T_{a,max}$ increased by 45% at $PC_{1.0}$ compared to control. In the remaining drugs, the maximum active tension remained similar or slightly increased compared to control.

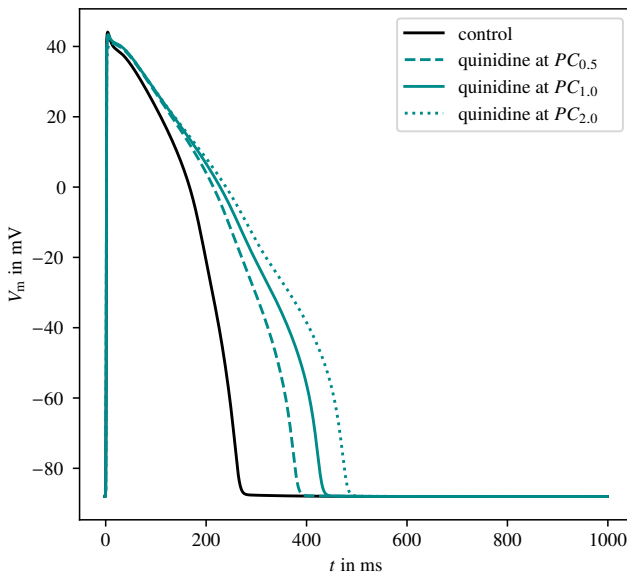


Fig. 2.4: Action potential for control and quinidine at $PC_{0.5}$, $PC_{1.0}$, and $PC_{2.0}$. An increase in PC highlights the drug concentration effect on the action potential duration.

2.3.4 *In Silico* and *in Vitro* TdP Risk Classifications

We classified all six drugs using the evaluation process described in section 2.2.3. Flecainide, ibutilide, and quinidine were determined to be high risk both in the previous classification and in our electromechanical model (based on APD_{90} and EM_w values). Based on the maximum active tension, the risk of metronidazole was changed from intermediate (CiPA indication) to high risk. On the other hand, following the APD_{90} and EM_w values it would have been classified as low risk. Mexiletine was classified as low in the CiPA as well as in our study. Lastly, ranolazine was previously predicted as low risk but was classified as intermediate risk using our model based on both the APD_{90} and EM_w values. Even though the increase in $T_{a,max}$ for ranolazine was the largest of the analyzed drugs, potentially having an effect on contraction and tissue stress, increases in $T_{a,max}$ were not considered in TdP risk classification.

2.4 Conclusions

In this study we analyzed six drugs, flecainide, ibutilide, metronidazole, mexiletine, quinidine, and ranolazine. Three of these drugs were classified as high risk, one as intermediate risk, and two as low risk according to CiPA. Using our fully coupled electromechanics model, four drugs were classified as high risk, one as intermediate risk and one as low risk. An overview of this distribution is given in Table 2.3. After performing our analysis, we concluded that some drugs may belong to different risk categories depending on the individual parameters considered. For example, ranolazine was previously classified as low risk; in our simulation, both the APD_{90} and EM_w biomarker values for $PC_{1,0}$ fell in the range of intermediate risk, while for $PC_{2,0}$ it was predicted high risk. In general, for all six drugs, both the APD_{90} and the EM_w biomarkers indicated the same risk categories. However, the risk classification based on $T_{a,max}$ differed from the other biomarkers. For metronidazole, a low TdP risk was observed based on the electrophysiological biomarkers. Despite that, there was a decrease of 58% in $T_{a,max}$ which can lead to severe problems in heart function.

Table 2.3: Predicted versus *in vitro* risk classifications for the analyzed drugs. Out of the six tested drugs, two drugs were classified differently based on the electromechanical results.

	Pred. high	Pred. intermediate	Pred. low
CiPA high	3	0	0
CiPA intermediate	1	0	0
CiPA low	0	1	1

We conclude that the addition of a mechanical biomarker, the maximum active tension, is valuable in the prediction of cardiac risk stratification. Additionally, using the electrophysiological biomarkers, SimCardEMS succeeded in predicting the same TdP risk category as previously determined for four of the six drugs.

References

1. Jordi Llopis Lorente, Beatriz Trenor, and Javier Saiz. Considering population variability of electrophysiological models improves the in silico assessment of drug-induced torsadogenic risk. *Computer Methods and Programs in Biomedicine*, 221:106934, 6 2022.
2. Dan M Rodfn. Torsade de pointes. *Clin. Cardiol*, 16:683–686, 1993.
3. Steven A Niederer, Joost Lumens, and Natalia A Trayanova. Computational models in cardiology. *Nature Reviews Cardiology* 2018 16:2, 16:100–111, 10 2018.
4. Elisa Passini, Cristian Trovato, Pierre Morissette, Frederick Sannajust, Alfonso Bueno Orovio, and Blanca Rodriguez. Drug-induced Shortening of the Electromechanical Window is an Effective Biomarker for in Silico Prediction of Clinical Risk of Arrhythmias. *Br J Pharmacol*, 7 2019.
5. Github - computationalphysiology/simcardems: Simula cardiac electromechanics solver.
6. Martin S Alnaes, Jan Blechta, Johan Hake, August Johansson, Benjamin Kehlet, Anders Logg, Chris Richardson, Johannes Ring, Marie E Rognes, and Garth N Wells. The fenics project version 1.5. *ANS*, 100:9–23, 2015.
7. Thomas O'Hara, László Virág, András Varró, and Yoram Rudy. Simulation of the undiseased human cardiac ventricular action potential: model formulation and experimental validation. *PLoS computational biology*, 7(5):e1002061, 2011.
8. S Land, S-J Park Holohan, NP Smith, CG Dos Remedios, JC Kentish, and S A Niederer. A model of cardiac contraction based on novel measurements of tension development in human cardiomyocytes. *J Mol Cell Cardiol*, 106:68–83, 1 2017.
9. Gerhard A Holzzapfel and Ray W Ogden. Constitutive modelling of passive myocardium: a structurally based framework for material characterization. *Philosophical Transactions of the Royal Society A: Mathematical, Physical and Engineering Sciences*, 367(1902):3445–3475, 2009.
10. Andrew E Epstein, John P DiMarco, Kenneth A Ellenbogen, NA Mark Estes, Roger A Freedman, Leonard S Gettes, A Marc Gillinov, Gabriel Gregoratos, Stephen C Hammill, David L Hayes, et al. Acc/aha/hrs 2008 guidelines for device-based therapy of cardiac rhythm abnormalities: a report of the american college of cardiology/american heart association task force on practice guidelines (writing committee to revise the acc/aha/naspe 2002 guideline update for implantation of cardiac pacemakers and antiarrhythmia devices) developed in collaboration with the american association for thoracic surgery and society of thoracic surgeons. *Journal of the American College of Cardiology*, 51(21):e1–e62, 2008.
11. Elisa Passini, Oliver J Britton, Hua Rong Lu, Jutta Rohrbacher, An N Hermans, David J Gallacher, Robert JH Greig, Alfonso Bueno-Orovio, and Blanca Rodriguez. Human in silico drug trials demonstrate higher accuracy than animal models in predicting clinical pro-arrhythmic cardiotoxicity. *Frontiers in physiology*, page 668, 2017.
12. Lucia Romero, Jordi Cano, Julio Gomis Tena, Beatriz Trenor, Ferran Sanz, Manuel Pastor, and Javier Saiz. In Silico QT and APD Prolongation Assay for Early Screening of Drug-Induced Proarrhythmic Risk. *Journal of Chemical Information and Modeling*, 58(4):867–878, 4 2018.

Open Access This chapter is licensed under the terms of the Creative Commons Attribution 4.0 International License (<http://creativecommons.org/licenses/by/4.0/>), which permits use, sharing, adaptation, distribution and reproduction in any medium or format, as long as you give appropriate credit to the original author(s) and the source, provide a link to the Creative Commons license and indicate if changes were made.

The images or other third party material in this chapter are included in the chapter's Creative Commons license, unless indicated otherwise in a credit line to the material. If material is not included in the chapter's Creative Commons license and your intended use is not permitted by statutory regulation or exceeds the permitted use, you will need to obtain permission directly from the copyright holder.





Chapter 3

In silico Investigation of Sex-Specific Osteoarthritis in Human Articular Chondrocytes

Khoa Ngo, Nathaniel T Herrera, Milda Folkmanaite, Kei Yamamoto, and Mary M Maleckar

Abstract Osteoarthritis (OA), a progressive degenerative disease of cartilage in joints, is the most common cause of chronic disability in older adults. While OA is mostly considered an age-related pathology, women have a 1.5-fold higher risk of developing OA relative to men and experience more severe symptoms. Yet, they remain underrepresented in musculoskeletal research and clinical trials. Responsible for cartilage formation, articular chondrocytes experience physiological changes in OA, but the functional implications of such alterations remain largely unexplored due to difficulties in acquiring the data experimentally. Through reparameterization, we expand a mathematical chondrocyte model to investigate sex-specific OA pathogenesis. We performed sensitivity analysis to address the impact of ion channel activity in healthy and OA chondrocyte populations. Simulations show that in healthy female chondrocytes, the resting membrane potential is more depolarized than in healthy male chondrocytes, suggesting potential sex-specific emergent physiological differences in articular chondrocytes. In both sexes, the resting membrane potential of healthy chondrocytes is most sensitive to I_{Ca-ATP} , I_{Na-b} , I_{NaK} and I_{K-b} , but in OA it depolarizes and becomes sensitive to I_{KDR} , I_{NaK} and I_{K-b} . Developed and evaluated against experimental data, our articular chondrocyte OA electrophysiology-

Khoa Ngo

Department of Physiology and Membrane Biology, University of California, Davis, USA

Nathaniel T Herrera

Department of Pharmacology, University of California, Davis, USA

Milda Folkmanaite

Department of Physiology, Anatomy and Genetics, University of Oxford, UK

Kei Yamamoto

Department of Computational Physiology, Simula Research Laboratory, NO

Mary M Maleckar (corresponding author)

Department of Computational Physiology, Simula Research Laboratory, NO e-mail: mmaleck@simula.no

ical model can be used to further study OA pathology and sex-specific pathological OA changes.

3.1 Introduction

Mammalian chondrocytes are found within intervertebral discs and articular cartilage, where they maintain the extracellular matrix (ECM) and produce the cartilage matrix [1]. The ECM mainly consists of collagen fibers that transmit force and dissipate energy, proteoglycans that withstand compressional forces, and synovial fluid to reduce friction between bones. In normal function, healthy chondrocytes respond to outside stimuli and damaged articular cartilage, where they increase production of specific ECM complexes [2]. Functional, mature, healthy articular chondrocytes are necessary for the maintenance of cartilage and therefore, physiological joint motion [3]. Chondrocytes function to maintain a homeostatic environment in the articular cartilage. Pathophysiological conditions can lead to the development of osteoarthritis (OA); however, the mechanism by which this occurs is poorly understood. Osteoarthritis is the most common form of arthritis and is a disease characterized by the degeneration of cartilage and underlying bone [4]. Women are 1.5x more likely to develop OA, and experience more severe symptoms as compared to men [5, 6, 7]. In OA, chondrocytes secrete increased levels of inflammatory cytokines, actively produce proteoglycans and collagen type II to recover the degeneration of the ECM, and become hypertrophic [8]. The present study on human, sex-specific OA is modeled after the specific cell physiology of the human articular chondrocyte.

Recent research suggests that maintaining a stable resting membrane potential is essential for chondrocytes in articular cartilage to be able to withstand pressure and force changes [9]. Despite chondrocytes being non-excitabile cells, they undergo robust ion-channel mediated changes in response to OA. This is further supported by experiments where ion-channels contributing to the resting membrane potential were blocked, resulting in a decrease in the production of matrix mRNAs, proteins and glycosaminoglycans [10, 11]. Additionally, channel blockers inhibit chondrocyte proliferation and increase apoptosis [12, 13]. During OA, chondrocytes have reduced capability to respond to changes in the extracellular environment, specifically with respect to ion transport; this is recognized by i.e. a deficiency in volume regulation [14]. Chondrocyte diameters vary between 7 and 30 μm , making technical electrophysiological experimental studies difficult [15]. Therefore, there is limited experimental data investigating the electrophysiological differences of chondrocytes in normal physiology and pathophysiology.

Therefore, to gain a better understanding of the human chondrocyte channelome in the context of OA, we have developed an OA chondrocyte model by further expanding a previously established mathematical model of the human articular chondrocyte [3, 16]. Mathematical models can play a key role in the dearth of physical data and in hypothesis generation, among other utilities. In the absence of constraining data, models can be used to generate valuable hypotheses about the underlying processes

at work, which can then be tested in carefully designed experiments and/or against data from other sources. This initial model of the human articular chondrocyte features various ion channels describing the resting membrane potential and ion movement across the cell membrane. Previous iterations of the model focused on potassium fluxes across the cell membrane, and included functions specifically for the integration of the sodium/potassium pump, an active transport pump that establishes an electrochemical gradient across the cell membrane. In this study, the model is expanded to include sex-specific OA by implementing the differences in ion channel conductances observed between males and females, as well as alterations of ion channel expression in OA disease. Populations of models using a log-normal distribution were also implemented to accurately represent biological variability, and subsequent parameter sensitivity analysis was performed to identify the currents that influence chondrocyte resting membrane potential to the greatest degree in both health and disease.

In summary, we have developed a mathematical OA chondrocyte model to gain a better understanding of OA pathogenesis through exploratory simulations, driving forward hypothesis development in the context of relative scarcity of human chondrocyte electrophysiological data across the channelome. As OA is more prevalent in females than males, we also implemented sex differences in our updated model. Our main goals in the present study were to: (i) update and scale the baseline male model (1) to generate a (2) disease OA-male model, (3) a control female model, and (4) a disease OA-female model, (ii) utilize a population of models approach to determine which ion channels were the main contributors to resting membrane potential in human articular chondrocytes during normal function and in OA.

3.2 Methods

To study the effects of OA on the resting membrane potential, we employed the chondrocyte model and simulation protocols developed by Maleckar *et al.* [3] and further improved by Fischer-Holzhausen *et al.* [17]. The model components are shown in Figure 3.1. I_{NaK} has been scaled to be within 0.1-0.6 of the original value, corresponding roughly to 0.9–5.35 pA/pF, as prior work has shown this range is more likely to present a physiologically-relevant model regime [17].

Following the Hodgkin-Huxley formalism, the cell membrane is modeled as a capacitor coupled in parallel with ion channels represented by resistors. The time-evolution of the transmembrane potential is given by the summation of all electrogenic transport processes.

$$C_m \frac{dV}{dt} = -(I_{KDR} + I_{NaK} + I_{NaCa} + I_{Ca-ATP} + I_{K-ATP} + I_{K2pore} + I_{Nab} + I_{Kb} + I_{Clb} + I_{KCa}), \quad (3.1)$$

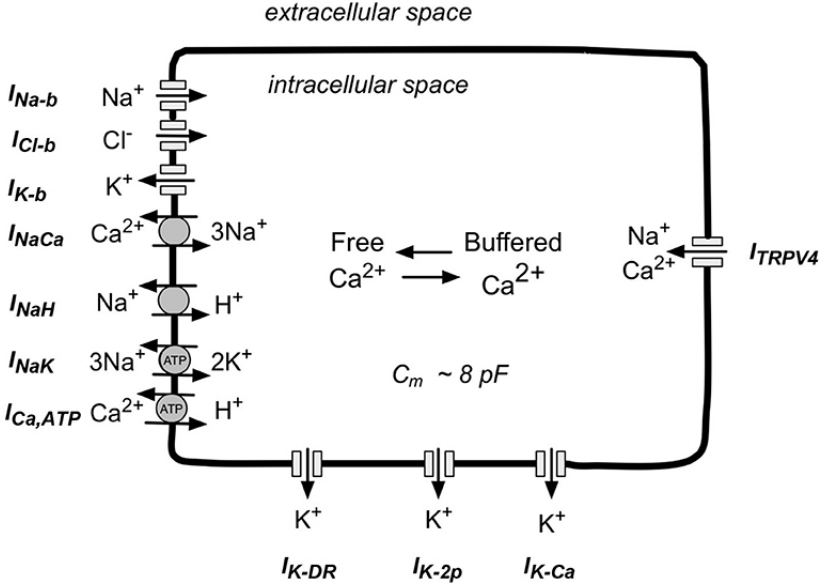


Fig. 3.1: Schematic illustration of the model adapted from Maleckar *et al.* [17], showing the principal ion-selective channels, exchangers, and pumps expressed in human chondrocytes.

where C_m is the chondrocyte capacitance (6.3 pF). A set of three transport equations gives the time-derivatives of the intracellular ionic concentrations of Na^+ , K^+ , and Ca^{2+}

$$\frac{d[Na^+]_i}{dt} = -\frac{I_{Na-b} + 3I_{NaK} + 3I_{NaCa} - I_{NaH} + I_{Cl-b}}{vol_i \times F}, \quad (3.2)$$

$$\frac{d[K^+]_i}{dt} = -\frac{I_{K-b} - 2I_{NaK} + I_{KDR} + I_{K2pore} + I_{KCa} + I_{K-ATP}}{vol_i \times F}, \quad (3.3)$$

$$\frac{d[Ca^{2+}]_i}{dt} = -\frac{I_{Ca-ATP} - 2I_{NaCa}}{2vol_i \times F} - 0.045 \times \frac{dO_c}{dt}, \quad (3.4)$$

where vol_i is the internal volume of the chondrocyte (0.005884 mL), F is the Faraday constant (96,485 C/mol), and O_c is the fraction of intracellular calmodulin bound to Ca^{2+} . The coefficients in front of the exchangers come from their respective ionic exchange ratios. For example, the NaK exchangers exchange three Na^+ ions for two K^+ ions.

3.2.1 Modeling Ionic Changes Induced by Osteoarthritis in Male and Female Chondrocytes

To gain mechanistic insight into the pathogenesis of OA, we implemented changes in ion channel expressions as measured by Karlsson *et al.* [18]. We further expanded our investigation by integrating sex-specific differences in ion channel activity into our model. Due to the lack of experimental data on female chondrocytes, we compiled a list of sex-specific differences in ion channel expression based on mRNA and ion channel subunit expression data collected from epicardial cardiomyocytes. In our model, we modeled the effect of changes in ion channel expression on their conductances (G), as displayed in Table 7.2.

Table 3.1: Sex-specific subcellular ion channel conductances relative to the male baseline model

Parameter	Male Control	Male OA	Female Control	Female OA
G_{NaK}	1	2.20	0.95	2.08
G_{Ca-ATP}	1	2	1	2
$G_{K-2Pore}$	1	0.20	1	0.20
G_{KDR}	1	8.30	0.80	6.64
G_{K-ATP}^*	1	0.34	1	0.34
G_{NaCa}	1	1	0.97	1
G_{K-b}	1	1	0.51	1

Implemented as change to the Q10 parameter which defines the effect of temperature on ion channel kinetics [19, 20].

3.2.2 Generation of a Population of Models

To capture biological variability and investigate parameter sensitivity, we used the published chondrocyte model [3, 17] as a baseline to build our population of 1,000 models by randomly modifying parameters corresponding to conductances of ion current and maximal rates of ion transports. A relatively large sample size of 1,000, typically used in similar population-based studies [21, 22], was chosen to allow even small effects, often indistinguishable in small sample sizes, to reach statistical significance. Prior studies have shown that biological parameters, when randomly selected, are distributed according to log-normal frequency curves instead of normal ones [23]. For each channel in the model, we varied its conductance by sampling from a log-normal distribution centered around their respective baseline value with the standard deviation set to 0.15.

3.2.3 Model Parameter Sensitivity Analysis

We performed parameter sensitivity analysis on the generated model population to assess the sensitivity of the model output (e.g., the resting membrane potential) in response to channel conductance variations. The degree to which perturbing a set parameter can influence the results are quantified as a set of regression coefficients, which are obtained by performing multivariable partial least squares regression on the dataset. Partial least squares regression was chosen over standard multivariable regression as many independent parameters (e.g., ion channel conductances) were used to predict a smaller set of dependent variables (e.g., the resting membrane voltage) [24]. This methodology was first used in cardiac electrophysiology by Sobie *et al.* [25] and has been widely used in other fields of biology [21, 26].

3.3 Results

3.3.1 Modeling the Impact of Sex-Specific OA on Resting Membrane Potential

In Figure 3.2, we implemented the experimentally-observed changes in ion channel expression in control and OA chondrocytes, accounting for sex differences as described in Table 7.2. Figure 3.2 shows that the healthy female chondrocyte maintains a more depolarized resting membrane potential (-58.21 ± 5.75 mV) as compared to the healthy male chondrocyte (-69.11 ± 4.71 mV). Electrophysiological differences instigated by OA result in depolarization in both male (from -69.11 ± 4.71 mV to -53.87 ± 3.21 mV) and female (from -58.21 ± 5.75 mV to -49.03 ± 1.34 mV) chondrocytes. This overall depolarizing effect of OA remodeling on the resting membrane potential has previously been reported in experiments [27].

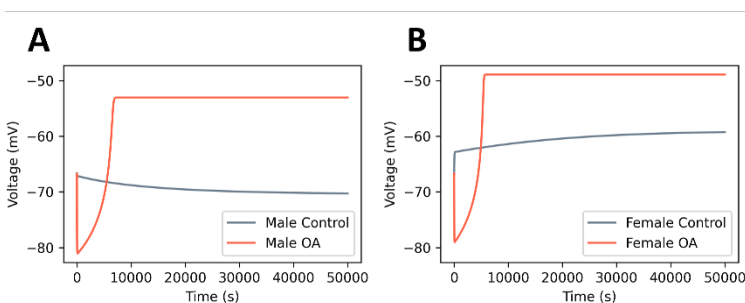


Fig. 3.2: Resting membrane potential in control and OA chondrocytes for (A) male and (B) female models. Changes in ion channel expression in OA induce resting membrane depolarization.

3.3.2 Population of Models

Shown in Figure 3.3, and as outlined previously, we further expanded our analysis to investigate population variability by generating 1,000 models for each condition with channel conductances varied according to a log-normal distribution. For all 1,000 parameter sets, the steady-state solutions were reached within the simulation period of 50,000 seconds. Figure 3.3 shows that in male and female OA chondrocytes, intracellular sodium quickly becomes depleted and remains very small, close to zero, for the rest of the simulation. We calculated the mean resting membrane potentials for all conditions and compared them against the reported experimental values as measured in experiments, shown in Figure 3.4. In all cases, the membrane potentials of OA chondrocytes are relatively more depolarized compared to their healthy counterparts. Comparing male and female chondrocytes, although the control resting membrane potential values slightly differ (females are more depolarized compared to males), OA male and female chondrocytes depolarize to a similar value (approximately -51 mV).

3.3.3 Parameter Sensitivity Analysis

Sensitivity analyses were performed on the chondrocyte populations to reveal how ionic modulations induced by OA might affect the sensitivities of underlying electrophysiological properties in the models. Shown in Figure 3.5, in the healthy male chondrocyte population, I_{NaK} , I_{Ca-ATP} , I_{Na-b} , and I_{K-b} are predicted to have the most critical impact on the resting membrane potential. In this case, I_{Na-b} is the strongest depolarizing current and I_{Ca-ATP} is the strongest hyperpolarizing current. In male chondrocytes expressing OA, only I_{NaK} and I_{K-b} remain the most influential currents. Compared to the healthy case, the impact of I_{Ca-ATP} and I_{Na-b} are severely reduced in OA, while I_{NaK} gains a 1.6-fold depolarizing influence.

The healthy female chondrocyte population shares some similarities with their male counterparts, as the resting membrane potential is still the most sensitive to I_{NaK} , I_{Ca-ATP} , I_{Na-b} , and I_{K-b} . However, I_{K-ATP} now plays a slightly more dominant role as a hyperpolarizing current. Compared to male chondrocytes, I_{NaK} gains a more significant role in establishing the resting membrane potential than in males (2.5-fold increase in importance). I_{NaK} is the strongest depolarizing current and I_{K-b} is the strongest hyperpolarizing current. Surprisingly, in female chondrocytes expressing OA, the majority of the currents no longer have as much of an impact on the resting membrane potential. Nonetheless, I_{NaK} and I_{K-b} each still retain a minor influence.

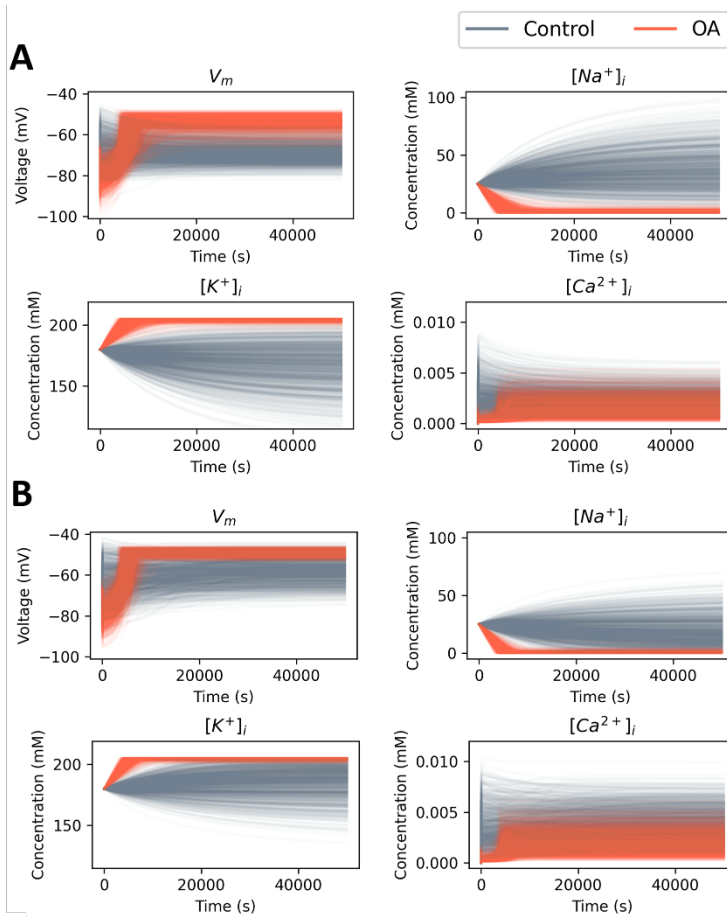


Fig. 3.3: Membrane voltage and internal ion concentrations for (A) male and (B) female population.

3.3.4 Inhibiting I_{NaK} Restores Normal Resting Membrane Potential in OA Chondrocytes

Per sensitivity analysis results, I_{NaK} has the largest impact on depolarizing the resting membrane potential (i.e., having positive regression coefficients) in both male and female chondrocytes in OA. To restore the membrane potential back to near control values, we applied I_{NaK} current block treatment then simulated the membrane potential in male and female OA populations of 1,000 models each. Figure 3.6 shows that applying 45% I_{NaK} block to male and 55% I_{NaK} block to female OA chondrocytes restored the mean resting membrane potential of the population back to the control level. Notably, previous clinical studies have revealed that I_{NaK}

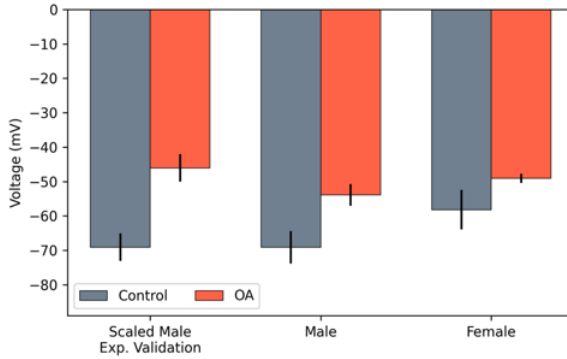


Fig. 3.4: Mean resting membrane potential in control and OA chondrocytes for male and female populations (1,000 models each) compared against experimental data [27]. To account for differences in data collection methodology, experimental resting membrane potential values were scaled to match the mean of the male population.

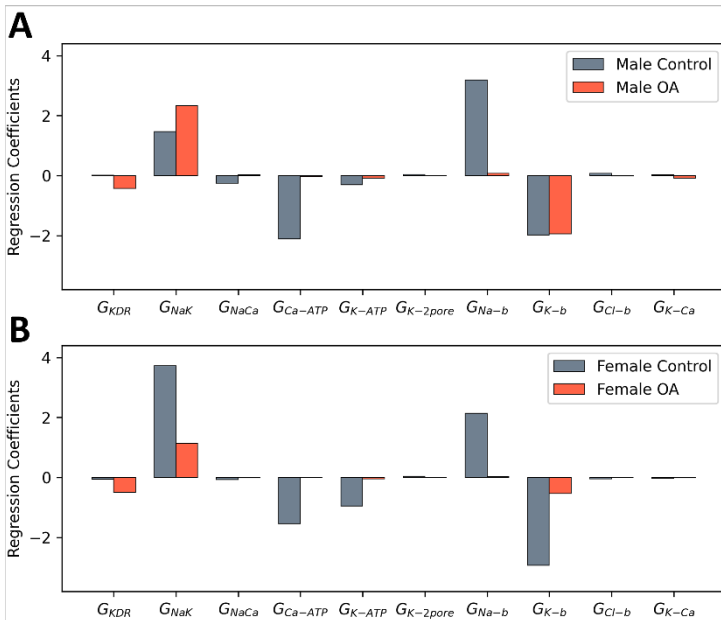


Fig. 3.5: Parameter sensitivity analysis on (A) male and (B) female population of sex-specific chondrocyte models. The regression coefficients measure the relative impact of a particular ionic current on the resting membrane potential. A positive regression coefficient indicates the associated current is a depolarizing current, while a negative regression coefficient indicates a hyperpolarizing current.

blockers Ouabain and Digoxin protected against OA and relieved OA-associated pain [28].

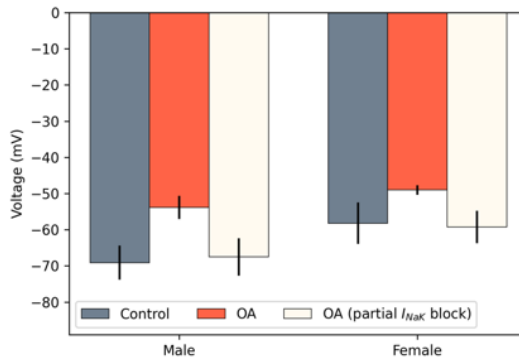


Fig. 3.6: Resting membrane potential in control, OA, and OA chondrocytes with partial block of I_{NaK} for male and female model population (1,000 models each). Blocking I_{NaK} (45% for male and 55% for female population) helped restore the resting membrane potential back to normal levels in OA chondrocytes.

3.4 Discussion

OA, a debilitating disorder affecting 1 in 7 individuals in the United States in their lifetime [29], has no current curative treatment. The prevalence, as well as disease severity, is more pronounced in female patients [30]. It is known that chondrocytes play an essential role in maintaining healthy cartilage, and that their function is impaired in disease [31]. As experimental investigation of human chondrocytes is challenging due to the lack of human control samples, we have further expanded a previously-developed mathematical model of a chondrocyte channelome by introducing experimental changes observed in ion channel electrophysiology, as well as temperature and capacitance [3]. The updated model is user-friendly and freely accessible (github.com/k-ngo/Chondrocyte).

Simulations revealed that the chondrocyte membrane becomes depolarized in OA, which agrees with experimental data [32]. This suggests that the changes in ion channel expression together with temperature and capacitance are sufficient to capture the main pathological alterations observed in OA chondrocytes related to their membrane potential. In the future, it remains important to further validate the model experimentally, as well as to investigate the primary cause of the alterations in ion channel expression observed in OA chondrocytes. These are likely to involve inflammatory processes associated with OA [33].

Comparisons between male and female chondrocyte models reveal intriguing phenotypic differences. First, the resting membrane potential is more depolarized in females compared to males in controls. The main differences between male and female healthy chondrocyte models include reduced G_{KDR} (by 25%), G_{K-b} (by 95.2%), G_{NaCa} (by 2.8%) and G_{NaK} (by 5.7%). The investigation of the main factors important for maintaining membrane potential visualized in Figure 3.5 revealed that, in the present model, calcium ATPase and background sodium and potassium currents contribute the most for maintaining healthy resting membrane potential in males, with an addition of I_{NaK} in females. It could be that the relative depolarization of the female chondrocyte membrane driven by the aforementioned changes in the model predisposes female patients to OA, although additional experimental data is needed to further investigate this hypothesis.

OA chondrocyte model simulations show that resting membrane potential is depolarized in disease, following experimental data [32]. This effect is seen in both male and female OA models. Our results also suggest that chondrocyte resting membrane potential in female patients could be more depolarized compared to that in males, which could lead to higher depolarization in OA (mean resting membrane potential is -49.03 ± 1.34 mV in the female and -53.87 ± 3.21 mV in the male OA model). The resting membrane potential in OA was around 17.5% more depolarized for female and 24.5% for male model compared to respective healthy resting membrane potentials. In our OA model, I_{NaK} current plays a prominent role in regulating membrane voltage: in both males and females with OA, increased I_{NaK} becomes the most important contributing factor to the overall depolarization of the resting membrane potential, as revealed by sensitivity analysis. Inhibiting I_{NaK} might therefore provide a useful approach for reversing resting membrane alterations in OA and, more broadly, I_{NaK} could be a useful target in modulating disease pathogenesis in OA.

I_{NaK} inhibitors are well characterized for e.g. cardiac disease treatment, and new selective inhibitor drugs are currently in the pipeline [28]. To test whether I_{NaK} block could be useful in overcoming OA-associated changes in resting membrane potential, we simulated I_{NaK} block. With varying degrees of I_{NaK} inhibition, the resting membrane potential in disease can be restored to healthy, pre-OA levels in both males and females. Therefore, re-purposing I_{NaK} blockers feasibly provide a useful new therapeutic approach for OA treatment. I_{NaK} blockers have, in fact, already been applied for OA treatment: clinical studies have reported positive outcomes in patients, revealing that I_{NaK} blockers, Ouabain and Digoxin, induced a reduction in pain and elicited an apparent OA-protective effect [28], supporting our simulation results implying I_{NaK} blockers as a potential treatment for OA.

Given this putative critical role of Na⁺ concentration in healthy and OA chondrocytes, novel future experiments should consider thoroughly probing Na⁺ balance in human chondrocytes. For instance, Figure 3.3 shows that in male and female OA chondrocytes, intracellular sodium quickly becomes depleted and remains very small, close to zero, for the rest of the simulation, suggesting that alternate sodium regulation not currently accounted for in base models may apply in OA. Model development should additionally move towards incorporating new channel species

to regulate Na^+ concentrations in control and in OA, including epithelial sodium channels (ENaC), which are not currently included in the model [31, 34]. Other work has also focused on voltage-gated sodium channels in chondrocytes, which may also be considered.

Naturally, the lack of available biological data from new electrophysiological and other experimental studies presents a challenge for the validation of both male and female models, both in control and in OA. Further experimental studies will be instrumental in determining the ranges of parameters for the model, as well as for simulated chondrocyte behavior evaluation. In the future, further experimental data will be helpful in further developing and expanding the current chondrocyte model. While the current study, synthetic in nature, limits its direct translation to clinical application, the present work retains utility in terms of physiological exploration and hypothesis generation.

In summary, further incorporating additional species key in the chondrocyte channelome into the model and incorporating new data from emerging experiments will permit even greater insights into the broad and nuanced role of membrane dynamics in chondrocyte function and pathophysiology.

3.5 Conclusions

We have further expanded a previously published chondrocyte mathematical model enabling simulations of the osteoarthritic chondrocyte channelome. Implemented changes were based on published data, and model simulation results show that the resting membrane potential in chondrocytes becomes depolarized in OA in both male and female chondrocytes, which agrees with the experimental data acquired from males. Our sex-specific chondrocyte model reveals differences in resting membrane potential between males and females that could potentially contribute to the higher prevalence of OA in female patients. Finally, sensitivity analyses revealed the main currents responsible for maintaining resting membrane potential in chondrocytes and potential novel therapeutic targets for OA treatment. Our OA chondrocyte electrophysiological model provides an accessible tool for subsequent studies of OA pathogenesis and drug targeting.

References

1. Ahmed Nahian and Amit Sapra. *Histology, Chondrocytes*. StatPearls Publishing, Treasure Island (FL), 2022.
2. Hemanth Akkiraju and Anja Nohe. Role of chondrocytes in cartilage formation, progression of osteoarthritis and cartilage regeneration. *Journal of developmental biology*, 3(4):177–192, Dec 2015.
3. Mary M Maleckar, Robert B Clark, Bartholomew Votta, and Wayne R Giles. The resting potential and k⁺ currents in primary human articular chondrocytes. *Frontiers in Physiology*, 9:974, Sep 2018.
4. Virginia Byers Kraus, Francisco J Blanco, Martin Englund, Morten A Karsdal, and L Stefan Lohmander. Call for standardized definitions of osteoarthritis and risk stratification for clinical trials and clinical use. *Osteoarthritis and cartilage / OARS, Osteoarthritis Research Society*, 23(8):1233–1241, Aug 2015.
5. Kamil E Barbour, Charles G Helmick, Michael Boring, and Teresa J Brady. Vital signs: Prevalence of doctor-diagnosed arthritis and arthritis-attributable activity limitation - united states, 2013-2015. *MMWR. Morbidity and mortality weekly report*, 66(9):246–253, Mar 2017.
6. Jennifer M Hootman, Charles G Helmick, Kamil E Barbour, Kristina A Theis, and Michael A Boring. Updated projected prevalence of self-reported doctor-diagnosed arthritis and arthritis-attributable activity limitation among us adults, 2015-2040. *Arthritis & Rheumatology (Hoboken, N.J.)*, 68(7):1582–1587, Jul 2016.
7. Kristina A Theis, Douglas W Roblin, Charles G Helmick, and Ruiyan Luo. Prevalence and causes of work disability among working-age u.s. adults, 2011-2013, nhis. *Disability and Health Journal*, 11(1):108–115, Jan 2018.
8. Mohit Kapoor, Johanne Martel-Pelletier, Daniel Lajeunesse, Jean-Pierre Pelletier, and Hassan Fahmi. Role of proinflammatory cytokines in the pathophysiology of osteoarthritis. *Nature Reviews. Rheumatology*, 7(1):33–42, Jan 2011.
9. Richard Barrett-Jolley, Rebecca Lewis, Rebecca Fallman, and Ali Mobasheri. The emerging chondrocyte channelome. *Frontiers in Physiology*, 1:135, Oct 2010.
10. JK Mouw, SM Imler, and ME Levenston. Ion-channel regulation of chondrocyte matrix synthesis in 3d culture under static and dynamic compression. *Biomechanics and Modeling in Mechanobiology*, 6(1–2):33–41, Jan 2007.
11. QQ Wu and Q Chen. Mechanoregulation of chondrocyte proliferation, maturation, and hypertrophy: ion-channel dependent transduction of matrix deformation signals. *Experimental Cell Research*, 256(2):383–391, May 2000.
12. Valentina Grishko, Min Xu, Glenn Wilson, and Albert W Pearsall. Apoptosis and mitochondrial dysfunction in human chondrocytes following exposure to lidocaine, bupivacaine, and ropivacaine. *The Journal of Bone and Joint Surgery. American Volume*, 92(3):609–618, Mar 2010.
13. D Wohlrab, M Vocke, T Klapperstück, and W Hein. The influence of lidocaine and verapamil on the proliferation, cd44 expression and apoptosis behavior of human chondrocytes. *International Journal of Molecular Medicine*, 16(1):149–157, Jul 2005.
14. Rebecca Lewis, Katie E Asplin, Gareth Bruce, Caroline Dart, Ali Mobasheri, and Richard Barrett-Jolley. The role of the membrane potential in chondrocyte volume regulation. *Journal of Cellular Physiology*, 226(11):2979–2986, Nov 2011.
15. Mehmet Selcuk Şenol and Hamza Özer. *Chapter 7 - Architecture of cartilage tissue and its adaptation to pathological conditions*, page 91–100. Academic Press, Jan 2020.
16. Mary M Maleckar, Robert B Clark, Bartholomew Votta, and Wayne R Giles. The resting potential and k⁺ currents in primary human articular chondrocytes. *Frontiers in Physiology*, 9:974, Sep 2018.
17. Sophie Fischer-Holzhausen, Kei Yamamoto, Maria P Fjeldstad, and Mary M Maleckar. Probing the putative role of k⁺ atp channels and biological variability in a mathematical model of chondrocyte electrophysiology. *Bioelectricity*, 3(4):272–281, Dec 2021.

18. C Karlsson, T Dehne, A Lindahl, M Brittberg, A Pruss, M Sittinger, and J Ringe. Genome-wide expression profiling reveals new candidate genes associated with osteoarthritis. *Osteoarthritis and Cartilage*, 18(4):581–592, Apr 2010.
19. Mary M Maleckar, Pablo Martín-Vasallo, Wayne R Giles, and Ali Mobasheri. Physiological effects of the electrogenic current generated by the Na^+/K^+ pump in mammalian articular chondrocytes. *Bioelectricity*, 2(3):258–268, Sep 2020.
20. David C Sterratt. *Q10: The Effect of Temperature on Ion Channel Kinetics*, page 1–3. Springer, New York, NY, 2013.
21. Haibo Ni, Stefano Morotti, and Eleonora Grandi. A heart for diversity: Simulating variability in cardiac arrhythmia research. *Frontiers in Physiology*, 9:958, Jul 2018.
22. Stefano Morotti and Eleonora Grandi. Logistic regression analysis of populations of electrophysiological models to assess proarrhythmic risk. *MethodsX*, 4:25–34, 2017.
23. CL Zhang and FA Popp. Log-normal distribution of physiological parameters and the coherence of biological systems. *Medical Hypotheses*, 43(1):11–16, Jul 1994.
24. Paul Geladi and Bruce R Kowalski. Partial least-squares regression: a tutorial. *Analytica Chimica Acta*, 185:1–17, 1986.
25. Eric A Sobie. Parameter sensitivity analysis in electrophysiological models using multivariable regression. *Biophysical Journal*, 96(4):1264–1274, Feb 2009.
26. Kevin A Janes, John G Albeck, Suzanne Gaudet, Peter K Sorger, Douglas A Lauffenburger, and Michael B Yaffe. A systems model of signaling identifies a molecular basis set for cytokine-induced apoptosis. *Science*, 310(5754):1646–1653, Dec 2005.
27. Julio C Sánchez and Diego F López-Zapata. Effects of osmotic challenges on membrane potential in human articular chondrocytes from healthy and osteoarthritic cartilage. *Biorheology*, 47(5–6):321–331, Jan 2010.
28. Kai-di Wang, Xiang Ding, Nan Jiang, Chao Zeng, Jing Wu, Xianyuan Cai, Aubryanna Hettlinghouse, Asya Khleborodova, Zi-Ning Lei, Zhe-Sheng Chen, Guang-hua Lei, and Chuan-ju Liu. Digoxin targets low density lipoprotein receptor-related protein 4 and protects against osteoarthritis. *Annals of the rheumatic diseases*, 81(4):544–555, Apr 2022.
29. Reva C Lawrence, David T Felson, Charles G Helmick, Lesley M Arnold, Hyon Choi, Richard A Deyo, Sherine Gabriel, Rosemarie Hirsch, Marc C Hochberg, Gene G Hunder, Joanne M Jordan, Jeffrey N Katz, Hilal Maradit Kremers, and Frederick Wolfe. Estimates of the prevalence of arthritis and other rheumatic conditions in the united states, part ii. *Arthritis and Rheumatism*, 58(1):26–35, Jan 2008.
30. Mary I O’Connor. Sex differences in osteoarthritis of the hip and knee. *The Journal of the American Academy of Orthopaedic Surgeons*, 15 Suppl 1:S22–25, 2007.
31. Ali Mobasheri, Csaba Matta, Ilona Uzielienė, Emma Budd, Pablo Martín-Vasallo, and Eiva Bernotiene. The chondrocyte channelome: A narrative review. *Joint Bone Spine*, 86(1):29–35, Jan 2019.
32. Rula Abdallat, Emily Kruchek, Csaba Matta, Rebecca Lewis, and Fatima H Labeed. Dielectrophoresis as a tool to reveal the potential role of ion channels and early electrophysiological changes in osteoarthritis. *Micromachines*, 12(8):949, Aug 2021.
33. Jeremy Sokolove and Christin M Lepus. Role of inflammation in the pathogenesis of osteoarthritis: latest findings and interpretations. *Therapeutic Advances in Musculoskeletal Disease*, 5(2):77–94, Apr 2013.
34. Pablo Martín-Vasallo, E Trujillo, D Álvarez de la Rosa, A Mobasheri, T González, and CM Canessa. Sodium transport systems in human chondrocytes ii. expression of $Na^+/K^+/2Cl^-$ -cotransporter and Na^+/H^+ exchangers in healthy and arthritic chondrocytes. *Histology and histopathology*, 14(4):1023–1031, 1999.

Open Access This chapter is licensed under the terms of the Creative Commons Attribution 4.0 International License (<http://creativecommons.org/licenses/by/4.0/>), which permits use, sharing, adaptation, distribution and reproduction in any medium or format, as long as you give appropriate credit to the original author(s) and the source, provide a link to the Creative Commons license and indicate if changes were made.

The images or other third party material in this chapter are included in the chapter’s Creative Commons license, unless indicated otherwise in a credit line to the material. If material is not included in the chapter’s Creative Commons license and your intended use is not permitted by statutory regulation or exceeds the permitted use, you will need to obtain permission directly from the copyright holder.





Chapter 4

Recapitulating Functional Heterogeneity in Electrophysiologically Active Tissues

Meye Bloothoof, Joseph G Shuttleworth, Gabriel Neiman, Ishan Goswami, and Andrew G Edwards

Abstract Inter-cellular heterogeneity is central to the dynamic range and robustness of function in many tissues, particularly electrically excitable tissues. In pancreatic islet β -cells, inter-cellular heterogeneity underlies the range of insulin response to glucose. In human-induced-pluripotent stem cell-derived cardiomyocytes (hiPSC-CMs), inter-cellular heterogeneity presents a key challenge for drug screening applications. In this study, we assess the ability to reconstruct inter-cellular heterogeneity *in silico* by applying a “population of models” (PoMs) framework, i.e. collections of computational cells created via Monte Carlo variation of model parameters. We define parameter variation based on experimentally observed heterogeneity in properties such as ion current conductances and enzymatic affinities. We then assess the accuracy of those reconstructions, based on the degree to which variation in PoM outputs (e.g. action potential duration) matches experimentally observed variation. We report that this “ground-up” approach underestimates functional heterogeneity in the hiPSC-CM population, but overestimates it in adult human cardiomyocytes. In contrast, the β -cell PoM captures three distinct and physiologically relevant subclasses of β -cell function. In the future, we expect PoM approaches like these will

Meye Bloothoof

Department of Medical Physiology, Division of Heart and Lungs, University Medical Centre Utrecht, NL

Joseph G Shuttleworth

Centre for Mathematical Medicine and Biology, School of Mathematical Sciences, University of Nottingham, Nottingham, UK

Gabriel Neiman

Department of Bioengineering, University of California, Berkeley, USA

Ishan Goswami

Department of Bioengineering, University of California, Berkeley, USA, Department of Materials Science and Engineering, University of California, Berkeley, USA

Andrew G Edwards (corresponding author)

Department of Computational Physiology, Simula Research Laboratory, NO e-mail: andy@simula.no

permit incorporation of realistic cellular heterogeneity in detailed models of intact tissues, and thereby aid development of sophisticated tissue-engineered platforms for therapeutics.

4.1 Introduction

Functional heterogeneity among cells within a tissue is a characteristic and relevant feature of living systems. Even within a genetically homogeneous population, individual cells often show a considerable amount of phenotypic heterogeneity [1], and this feature has implications in the plasticity and robustness of the organisms. Plasticity allows adaptive cellular responses to perturbations in the environment while maintaining a robustness in functional behaviour of the tissue even after a perturbation or insult. For example, when a region of the heart becomes infarcted (dies), non-infarcted healthy areas will adapt and increase their force of contraction to maintain blood flow to the body. This ability to adapt is a form of robustness of organ function, but must be achieved in a manner that maintains the heart's electrophysiologic stability. Similarly, in obesity induced diabetes, hyperlipidemia and hyperglycemia exert excessive insulin demand on pancreatic islet β -cells. In some β -cells this prolonged exertion leads to exhaustion of insulin reserve and cell death. Thus, increased demand for insulin must be achieved via an adaptive response in the remaining viable β -cells, which are phenotypically distinct. In both of these examples, cellular heterogeneity is central to the plasticity and robustness that allows both organs to maintain function after pathophysiological challenge. Functional heterogeneity may also broaden the range of responses to drugs [2]. For example, glibenclamide has differential effects on pancreatic islets owing to functional heterogeneity of their β -cell populations [3]. Thus, the study of cellular heterogeneity for both basic understanding of living systems and discovery of therapeutics has motivated the development of experimental techniques and the construction of computational models to simulate the dynamics and effects of cellular heterogeneity [4].

A range of single-cell experimental techniques are available to investigate this heterogeneity. These range from transcriptome assessment via single cell RNA sequencing, to classical cell electrophysiology via patch clamp. While these approaches are generally both time and labor intensive, data collected by those methods can be stored and interrogated via efficient modelling frameworks, such as the population of models approach (PoM) [5, 6]. These approaches simulate the dynamics and functional implications of heterogeneity in cell populations, including responses to pathologic insults and drug challenges.

In the PoM approach, heterogeneity is implemented by varying parameters (such as the ionic conductance of a single or multiple ion channel/s) of a baseline model, which itself captures the average characteristics of a particular cell type. Each unique configuration of parameters creates a new instance of the cell model, which is anal-

ogous to a new “member” cell of the population. In general, this procedure has been performed by first specifying equal distributions over which all parameters of interest (e.g. all ionic conductances) can vary, and then selecting only members of that population that exhibit behaviour within the experimentally observable range [5, 6]. For example, a cardiac myocyte population could be constructed by first allowing all ionic conductance parameters to be sampled from Gaussian distributions with an arbitrary standard deviation of 30% of each mean parameter value in the baseline model - this sampling strategy involves homogeneous variability across parameters. Some members of this PoM will exhibit parameter combinations that are biologically unrealistic, and thus possibly exhibit behaviour outside the experimentally observable range. To eliminate those models, it is common to reject models that produce outputs or features, such as a cardiomyocyte action potential duration, that are outside the range of experimental observations for the respective features. Continuing the example, a cardiomyocyte population member will be deemed non-viable if the action potential duration is far longer or shorter than observed experimentally. Similarly, a non-firing β -cell model will be rejected from the islet PoM. Because, in these examples, the PoMs are generated from arbitrary and homogeneous parameter distributions, they will exhibit appropriate behavioural characteristics, but may not involve truly biologically representative parameter combinations. Thus, the behaviours may not result from truly representative underlying dynamics.

In this work, we apply a different approach, with the intention of introducing more biologically realistic variability in PoMs of three different cell types: human adult cardiomyocytes, hiPSC-CMs and primary islet β -cells. By introducing variability to the input parameters that is grounded in *experimentally observed variability for each parameter*, we hope to span the biologically reachable configurations and limit the number of unrealistic configurations that are generated. That is, we use published experimental variation (standard deviations) for ionic conductance parameters and enzymatic activity/affinity parameters in order to apply parameter-specific heterogeneity rather than variation that is homogeneous across the varied parameters. Based on these constraining conditions, we demonstrate the feasibility of PoMs to generate a heterogeneous population representing different functional phenotypes.

4.2 Methods

An illustrative example of our approach in generating PoMs is shown in Figure 4.1. To recapitulate the functional heterogeneity in the tissue PoMs, we introduced parameter-specific variability into our models. To do this, we identified a set of parameters which we expect to account for much of the inherent biological variability influencing electrophysiologic function in these cell types. These parameters are a selection of maximal conductance (or flux) parameters for both the cardiomyocyte models (hiPSC-CM and adult) and the β -cell model. Additionally for the β -cell, a selection of kinetic parameters for enzyme reactions in the glycolysis cycle were varied to introduce metabolic heterogeneity. We chose to endow each of these pa-

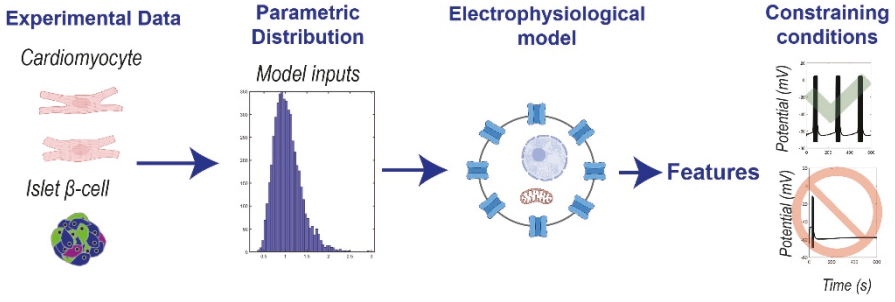


Fig. 4.1: Illustrative example of generating population of model (PoM) of human cardiomyocytes and islet β -cells. Experimental data obtained from literature was used to generate log-normal distributions of electrophysiological and/or metabolic parameters used as inputs to computational model. Sets of features are obtained from the simulations that are then used to generate viable candidates for the PoMs representative of cardiomyocyte or β -cells via constraining conditions.

rameters, p , with a log-normal distribution, such that $\log p \sim \bar{p}N(0, \sigma^2)$ where \bar{p} is the original, unmodified parameter from the baseline model and σ is a standard deviation derived from the literature. We term the random variable $\frac{p}{\bar{p}}$ the *scaling factor*. To assign values for the various σ , we surveyed the literature for measured variability of each parameter of interest. To mitigate the impact of systematic differences among the means of different datasets, and to keep our parameter distributions centred on the original parameter values, we computed the coefficient of variation for each parameter (σ_p):

$$\sigma_p := \frac{\sigma_{\text{lit}}}{\mu_{\text{lit}}} \quad (4.1)$$

where μ_{lit} and σ_{lit} are the mean and standard deviation, respectively, of the observations found in the literature.

The published mathematical models chosen as the baselines for the adult-CM and the hiPSC-CM were developed by [7] and [8], respectively. For the β -cell PoM, the electrophysiological model developed in [9] and glycolysis model developed in [10] were used to generate the heterogeneous population of β -cells. In the following subsections, we will detail the generation of parametric distributions and the constraining conditions via feature extraction for each PoM.

4.2.1 Cardiomyocytes

The O’Hara-Rudy model (ORd, [7]) is a widely-used mathematical description of the average human left ventricular cardiomyocyte. We specifically used the epicardial

version for our adult human baseline model. Likewise, the baseline model for hiPSC-CMs was that published in [8]. Both models use the following fundamental equation for calculation of time-varying membrane potential:

$$C_m \frac{dV}{dt} = - \sum_i I_i \quad (4.2)$$

where C_m is the capacitance of the cell membrane and each I_i is a current describing the transmembrane current carried by each species of ion channel present in the model. For each ion channel, there is a maximal conductance parameter g_i , or analogous permeability parameter, such that $I_i = g_i \hat{I}_i$ for some \hat{I}_i . \hat{I}_i is in turn described by a system of ordinary differential equations that specify the voltage, ion concentration and time-dependencies of ion channel function. For all currents, we only vary the maximal conductance (g_i), and not the parameters of the remaining equations contributing to \hat{I}_i . The formulation for sarcoplasmic reticulum (SR) calcium reuptake is different to those of the ion channels, but an analogous term that reflects the maximal rate of SR calcium reuptake \bar{J}_{SERCA} . As for the ion channel conductances, this parameter was varied to introduce heterogeneity in this key element of intracellular calcium handling.

Table 4.1: **Scaling parameters for the cardiomyocyte PoM**

Sources to construct coefficient of variation (σ_p) listed by the reference numbers

Variable	Mean	Unit	σ_p
human adult CM			
g_{K1}	3.60	pA/pF	0.78 ¹
g_{Kr}	0.31	pA/pF	0.13 ¹
g_{Ks}	0.18	pA/pF	0.65 ²
g_{ko}	9.30	pA/pF	0.99 ¹
g_{CaL}	10.20	pA/pF	0.13 ¹
g_{Na}	16.10	pA/pF	0.83 ³
g_{NaL}	0.34	pA/pF	0.49 ⁴
g_{NaK}	1.90	$\mu\text{M}/\text{min}/\text{mg}$ protein	0.48 ⁵
g_{NaCa}	0.05	nmol Ca ²⁺ /mg protein/sec	0.36 ^{6,7}
J_{SERCA}	7.10	nmol ATP/mg protein/min	0.39 ⁵
hiPSC-CM			
g_{Na}	166.00	pA/pF	0.26 ⁸⁻¹¹
g_{Ca}	12.20	pA/pF	0.41 ^{8,11-15}
g_{Kr}	2.02	pA/pF	0.47 ^{8,11,16-18}
g_{Ks}	1.30	pA/pF	0.58 ^{8,11,19}
g_f	2.50	pA/pF	0.32 ^{8,11}
g_{k1}	1.00	pA/pF	2.20 ^{8,11,17,20}
g_{to}	4.69	pA/pF	0.48 ^{8,14,21}
g_{NCX}	2.10	pA/pF	0.33 ²²
g_{NaL}	0.70	pA/pF	0.86 ¹⁰

¹[11], ²[12], ³[13], ⁴[14], ⁵[15], ⁶[16] ⁷[17], ⁸[18], ⁹[19], ¹⁰[20], ¹¹[21], ¹²[22], ¹³[23], ¹⁴[24], ¹⁵[25], ¹⁶[26], ¹⁷[27], ¹⁸[28], ¹⁹[29], ²⁰[30], ²¹[31], ²²[32]

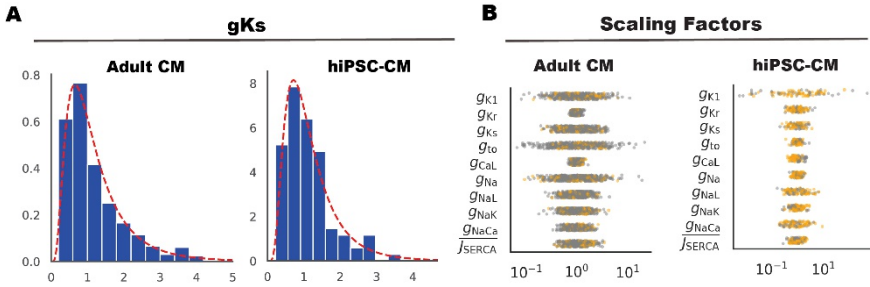


Fig. 4.2: A. The resultant log-normal distributions for the g_{Ks} scaling factor, along with histograms resulting from 100 samples, are shown for the representative parametric variation in adult CM and the hiPSC-CM inputs for the models. B. The scaling factors that were sampled in order to create the PoM are shown for two cardiomyocyte models. Parameters from the models that were excluded from the POM are shown in grey, whereas the parameters which were calibrated into the PoMs are highlighted in orange.

Table 4.1 provides the values for each varied parameter for both the adult human myocyte model and the hiPSC-CM model. The variability presented in this table may not completely capture the variability in each maximal conductance parameter. Nevertheless, these values provide a reasonable approximation, and yield plausible distributions for each of the relevant parameters. We took 500 samples from each of these distributions and the results are shown in Figure 4.2A alongside the relevant sampling distributions.

The PoMs generated by varying the input parameters as summarized in Table 4.1 were solved via MATLAB stiff-solver ode15s, and allowed to equilibrate by simulating for 500s before computing the output features. Calibrated PoMs for both the adult CM and hiPSC-CM were obtained by rejecting models that produced features outside the experimentally observed range. We identified a collection of features from the literature: *maximum upstroke velocity (voltage)*, *minimum diastolic potential*, *voltage amplitude*, *action potential duration (APD_{90})*, *maximal departure velocity for Ca^{2+}* , *diastolic Ca^{2+} concentration*, *Ca^{2+} transient amplitude*, *Ca^{2+} transient time-to-peak*, and *time constant of Ca^{2+} decay*. Representative scaling factors sampled from the output of the models obtained via the constraining criterion are shown in Figure 4.2B. In the results section, we discuss the typical features obtained and constraining criteria to generate calibrated PoMs for the cardiomyocytes.

4.2.2 Islet β -cells

A robust secretion of insulin by the β -cell upon glucose challenge relies heavily on the coupling of the metabolic oscillations in the glycolysis pathway with electrical oscillations (e.g. isolated action potentials and action potential bursting). Recognizing this, the β -cell PoM was generated via a coupling of the electrophysiological model developed in [9] and glycolysis model developed in [10]. A coupling of these models was demonstrated in [33], albeit using single mean values for the electrical and glycolytic component parameters. A simplistic illustration of this coupled model is shown in Figure 4.3. To delineate contributions made by the glycolytic and electrophysiological systems to the overall functional heterogeneity in our β -cell populations, we divide the parametric distributions into two components: ionic and glycolytic.

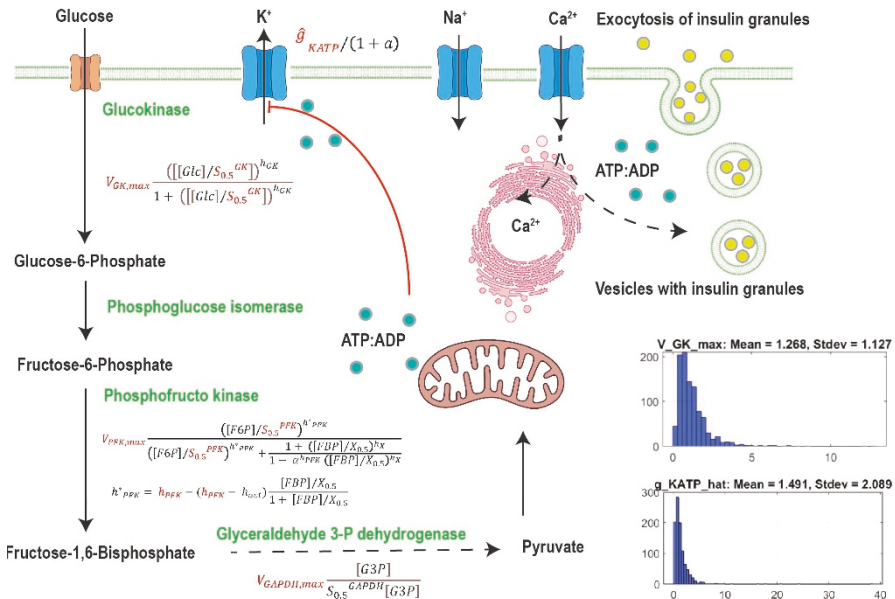


Fig. 4.3: Schematic representation of a β -cell's metabolic and electrophysiological circuit involved during the glucose-stimulated-insulin-secretion. Included in the schematic are representative formulae of the glycolytic component's enzyme rate equations and a few parameters (in red) that are changed to generate PoMs. Log-normal distributions for two of the 14 parameters are shown in the bottom right hand side of the figure.

Details of the ionic models can be found in the cited articles, but briefly electrical oscillations in the system were modeled as described by Equation 4.2. The maximal conductance (g_i) of 8 ion channels were varied based on experimental data in the

literature (references found in [34], [35], and [36]). These variations, reported via coefficients of variation (σ_p) and their sources, are summarized in Table 4.2.

The glycolysis model comprised enzymatic reactions from glucokinase to glyceraldehyde-3-phosphate. The rate of ATP generation through these steps and via downstream oxidative phosphorylation in the mitochondria is introduced in a phenomenological manner via the variable, a , which represents ATP level.

$$\frac{da}{dt} = V_{GAPDH} - k_A a \quad (4.3)$$

where V_{GAPDH} is the metabolic flux due to GAPDH and k_A is a phenomenological time constant. The ion channel conductance of K_{ATP} channel is then altered via:

$$g_{KATP} = \frac{\hat{g}_{KATP}}{1+a} \quad (4.4)$$

In our study, we varied the kinetics of the enzymatic reactions by varying the limiting rates $V_{i,max}$ of glucokinase, phosphofructokinase, and glyceraldehyde 3-P dehydrogenase. In addition we varied other kinetic parameters such as the half-activation concentrations $S_{0.5}^i$. These parameters are highlighted in red in our Figure 4.3. Variations in these glycolytic components of our model and their sources are summarized in Table 4.2. This variability was again assumed to be log-normal distributed and implemented as such for construction of our PoMs. Sources for these datasets can be found in [37], [38],[39],[40].

Since the behaviour of individual β -cells is much more diverse than those of cardiac myocytes, the constraining conditions are also less well-established. Thus, we discuss the features used for constraining the β -cell PoMs in the results, and we report sub-classes of β -cells obtained via our approach. Furthermore, we will analyze the effects of perturbations to the glycolysis and ionic components in maintaining functional heterogeneity.

4.3 Results

4.3.1 Cardiomyocyte PoM

As described in the methods, we allowed each PoM member model to equilibrate for 500s before computing the output features. The last 10 action potentials of each simulation for these models were used to extract features that were compared against the constraining criteria to generate the calibrated PoMs. Constraining criteria were:

Table 4.2: **Scaling parameters for islet β -cell PoM**Sources to construct coefficient of variation (σ_p) listed by the reference numbers

Variable	Mean	Unit	σ_p
Ionic component			
g_{KV}	1.00	nS/pF	0.37 ¹
g_{BK}	0.02	nS/pA	0.80 ¹
g_{Na}	0.40	nS/pF	0.49 ¹
g_{CaL}	0.14	nS/pF	0.34 ¹
g_{CaPQ}	0.17	nS/pF	0.40 ¹
g_{CaT}	0.05	nS/pF	0.42 ¹
g_{KATP}	0.01	nS/pF	0.89 ²
g_{HERG}	0.00	nS/pF	0.30 ³
Glycolysis component			
$V_{GK,max}$	55.60	μ M/s	0.71 ⁴
$S_{0.5}^{GK}$	8.00	mM	0.90 ⁵
$V_{PFK,max}$	556.00	μ M/s	0.03 ⁶
$S_{0.5}^{PFK}$	4.00	mM	0.09 ⁶
h_{PFK}	2.50	N/A	0.14 ⁶
$V_{GAPDH,max}$	1.39	mM/s	0.27 ⁷

¹[34], ²[35], ³[36], ⁴[37], ⁵[38], ⁶[39], ⁷[40](C₁) At all times during the simulation, $-100\text{mV} < V_m < 70\text{mV}$,(C₂) The change in cytosolic Ca^{2+} transient amplitude $< 2\%$ of the mean,(C₃) The change in cytosolic Na^+ $< 2\%$ of the mean,(C₄) The change in Ca_{SR} transient amplitude $< 2\%$ of the mean,(C₅) Peak $V_m > -20\text{mV}$,(C₆) Action potential amplitude $> 20\text{mV}$,(C₇) The standard deviation of the final 10 APD₉₀s is less than 10% of the mean,(C₈) We are able to extract every feature from the model,(C₉) The minimum diastolic potential is less than -65mV .

The full populations, showing both the accepted (orange) and discarded (grey) model configurations are shown in Figure 4.4A, together with the percent of configurations discarded based on each pairwise combination of constraints in Figure 4.4B. This figure provides a first indication of how well variability in the model behaviour is captured by applying a data-defined variation in the model inputs. A large number of configurations had to be discarded for both models, although the reasons for exclusion were different. Specifically, we retained only 55 of 500 models for our adult ventricular cardiomyocyte PoM, and 60 of 100 models for our hiPSC-CM PoM. For the adult ventricular PoM the vast majority of exclusions were made because the configuration failed either C₁ (43% of configurations) or C₉ (40% of configurations). This can also be seen in Figure 4.4A, where many configurations fail to repolarize below -65mV (C₉), whereas others reach supraphysiologic membrane potentials (either $> 70\text{mV}$ or $< -100\text{mV}$). For the hiPSC-CM model the reasons for exclusion were physiologically reachable but not observed in published hiPSC-CM phenotypes. That is, the vast majority of excluded configurations simultaneously failed criteria C₂ - C₉, each of which was chosen to address a different source of biologically

reachable instability. This can also be seen in Figure 4.4A, where most of the discarded (grey models) have attracted to a second equilibrium in membrane potential between -10mV and -20mV . This property of electrophysiologic bistability is a real biological property of cardiac myocytes [41]. It is thus a fair question to ask whether such configurations should be discarded for the hiPSC-CM PoM, as they may in fact be realistic members of most hiPSC-CM cell populations. Regardless, this initial characterization suggests that the experimentally-defined variation in hiPSC-CM input parameters results in sharp transition to gross electrophysiologic instabilities, most of which remain physiologically plausible. On the other hand, the majority of adult ventricular PoM exclusions resulted from either biologically unreachable phenotypes ($V_m > 70\text{mV}$ or $< -100\text{mV}$), or to an unstable resting potential (minimum $V_m > -65\text{mV}$).

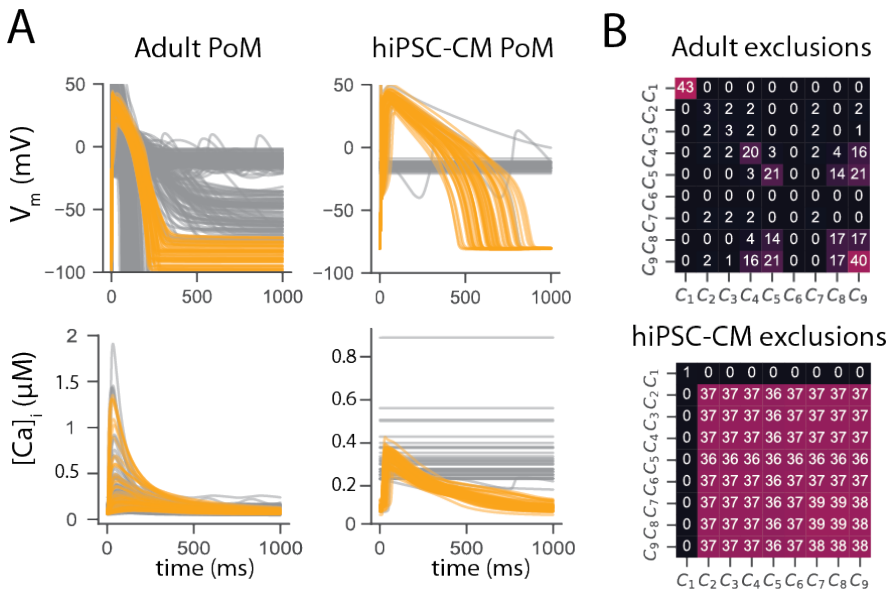


Fig. 4.4: **A** The action potential and calcium transient phenotypes from the adult CM and hiPSC-CM PoMs. Traces of cells accepted into the calibrated PoMs are in orange, while those discarded are shown in grey. **B** Tables summarizing the % of models excluded by the constraining criteria. Diagonal values show the percentage of models excluded by each criterion in isolation, whereas the off-diagonal entries show the % of configurations for which each combination of two excluding criteria were present. The meaning of each criterion, i.e. C_i , is explained in the main text.

Figure 4.5 shows the relationships between major features of the final calibrated PoMs for the two cardiac models, and provides a basis for comparing systematic differences in the phenotypic span of each PoM. The stronger relationships for the hiPSC-CM PoM between Ca^{2+} handling features and AP amplitude indicate the larger role of sarcolemmal fluxes in determining Ca^{2+} features. In contrast, the adult

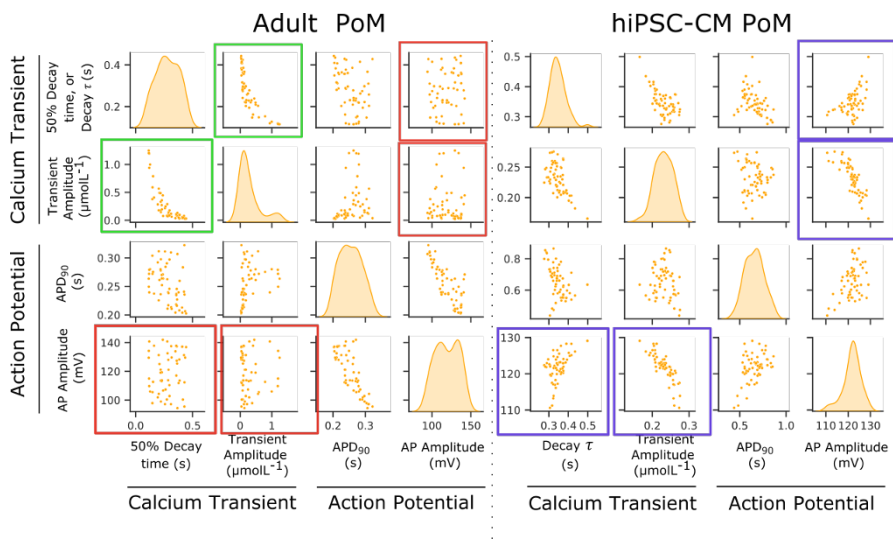
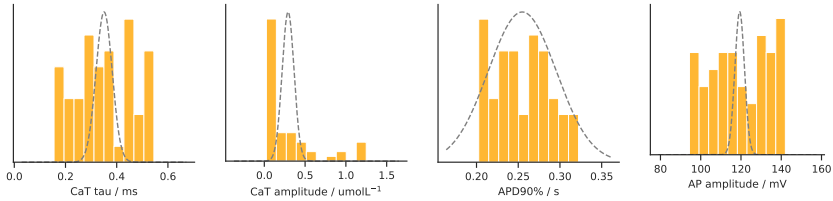


Fig. 4.5: Scatter plots of feature pairs from both PoMs. The fitted distributions are shown along the diagonals using a kernel density estimator. Noteworthy differences between the two PoMs are boxed in the red (adult) and purple (hiPSC-CM).

ventricular PoM Ca^{2+} dynamics are more internally determined, as demonstrated by stronger relationships boxed in green. These differences reflect intrinsic characteristics of the baseline hiPSC-CM and adult ventricular cardiac myocyte models. They are a well-known difference in the biological underpinnings of the two cell types and reflect the generally less “mature” Ca^{2+} handling phenotype of hiPSC-CMs relative to adult ventricular myocytes.

Finally for the cardiac PoMs, Figure 4.6 shows important differences between the two calibrated PoMs in terms of degree to which the variability in their AP and Ca^{2+} handling features reflect those reported in the literature. Specifically, it is clear that the adult ventricular PoM features (top row, orange histograms) are generally more variable than is reported experimentally (dashed lines). Only the APD_{90} feature for this PoM appears to approximate reported experimental variation. In contrast, the hiPSC-CM feature distributions (bottom row, orange histograms) are less variable than published reports of these phenotypes (dashed lines). This presents a fundamental distinction, and suggests that literature reports of variation in the underlying currents and fluxes overestimate the true physiologic variability in human adult cardiac ventricular myocytes. In contrast, the same techniques applied to hiPSC-CMs underestimate observable phenotypic variability. We explore this important observation in the discussion.

Adult ventricular cardiomyocyte PoM



hiPSC-CM PoM

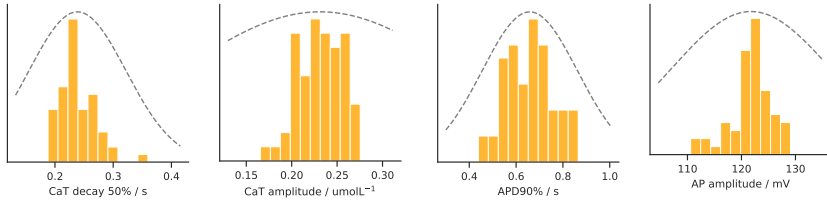


Fig. 4.6: Histograms showing the variability in the features of the PoM. The first row shows the adult ventricular cardiomyocyte PoM, and the second row shows the hiPSC-CM PoM. In each plot, the probability density function of a representative Gaussian distribution shows the variation typically found in measurements of these features in the literature. These distributions have been normalised such that they are centered on the means of each histogram.

4.3.2 Islet β -cell PoM

The individual models for the β -cell PoM were simulated to capture cell behaviour over 10 minutes - the acute phase of glucose-stimulated insulin release. The parameter variations provided in Table 4.2 were used to generate 1000 cells to assess the importance of 3 sources of heterogeneity, by varying model parameters associated with: (a) only glycolytic (enzyme) model components, (b) only ionic (ion channel and transporter) components, (c) both ionic and glycolytic components. In all three cases, each model configuration was simulated under high glucose (10 mM) and low glucose (2 mM) conditions. Thus, the total number of simulations across all 3 cases (3000 cell model configurations), at both glucose concentrations, was 6000.

Figure 4.7A shows V_m and cytosolic calcium for representative simulations at high glucose. We see cells 1 through 3 demonstrate similar features as experimentally observable sub-classes of β -cells, i.e. spiking, bursting, and plateau phenotypes. Non-firing cells such as those shown in cells 4 and 5 were also observed. As for the cardiac PoMs, in order to generate a calibrated β -cell PoM, we have to invoke and apply a set of constraining criteria to reject configurations that produce features outside the ranges of experimental observations. However, because the β -cell phenotype is the most heterogeneous of all cell types assessed here, there exists far fewer such objective constraints in the β -cell literature. However, some benchmarks are available. For example, [42] suggested two metrics of activity based on β -cell V_m

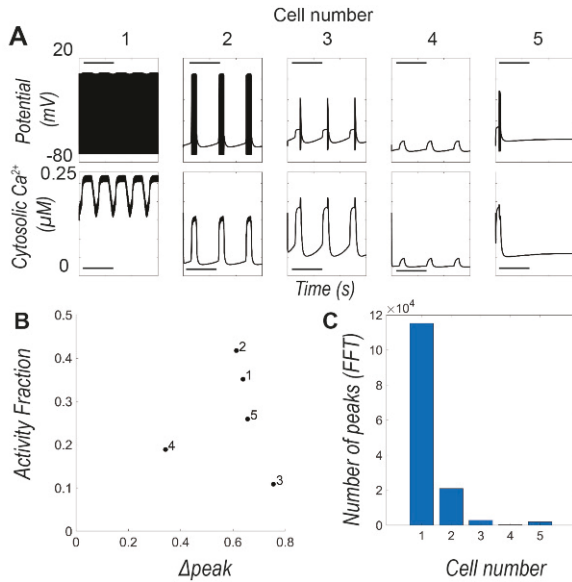


Fig. 4.7: Representative simulation outputs and categorizations. **A.** Representative simulation outputs of membrane potential and cytosolic calcium representing different sub-classes of β -cells. 1. Spiking cells 2. Bursting cells 3. Plateau cells 4 & 5. Non-firing cells. Scales on the plots represents time of 240s. **B.** Plot of activity fraction vs. Δ_{peak} for the 5 representative cells. **C.** Number of peaks in the Fast Fourier Transform (FFT) of the membrane potential traces for the 5 representative cells.

(the activity fraction and Δ_{peak}), as means of classifying phenotypic sub-classes. Activity fraction was defined as the fraction of time V_m was above an arbitrary threshold level. The definition of Δ_{peak} was set as the difference of the two major components of V_m -time probability distribution (i.e. the difference between “resting” V_m and “active” V_m). As for [42], we did not observe clear delineation of the three sub-classes, nor could we readily differentiate firing vs. non-firing β -cells via these metrics (Figure 4.7B). However, we surmised that Fast Fourier Transform (FFT) of the V_m signal may allow more clear distinction of these classes. Figure 4.7C shows the number of FFT peaks corresponded with the number of dominant harmonics in the V_m signal for each representative recording in Figure 4.7A.

Based on this analysis, we set the constraining criteria as follows. Any cell with less than 100 peaks in the V_m peaks, was considered to be quiescent and thus discarded. For cells that had more than 100 peaks in their voltage signal, FFT was performed on the voltage signal to classify them into spiking, bursting, or plateau cells. Based on our initial analyses, cells with less than 20,000 peaks in the voltage FFT were classified as plateau cells. Bursting cells were classified as those having

anywhere above 20,000 FFT peaks but less than 40,000 peaks. Finally, cells with FFT peaks greater than 40,000 were classified as spiking cells.

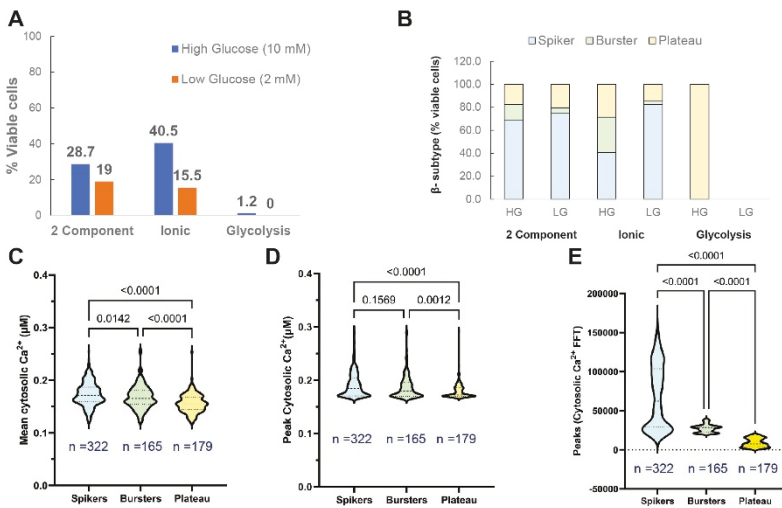


Fig. 4.8: **A.** Percentage of viable cells based on the chosen constraining conditions for six different cases (1000 runs each). **B.** Distribution of the sub-classes of β -cell from the viable candidates for each of the six cases. HG: High glucose (10 mM). LG: Low glucose (2 mM). Analyses of the cytosolic calcium traces of each of the sub-classes of β -cells in the viable population obtained with high glucose: **C.** mean values, **D.** peak values, **E.** Number of FFT peaks. Statistical differences between the groups were determined by one-way ANOVA followed by Tukey's HSD post-test.

Based on these constraining criteria, we quantified the viable cells that were not rejected for both glucose concentrations and all 3 cases of heterogeneity (glycolytic, ionic, both), as shown in Figure 4.8A. The greatest reduction in viable cells was observed for glycolytic heterogeneity only, thus highlighting the narrow metabolic parameter range functional β -cells operate under and its importance for achieving robust insulin secretion. Another interesting aspect of these data was the number of active cells at low ("resting") glucose (2 mM). This feature of basal activity is unique to human β -cells, and underlies basal insulin release at the lower blood glucose concentrations present in humans. Thus, our PoM approach was able to capture this aspect of human-specific β -cell physiology.

Further analysis of the viable candidates allowed us to assess the fraction of each of the 3 PoMs belonging to the sub-classes of β -cell phenotypes at each glucose concentration (Figure 4.8B). The lowest fraction of bursting cells was observed in the low-glucose (LG) cases when both components or only ionic components were varied. Upon altering glycolytic components alone, plateau cells comprised the only viable sub-class, thus suggesting the importance of coupling the ionic and

glycolytic elements to generate the full range of functional phenotypes observable in human β -cell populations. Mean cytosolic calcium of the viable cells within our PoM were not statistically different between spiking and bursting cells, suggestive of less pronounced basal shift of calcium signalling (Figure 4.8C). However, plateau cells exhibited a mean cytosolic calcium signature distinct from the other two classes, while peak cytosolic calcium grouped plateau and bursting phenotypes. (Figure 4.8D). Applying FFT analysis to the calcium signals also showed that the number of harmonics in the signal could distinguish the sub-classes of β -cells, thus suggesting that this may be a viable means of distinguishing functional heterogeneity in experiments, for which calcium recordings are considerably easier.

4.4 Discussion

In this manuscript, we report the construction of PoMs for three electrophysiologically active tissues that were calibrated against experimental data from the literature. PoMs have proven useful in investigation of cardiac electrophysiological variability and recent studies have furthered the methodology by explicitly incorporating experimental data into the construction of populations of models [43, 6]. In our CM PoMs, we observed that the fluctuations in the input parameters for the models allowed us to generate cells with features comparable to those observed in both primary and hiPSC-derived CMs, albeit with differing coverage of the range of function observable in experiments. In both cardiac PoMs we assumed the main source of variability is differing expression of ion transporters, and that this variation is responsible for the observable variation in their V_m and calcium cycling features. In hiPSC-CMs particularly, this variation is likely to be pronounced given their immature (“fetal-like”) phenotype and the degree to which this can be matured. Importantly, we observed that experimentally-defined variation in the input parameters of the cardiac models resulted in functional output that differed in its range for the two models. That is, for the adult CM PoM, the range of AP and calcium handling features was broader than observed experimentally, whereas it was narrower than experimental for the hiPSC-CM PoM. This is a fundamental observation about the agreement between two types of data recorded in these cell types. For the adult CM it could be that biological covariance (which we have not applied in PoM construction) among the ionic currents reduces the range of reachable AP and calcium features in real cells, or that the relative scarcity of adult human CM data means that these two classes of data are not yet fully internally consistent. In contrast, the greater experimental variability for hiPSC-CM phenotype features suggests either that experimental ionic current measurements are subjected to overly constraining inclusion criteria. Alternatively, our hiPSC-CM model formalism may somehow be constrained to be overly stable with respect to the phenotypic variation resulting from variation in the input currents. Regardless, these questions are fundamental to understanding how perturbations to either adult or hiPSC CMs should be expected to impact those tissues *in vivo*.

The islet β -cell PoMs were generated via alterations in both the parameters involved in glycolysis model components as well as the ionic conductance components. We observed that the number of harmonics in V_m of the simulated computational cells was enough to distinguish different sub-classes of β -cells observed experimentally, although we believe the proposed constraining criteria requires further validation via prospective screening of experimentally obtained data sets. Furthermore, we observed that the functional heterogeneity of the β -cells is dependent on the coupling of the metabolic and ionic components, as noted by the number of viable cells and their sub-types when only glycolytic components were varied. This, in part, explains why glycolytic bottlenecks in stem cell-derived β -cells show non-robust glucose-stimulated-insulin-secretion behaviour [44, 45]. The calibrated PoMs generated in this study were able to capture electrical oscillations at low glucose, which is a unique feature of human β -cells (compared to rodents). Thus, the methodology developed should be applicable for creating human-specific 3D models of coupled β -cell clusters with and without partner cells such as α -, δ -, ϵ - and pancreatic polypeptide cells. When coupled with experimental studies, these 3D models could be invaluable to understand the effect of heterogeneity on intact islet function, and to develop sophisticated, robust tissue-engineered platforms for therapeutics.

Here we have demonstrated the use of experimental constraints to first construct and then calibrate PoMs of three human cell types. The cardiomyocyte PoMs partially reproduced observable variation in the functional features for their respective cell types, albeit with clear systematic inaccuracies. The ability of the human β -cell PoM to recapitulate the range of function observed in experimental β -cell recordings is encouraging for applying this strategy to integrated function of β -cells in human islets. Constructing new methods for constraining these PoM approaches will require continued advancement of single cell assays.

References

1. Steffen Waldherr. Estimation methods for heterogeneous cell population models in systems biology. *Journal of The Royal Society Interface*, 15(147):20180530, October 2018.
2. Lauren L. Campbell and Kornelia Polyak. Breast tumor heterogeneity: Cancer stem cells or clonal evolution? *Cell Cycle*, 6(19):2332–2338, October 2007.
3. Zhidong Ling, Qidi Wang, Geert Stange, Peter Inf Veld, and Daniel Pipeleers. Glibenclamide treatment recruits β -cell subpopulation into elevated and sustained basal insulin synthetic activity. *Diabetes*, 55(1):78–85, January 2006.
4. Annamaria Carusi, Kevin Burrage, and Blanca Rodríguez. Bridging experiments, models and simulations: an integrative approach to validation in computational cardiac electrophysiology. *American Journal of Physiology-Heart and Circulatory Physiology*, 303(2):H144–H155, July 2012.
5. Amrita X Sarkar, David J Christini, and Eric A Sobie. Exploiting mathematical models to illuminate electrophysiological variability between individuals. *The Journal of Physiology*, 590(11):2555–2567, May 2012.
6. Oliver J Britton, Alfonso Bueno-Orovio, Karel Van Ammel, Hua Rong Lu, Rob Towart, David J Gallacher, and Blanca Rodriguez. Experimentally calibrated population of models predicts and explains intersubject variability in cardiac cellular electrophysiology. *Proceedings of the National Academy of Sciences*, 110(23), May 2013.
7. Thomas O’Hara, László Virág, András Varró, and Yoram Rudy. Simulation of the undiseased human cardiac ventricular action potential: model formulation and experimental validation. *PLoS computational biology*, 7(5):e1002061, 2011.
8. Karoline Horgmo Jæger, Andrew G Edwards, Wayne R Giles, and Aslak Tveito. A computational method for identifying an optimal combination of existing drugs to repair the action potentials of SQT1 ventricular myocytes. *PLOS Computational Biology*, 17(8):e1009233, August 2021.
9. Morten Gram Pedersen. A biophysical model of electrical activity in human β -cells. *Biophysical Journal*, 99(10):3200–3207, November 2010.
10. Pál O Westermark and Anders Lansner. A model of phosphofructokinase and glycolytic oscillations in the pancreatic β -cell. *Biophysical Journal*, 85(1):126–139, July 2003.
11. János Magyar, Norbert Iost, A Körtvély, Tamás Bányász, László Virág, P Szigligeti, András Varró, M Opincariu, J Szécsi, Julius Gyula Papp, et al. Effects of endothelin-1 on calcium and potassium currents in undiseased human ventricular myocytes. *Pflügers Archiv*, 441(1):144–149, 2000.
12. Laszlo Virag, Norbert Iost, Miklos Opincariu, Jenő Szolnoky, Janos Szecsi, Gabor Bogats, Pal Szenohradszky, Andras Varro, and Julius Gy Papp. The slow component of the delayed rectifier potassium current in undiseased human ventricular myocytes. *Cardiovascular research*, 49(4):790–797, 2001.
13. Yusaku Sakakibara, Taiji Furukawa, Donald H Singer, Hongjun Jia, Carl L Backer, Carl E Arentzen, and J Andrew Wasserstrom. Sodium current in isolated human ventricular myocytes. *American Journal of Physiology-Heart and Circulatory Physiology*, 265(4):H1301–H1309, 1993.
14. Victor A Maltsev, Hani N Sabbah, Robert SD Higgins, Norman Silverman, Michael Lesch, and Albertas I Undrovinas. Novel, ultraslow inactivating sodium current in human ventricular cardiomyocytes. *Circulation*, 98(23):2545–2552, 1998.
15. Robert HG Schwinger, Jiangnan Wang, Konrad Frank, Jochen Müller-Ehmsen, Klara Brixius, Alicia A McDonough, and Erland Erdmann. Reduced sodium pump $\alpha 1$, $\alpha 3$, and $\beta 1$ -isoform protein levels and Na⁺, K⁺-ATPase activity but unchanged Na⁺-Ca²⁺ exchanger protein levels in human heart failure. *Circulation*, 99(16):2105–2112, 1999.
16. Hans Reinecke, Roland Studer, Roland Vetter, Jürgen Holtz, and Helmut Drexler. Cardiac Na⁺/Ca²⁺ exchange activity in patients with end-stage heart failure. *Cardiovascular research*, 31(1):48–54, 1996.

17. Hans Reinecke, Roland Studer, Roland Vetter, Hanjörg Just, Jürgen Holtz, and Helmut Drexler. Role of the cardiac sarcolemmal Na^+ - Ca^{2+} exchanger in end-stage human heart failure. *Annals of the New York Academy of Sciences*, 779(1):543–545, 1996.
18. Junyi Ma, Liang Guo, Steve J Fiene, Blake D Anson, James A Thomson, Timothy J Kamp, Kyle L Kolaja, Bradley J Swanson, and Craig T January. High purity human-induced pluripotent stem cell-derived cardiomyocytes: electrophysiological properties of action potentials and ionic currents. *American Journal of Physiology-Heart and Circulatory Physiology*, 301(5):H2006–H2017, 2011.
19. Richard P Davis, Simona Casini, Cathelijne W van den Berg, Maaïke Hoekstra, Carol Ann Remme, Cheryl Dambrot, Daniela Salvatori, Dorien Ward-van Oostwaard, Arthur AM Wilde, Connie R Bezzina, et al. Cardiomyocytes derived from pluripotent stem cells recapitulate electrophysiological characteristics of an overlap syndrome of cardiac sodium channel disease. *Circulation*, 125(25):3079–3091, 2012.
20. Dongrui Ma, Heming Wei, Yongxing Zhao, Jun Lu, Guang Li, Norliza Binte Esmail Sahib, Teng Hong Tan, Keng Yean Wong, Winston Shim, Philip Wong, et al. Modeling type 3 long qt syndrome with cardiomyocytes derived from patient-specific induced pluripotent stem cells. *International journal of cardiology*, 168(6):5277–5286, 2013.
21. Sujeong Lee, Hyang-Ae Lee, Sung Woo Choi, Sung Joon Kim, and Ki-Suk Kim. Evaluation of nefazodone-induced cardiotoxicity in human induced pluripotent stem cell-derived cardiomyocytes. *Toxicology and applied pharmacology*, 296:42–53, 2016.
22. John K Gibson, Yimei Yue, Jared Bronson, Cassie Palmer, and Randy Numann. Human stem cell-derived cardiomyocytes detect drug-mediated changes in action potentials and ion currents. *Journal of pharmacological and toxicological methods*, 70(3):255–267, 2014.
23. Jussi T Koivumäki, Nikolay Naumenko, Tomi Tuomainen, Jouni Takalo, Minna Oksanen, Katja A Puttonen, Šárka Lehtonen, Johanna Kuusisto, Markku Laakso, Jari Koistinaho, et al. Structural immaturity of human ipsc-derived cardiomyocytes: in silico investigation of effects on function and disease modeling. *Frontiers in physiology*, 9:80, 2018.
24. Olaf Scheel, Stefanie Frech, Bogdan Amuzescu, Jörg Eisfeld, Kun-Han Lin, and Thomas Knott. Action potential characterization of human induced pluripotent stem cell-derived cardiomyocytes using automated patch-clamp technology. *Assay and drug development technologies*, 12(8):457–469, 2014.
25. Heming Wei, Guangqin Zhang, Suhua Qiu, Jun Lu, Jingwei Sheng, Grace Tan, Philip Wong, Shu Yin Gan, and Winston Shim. Hydrogen sulfide suppresses outward rectifier potassium currents in human pluripotent stem cell-derived cardiomyocytes. *PLoS One*, 7(11):e50641, 2012.
26. Milena Bellin, Simona Casini, Richard P Davis, Cristina D’aniello, Jessica Haas, Dorien Ward-van Oostwaard, Leon GJ Tertoolen, Christian B Jung, David A Elliott, Andrea Welling, et al. Isogenic human pluripotent stem cell pairs reveal the role of a KCNH2 mutation in long-QT syndrome. *The EMBO journal*, 32(24):3161–3175, 2013.
27. Michael Xavier Doss, Jose M Di Diego, Robert J Goodrow, Yuesheng Wu, Jonathan M Cordeiro, Vladislav V Nesterenko, Hector Barajas-Martinez, Dan Hu, Janire Urrutia, Mayurika Desai, et al. Maximum diastolic potential of human induced pluripotent stem cell-derived cardiomyocytes depends critically on IKr. *PloS one*, 7(7):e40288, 2012.
28. Mariam Jouni, Karim Si-Tayeb, Zeineb Es-Salah-Lamoureux, Xenia Latypova, Benoite Champion, Amandine Caillaud, Anais Rungoat, Flavien Charpentier, Gildas Loussouarn, Isabelle Baró, et al. Toward personalized medicine: Using cardiomyocytes differentiated from urine-derived pluripotent stem cells to recapitulate electrophysiological characteristics of type 2 long QT syndrome. *Journal of the American Heart Association*, 4(9):e002159, 2015.
29. Dongrui Ma, Heming Wei, Jun Lu, Dou Huang, Zhenfeng Liu, Li Jun Loh, Omedul Islam, Reginald Liew, Winston Shim, and Stuart A Cook. Characterization of a novel KCNQ1 mutation for type 1 long QT syndrome and assessment of the therapeutic potential of a novel IKs activator using patient-specific induced pluripotent stem cell-derived cardiomyocytes. *Stem Cell Research & Therapy*, 6(1):1–13, 2015.
30. Rosalie ME Meijer van Putten, Isabella Mengarelli, Kaomei Guan, Jan G Zegers, Antoni CG van Ginneken, Arie O Verkerk, and Ronald Wilders. Ion channelopathies in human induced

- pluripotent stem cell derived cardiomyocytes: a dynamic clamp study with virtual IK1. *Frontiers in Physiology*, 6, 2015.
31. Jonathan M Cordeiro, Vladislav V Nesterenko, Serge Sicouri, Robert J Goodrow, Jacqueline A Treat, Mayurika Desai, Yuesheng Wu, Michael Xavier Doss, Charles Antzelevitch, and José M Di Diego. Identification and characterization of a transient outward K⁺ current in human induced pluripotent stem cell-derived cardiomyocytes. *Journal of Molecular and Cellular Cardiology*, 60:36–46, 2013.
 32. XH Zhang, S Haviland, H Wei, T Šarić, A Fatima, J Hescheler, L Cleemann, and M Morad. Ca²⁺ signaling in human induced pluripotent stem cell-derived cardiomyocytes (iPS-CM) from normal and catecholaminergic polymorphic ventricular tachycardia (CPVT)-afflicted subjects. *Cell Calcium*, 54(2):57–70, 2013.
 33. Michela Riz, Matthias Braun, and Morten Gram Pedersen. Mathematical modeling of heterogeneous electrophysiological responses in human β -cells. *PLoS Computational Biology*, 10(1):e1003389, January 2014.
 34. Matthias Braun, Reshma Ramracheya, Martin Bengtsson, Quan Zhang, Jovita Karanauskaite, Chris Partridge, Paul R. Johnson, and Patrik Rorsman. Voltage-gated ion channels in human pancreatic β -cells: Electrophysiological characterization and role in insulin secretion. *Diabetes*, 57(6):1618–1628, June 2008.
 35. R Bränström, Craig A Aspinwall, S Välimäki, C-G Östensson, A Tibell, M Eckhard, H Brandhorst, BE Corkey, P-O Berggren, and O Larsson. Long-chain coa esters activate human pancreatic beta-cell katp channels: potential role in type 2 diabetes. *Diabetologia*, 47(2):277–283, 2004.
 36. Barbara Rosati, Piero Marchetti, Olivia Crociani, Marzia Lecchi, Roberto Lupi, Annarosa Arcangeli, Massimo Olivotto, and Enzo Wanke. Glucose-and arginine-induced insulin secretion by human pancreatic β -cells: the role of HERG K⁺ channels in firing and release. *The FASEB Journal*, 14(15):2601–2610, 2000.
 37. J Takeda, M Gidh-Jain, L Z Xu, P Froguel, G Velho, M Vaxillaire, D Cohen, F Shimada, H Makino, and S Nishi. Structure/function studies of human beta-cell glucokinase. enzymatic properties of a sequence polymorphism, mutations associated with diabetes, and other site-directed mutants. *J. Biol. Chem.*, 268(20):15200–15204, July 1993.
 38. M Gidh-Jain, J Takeda, L Z Xu, A J Lange, N Vionnet, M Stoffel, P Froguel, G Velho, F Sun, and D Cohen. Glucokinase mutations associated with non-insulin-dependent (type 2) diabetes mellitus have decreased enzymatic activity: implications for structure/function relationships. *Proceedings of the National Academy of Sciences*, 90(5):1932–1936, March 1993.
 39. Peter M Fernandes, James Kinkead, Iain McNae, Paul AM Michels, and Malcolm D Walkinshaw. Biochemical and transcript level differences between the three human phosphofructokinases show optimisation of each isoform for specific metabolic niches. *Biochemical Journal*, 477(22):4425–4441, November 2020.
 40. Michael J Mac Donald. Does glyceraldehyde enter pancreatic islet metabolism via both the triokinase and the glyceraldehyde phosphate dehydrogenase reactions? *Archives of Biochemistry and Biophysics*, 270(1):15–22, April 1989.
 41. Stewart Heitmann, Anton Shpak, Jamie I Vandenberg, and Adam P Hill. Arrhythmogenic effects of ultra-long and bistable cardiac action potentials. *PLoS Computational Biology*, 17(2):e1008683, 2 2021.
 42. TA Kinard, G de Vries, A Sherman, and LS Satin. Modulation of the bursting properties of single mouse pancreatic β -cells by artificial conductances. *Biophysical Journal*, 76(3):1423–1435, March 1999.
 43. Anna Muszkiewicz, Oliver J Britton, Philip Gemmell, Elisa Passini, Carlos Sánchez, Xin Zhou, Annamaria Carusi, T Alexander Quinn, Kevin Burrage, Alfonso Bueno-Orovio, and Blanca Rodriguez. Variability in cardiac electrophysiology: Using experimentally-calibrated populations of models to move beyond the single virtual physiological human paradigm. *Progress in Biophysics and Molecular Biology*, 120(1-3):115–127, January 2016.
 44. Jeffrey C Davis, Tiago C Alves, Aharon Helman, Jonathan C Chen, Jennifer H Kenty, Rebecca L Cardone, David R Liu, Richard G Kibbey, and Douglas A Melton. Glucose response by

- stem cell-derived β cells in vitro is inhibited by a bottleneck in glycolysis. *Cell Reports*, 31(6):107623, May 2020.
45. Ishan Goswami, Eleonora de Klerk, Phichitpol Carnese, Matthias Hebrok, and Kevin E Healy. Multiplexed microfluidic platform for stem-cell derived pancreatic islet β cells. *Lab on a Chip*, 2022.

Open Access This chapter is licensed under the terms of the Creative Commons Attribution 4.0 International License (<http://creativecommons.org/licenses/by/4.0/>), which permits use, sharing, adaptation, distribution and reproduction in any medium or format, as long as you give appropriate credit to the original author(s) and the source, provide a link to the Creative Commons license and indicate if changes were made.

The images or other third party material in this chapter are included in the chapter's Creative Commons license, unless indicated otherwise in a credit line to the material. If material is not included in the chapter's Creative Commons license and your intended use is not permitted by statutory regulation or exceeds the permitted use, you will need to obtain permission directly from the copyright holder.





Chapter 5

Realizing Synaptic Signal Transmission During Astrocyte-Neuron Interactions within the EMI Framework

Julia Gorman, Konstantin Holzhausen, Joyce Reimer, and Jørgen Riseth

Abstract The tripartite synapse or “neural threesome” refers to the interplay in the synapse between neighbouring neurons, the synaptic cleft, and the surrounding glial cells. Despite extensive research, the effects of glial cells, such as astrocytes, on signal transduction between neurons are not fully understood. The Kirchhoff-Nernst-Planck (KNP) and Extracellular-Membrane-Intracellular (EMI) models constitute a promising framework for modeling these kinds of systems. However, they lack the neurotransmitter-related mechanisms that are necessary to bridge signal transduction across the synaptic cleft. Here, we propose an extension to the KNP-EMI model by a spatio-temporal diffusion-based description of the most prominent neurotransmitter, glutamate, that allows for investigation of the contribution of astrocytes to the functionality of the synapse. We validate our model by showing that the presence of an astrocyte in the domain affects the glutamate flux across the postsynaptic terminal, as observed physiologically. The proposed extension offers a sufficiently simple way of integrating synaptic glutamate dynamics into the KNP-EMI framework. It introduces the relevant interactions between electrical activity and diffusion processes at the tripartite synapse that are necessary to assess how astrocytes might contribute to the functionality of the synapse. This work has implications for future studies involving glial mechanisms and other charged species within the KNP-EMI framework.

Julia Gorman

Department of Neurosciences, University of California, San Diego, USA

Konstantin Holzhausen

Department of Physics, University of Oslo, NO

Joyce Reimer

Division of Biomedical Engineering, University of Saskatchewan, CA

Jørgen Riseth (corresponding author)

Department of Numerical Analysis and Scientific Computing, Simula Research Laboratory, NO

e-mail: jorgenr@simula.no

5.1 Introduction

Circuits in the brain are composed of complex connections of both neurons and glia. Neurons communicate via patterns of electrical signals that are propagated by molecules and ions. These signals, called action potentials, communicate information that gives rise to cognitive function, behaviors, and movements. Action potentials travel from neuron to neuron across small gaps called synapses. The neuron sending the signal, the presynaptic neuron, releases specific molecules called neurotransmitters to the receiving neuron, or the postsynaptic neuron. However, neurons are not the only cells that are found in the synapse. A type of glial cell called an astrocyte envelopes the synapse and alters information transmission by modulating the neurotransmitters as they diffuse across the synapse [1]. Thus, together, the neurons, the synapse, and the astrocyte form a “neural threesome” [2], or tripartite synapse. The role of this astrocyte mediated modulation in electrical and chemical interplay is not well understood.

One of the ways astrocytes are thought to affect synaptic transmission is through reuptake of the neurotransmitter glutamate. Once an electrical signal reaches the end of the presynaptic neuron, prepackaged vesicles release glutamate into the synaptic cleft. After release, glutamate diffuses across the synapse where it binds AMPA receptors on the postsynaptic neuron, resulting in a net inward sodium (Na^+) current through the ligand-gated AMPA receptor ion channels. As a result, the intracellular potential starts to increase which triggers the opening of nearby voltage-gated Na^+ channels. This channel opening allows for a larger Na^+ influx, bringing the postsynaptic neuron closer to its threshold for depolarization. If the signal is strong enough, subsequent ion dynamics across the postsynaptic membranes result in the onset of a new action potential and signal propagation continues.

As glutamate diffuses across the synapse, astrocytes take up a percentage of the glutamate ions through high-affinity glutamate transporters [3, 4]. This mechanism is suggested to be a way of reducing cellular toxicity, as too much glutamate in the synapse can have excitotoxic effects [5]. Recently, it has been found that astrocytes also release glutamate to neurons in response to extracellular glutamate cues [6]. Because of this dual mechanism of glutamate uptake and release, astrocytes act as a buffer to balance excitatory and inhibitory neuronal activity.

Here, we propose a simple mechanistic model of glutamate in the tripartite synapse that allows for the assessment of these questions within the Kirchhoff-Nernst-Planck (KNP) - Extracellular-Membrane-Intracellular (EMI) modeling framework. The KNP-EMI model is a mechanistic mathematical model for excitable tissue in spatiotemporal resolution. It is stated in the form of a set of coupled partial differential equations, and includes interactions between ionic transmembrane currents and electric potentials [7, 8, 9]. In [7], Ellingsrud *et al.* show that their KNP-EMI model accurately describes depolarization along excitable membranes. Thus, it constitutes a truly spatio-temporal model of signal transduction along a cell, for example, along an axon or a dendrite of a neuron. However, the model in its current form does not account for neurotransmitters in the extracellular space, nor for neurotransmitter-

related mechanisms and interactions. For this reason, the KNP-EMI model is not able to capture the regulation of signal transduction at the synapse.

We propose an extension by introducing glutamate to the model. In order to bridge the synaptic gap, we identify three relevant biophysical mechanisms: glutamate release into the cleft by exocytosis from the presynaptic neuron, diffusion in the extracellular space, and binding to postsynaptic AMPA receptors. All three of these processes are considered in our implementation. In addition to this, we assume that glutamate uptake is the fundamental interaction of the astrocyte at the synapse whereby astrocytes regulate signal transmission. Therefore, our proposed glutamate diffusion model describes the properties of signal transduction unique to the synapse; in particular, how astrocytes affect the glutamate gradient and how a changing glutamate gradient affects signal propagation. Our extension to the KNP-EMI model features a simplified yet qualitatively complete description of signal transmission across neurons. The extended model will allow for a comprehensive investigation of the astrocyte's role in signal propagation across neurons in a way that takes spatial effects, such as explicit geometries and local concentrations, into account.

The EMI model constitutes a general framework for modeling excitable tissue ranging from cardiac cells to neural systems [10]. Besides its broad range of application, it allows for the incorporation of explicit morphologies within the system of interest. In combination with the KNP framework, the KNP-EMI model allows for the representation of a complicated geometry and detailed electrochemical profiles [8]. In order to leverage its power, we design our glutamate model under consideration of its integrability into the KNP-EMI model. Although its formulation is independent of the respective morphology, our implementation assumes a simplistic geometry in order to show its functionality as a proof of concept.

Our paper is structured as follows. First, we familiarize the reader with the geometry of the problem conceptually and derive the glutamate model. Subsequently, we demonstrate a way to estimate the model parameters based on literature values, restricting our model to hippocampal synapses. After providing implementation details, we validate the glutamate model by showing that it behaves as intended. Finally, we discuss the implications of our model within the context of the KNP-EMI framework.

5.2 Methods

The glutamate model consists of two parts. The first part describes the transport of glutamate across the synaptic cleft by diffusion, whereas the second part describes how AMPA receptors react in response to glutamate to trigger a Na^+ current across the postsynaptic terminal. Here, we describe the computational domain and the governing equations for the glutamate model. We then describe the parameters that are used within the model, and finally, the numerical methods used in our simulations.

5.2.1 Representation of the Computational Domain

The tripartite synapse features a variety of membranes that behave differently. The characteristic behavior of each membrane is determined by the density and type of functional components it exhibits, e.g. channels, pumps, and receptors. Figure 5.1 shows a schematic of our envisioned computational domain for the full KNP-EMI model. It resembles a simplified and abstracted two-dimensional realization of a tripartite synapse setup. The domain is divided into two distinct subdomains: the

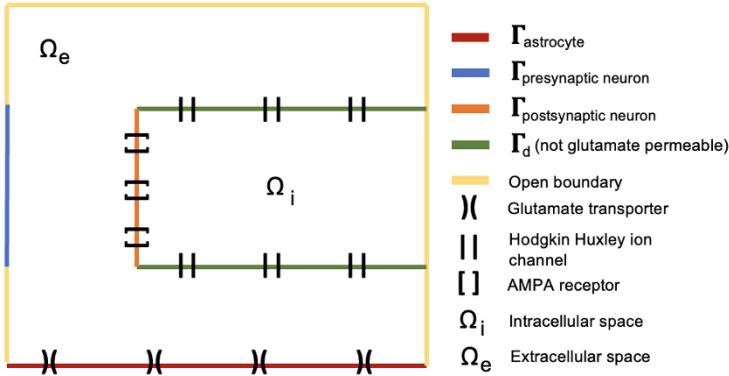


Fig. 5.1: Representation of the computational domain in our glutamate KNP-EMI model. Synthesis of computational domains, channel dynamics, and boundary conditions.

extracellular space, Ω_{e} , and the intracellular space, Ω_{i} . Ω_{i} represents the interior of the postsynaptic neuron's dendrite. The interface boundary separating Ω_{e} from Ω_{i} consists of the postsynaptic terminal, Γ_{post} , and extrasynaptic membrane of the dendrite, Γ_{d} . We assume that Γ_{d} is impermeable to glutamate. In contrast, Γ_{post} is a region with an affinity for glutamate due to the presence of AMPA receptors, which are only located on the part of the postsynaptic membrane that faces the synapse [11]. The exterior boundary consists of three biophysically distinct types. Γ_{pre} denotes the membrane between the presynaptic neuron and the synapse. Γ_{a} represents the membrane on the astrocyte, which also has an affinity for glutamate due to the presence of glutamate transporters that clear it from the synapse [4]. The remaining part of the exterior boundary is open for glutamate to pass, since the neurotransmitter freely diffuses through the extracellular space out of the synaptic region. We note that because this report only covers the glutamate model, our computational domain is for now restricted to the extracellular space, Ω_{e} .

5.2.2 Mathematical Modeling of Glutamate Dynamics

The glutamate transport is modelled using a pure diffusion equation: find the glutamate concentration $g = g(x, t)$ such that

$$\partial_t g = D_e \Delta g \quad \text{on} \quad \Omega_e \times [0, T] \quad . \quad (5.1)$$

Here, D_e is the diffusion coefficient for glutamate within the extracellular space. The glutamate release from the presynaptic terminal and absorption of glutamate on the various cell membranes are modelled using the following combination of von Neumann and Robin boundary conditions:

$$-D_e \nabla g \cdot \mathbf{n}_{\Gamma_d} = 0 \quad \text{on} \quad \Gamma_d \times [0, T] \quad (5.2)$$

$$-D_e \nabla g \cdot \mathbf{n}_{\Gamma_a} = k_{\text{uptake}} g|_{\Gamma_a} \quad \text{on} \quad \Gamma_a \times [0, T] \quad (5.3)$$

$$-D_e \nabla g \cdot \mathbf{n}_{\Gamma_{\text{post}}} = k_{\text{bind}} g|_{\Gamma_{\text{post}}} \quad \text{on} \quad \Gamma_{\text{post}} \times [0, T] \quad (5.4)$$

$$-D_e \nabla g \cdot \mathbf{n}_{\Gamma_{\text{pre}}} = -\sum_i v_v^i \delta(t - t_i) \quad \text{on} \quad \Gamma_{\text{pre}} \times [0, T]. \quad (5.5)$$

Note that here, \mathbf{n}_k denotes the outward pointing normal vectors of the respective boundary surfaces. As a consequence, the left hand sides denote the outward fluxes of glutamate through them. We model glutamate binding to the AMPA receptors as well as glutamate uptake at the astrocyte's membrane by first order reaction kinetics. Thus, k_{bind} specifies the affinity of the AMPA receptor towards glutamate and k_{uptake} the absorption rate. The reflecting boundary condition at Γ_d in Equation (5.2) realizes the impermeability of glutamate through the extrasynaptic membranes of the dendrite. Equation (5.5) describes the source of glutamate in our model, which is vesicular release due to exocytosis. In accordance with Clements *et al.* [12] and Jonas *et al.* [13], we model an instantaneous release of vesicles at release times t_i . v_v^i denotes the vesicular spatial profile defined in Equation (5.9). On the remaining open boundaries, we assume homogeneous Dirichlet boundary conditions

$$g|_{\Gamma_{\text{open}}} = 0 \quad . \quad (5.6)$$

This choice is made for simplicity, and future work will benefit from more realistic modelling of free diffusion across the open boundaries. Since glutamate is supposed to be cleared from the synaptic cleft after exocytosis, we assume an initial equilibrium of $g(x, t = 0) = 0$.

5.2.3 Modeling AMPA Gating Dynamics

We model the dynamics of the AMPA receptors on the postsynaptic terminal using a model proposed by Tewari and Majurmdar [14]. The ODE model describing the AMPA gating dynamics reads

$$\frac{d}{dt} m_{\text{AMPA}} = \alpha_{\text{AMPA}} g|_{\Gamma_{\text{post}}} (1 - m_{\text{AMPA}}) - \beta_{\text{AMPA}} m_{\text{AMPA}} \quad . \quad (5.7)$$

Here, the glutamate concentration, g , couples linearly to the opening rate of the AMPA receptor, α_{AMPA} . The ODE model governs the dynamics of the gating variable, m_{AMPA} , point-wise along the boundary Γ_{post} , and depends on the local glutamate concentration, $g|_{\Gamma_{\text{post}}}$. We intend to initialize the system in its equilibrium state. The initial state $g(x, t = 0) = 0$ corresponds to the equilibrium state of the glutamate model. For $g = 0$, we get $m_{\text{AMPA}}^* = 0$ as the stationary state of the gating variable m_{AMPA}^* at $t = 0$. Therefore, we choose $m_{\text{AMPA}}(t = 0) = m_{\text{AMPA}}^* = 0$.

The gating variable, m_{AMPA} , controls an AMPA-specific Na^+ current, I_{AMPA} , through the postsynaptic terminal. This current is given by

$$I_{\text{AMPA}} = g_{\text{AMPA}} m_{\text{AMPA}} (V_{\text{post}} - V_{\text{AMPA}}) \quad \text{on} \quad \Gamma_{\text{post}} \quad (5.8)$$

[15, 14], with V_{post} being the local membrane potential at the postsynaptic neuron and V_{AMPA} referring to the reversal potential. In the KNP-EMI model, V_{AMPA} is associated with the Na^+ -specific Nernst potential.

5.2.4 Estimation of Model Parameters

All parameters for the AMPA receptors were chosen in the same way as the original model by Tewari *et al.* [14]. Following Clements *et al.* and Tewari *et al.*, we assume vesicles with a diameter $d_{\text{Ves}} = 40 \text{ nm}$, containing glutamate at concentrations of $c_{\text{Ves}}^{\text{Gl}} = 60 \text{ mM}$. In addition, we assume a homogeneous glutamate surface density $\zeta_{\text{Ves}}^{\text{Gl}}$ across the vesicle's cross section on the presynaptic terminal. We may now define a vesicular profile at Γ_{pre} , v_v^i , as

$$v_v^i(y) = \begin{cases} \zeta_{\text{Ves}}^{\text{Gl}} & \forall |y - y_{\text{Ves}}| \leq d_{\text{Ves}} \\ 0 & \text{else,} \end{cases} \quad (5.9)$$

where y_{Ves} denotes the center position of the vesicle on the membrane and y denotes the coordinate parameterizing the one-dimensional boundary surface. We assume that the arrival of the action potential at the presynaptic bouton at any time $t = t_{\text{rel}}$ results in the release of one vesicle. On release, the total mass of glutamate contained within one vesicle exocytosed across the membrane Γ_{pre} within the period $[t_{\text{rel}} - \epsilon, t_{\text{rel}} + \epsilon]$, $\epsilon > 0$ can be written as

$$\begin{aligned} M &= \int_{t_{\text{rel}} - \epsilon}^{t_{\text{rel}} + \epsilon} dt \int_{\Gamma_{\text{pre}}} D_e \nabla g \cdot \mathbf{n}_{\Gamma_{\text{pre}}} dS \\ &= \int_{y_{\text{Ves}} - d_{\text{Ves}}/2}^{y_{\text{Ves}} + d_{\text{Ves}}/2} \zeta_{\text{Ves}}^{\text{Gl}} dy = \zeta_{\text{Ves}}^{\text{Gl}} d_{\text{Ves}} \quad . \end{aligned}$$

On average, this total mass is $M_{\text{Ves}} = V_{\text{Ves}} c_{\text{Ves}}^{\text{Gl}} = \frac{4}{3} \pi R_{\text{Ves}}^3 c_{\text{Ves}}^{\text{Gl}}$, assuming spherical vesicles with radius $R_{\text{Ves}} = d_{\text{Ves}}/2$. This yields a mean surface density of

$$\zeta_{\text{Ves}}^{\text{Gl}} = \frac{\pi}{6} c_{\text{Ves}}^{\text{Gl}} d_{\text{Ves}}^2 \quad . \quad (5.10)$$

Released glutamate diffuses throughout the synaptic cleft. In accordance with [13], we choose a diffusion coefficient of $D_e = 3 \cdot 10^5 \text{ nm}^2 \text{ ms}^{-1}$ for glutamate in extracellular space. In common reaction kinetic models of synaptic glutamate, the total clearance rate amounts to $k_c = 10 \text{ ms}^{-1}$ [15, p.4]. 4/5 of synaptic glutamate is cleared by glial uptake, which leaves only 1/5 being removed by processes on the postsynaptic terminal including uptake and binding to receptors [16]. Furthermore, glutamate gets cleared passively by diffusing out of the cleft. We use these proportions to estimate the surface uptake and binding rate densities $k_{\text{uptake}}, k_{\text{bind}}$. Since $D_e \gg k_c$, diffusion is the dominant process governing the synaptic glutamate distributions. Thus, we assume $D_e \rightarrow \infty$ locally when focusing on the reaction kinetics on the membranes. In this limit, the system is well-mixed and glutamate is homogeneously distributed such that $g \equiv g_c \in \mathbb{R}$. It behaves like a single-compartment model, which allows us to directly compare the respective flux terms. In particular, we require that all of the clearing fluxes add up to k_c , by

$$\frac{1}{5} k_c g_c = g_c \int_{\Gamma_{\text{post}}} k_{\text{bind}} dS \quad (5.11)$$

$$\frac{4}{5} k_c g_c = g_c \int_{\Gamma_a} k_{\text{uptake}} dS \quad . \quad (5.12)$$

We assume that the membrane properties do not change locally, therefore, we assume homogeneous surface rate densities. Thus, we have simple expressions for both surface rate functions,

$$k_{\text{bind}} = \frac{1}{5} \frac{k_c}{h_t} \quad (5.13)$$

$$k_{\text{uptake}} = \frac{4}{5} \frac{k_c}{w_s} \quad . \quad (5.14)$$

Here, w_s denotes the width of the synaptic cleft and h_t describes the full height of the synaptic terminals. Table 5.1 summarizes all parameters and their values associated with our glutamate model.

5.2.5 Numerical Methods

In our validation studies, we solve the glutamate diffusion model numerically using the finite element method with piecewise continuous linear elements for spatial discretization and an implicit Euler scheme for temporal integration.

Table 5.1: Parameters and their values relevant for the glutamate model

Symbol	Value	Unit	Description
D_e	$3 \cdot 10^5$	$\text{nm}^2 \text{ms}^{-1}$	Diffusion coefficient in the extracellular space
k_{bind}	$5 \cdot 10^{-3}$	$\text{nm}^{-1} \text{ms}^{-1}$	AMPA specific glutamate binding surface rate density
k_{uptake}	$4 \cdot 10^{-1}$	$\text{nm}^{-1} \text{ms}^{-1}$	Glutamate uptake surface rate density of the astrocyte
$\zeta_{\text{Ves}}^{\text{Gl}}$	$5 \cdot 10^5$	mM nm^2	Glutamate release surface density
d_V	40	nm	Mean diameter of a vesicle
w_s	20^a	nm	Width of the synaptic cleft
h_t	400^a	nm	Full height of the synaptic terminals

^a Values according to Clements *et al.* [12].

Let V_h denote the set of continuous piecewise linear functions restricted to a discrete triangulation of Ω_e , such that $v \in V_h$ vanish at the open boundaries Γ_{open} . Then, the discrete variational form of the glutamate diffusion model at time $t = n\Delta t$, where $n = 0, 1, \dots$, and Δt is the time step, reads: find $g \in V_h$ such that

$$\begin{aligned} \int_{\Omega_e} \frac{1}{\Delta t} g v + \nabla g \cdot \nabla v \, dx + \int_{\Gamma_a} k_{\text{uptake}} g|_{\Gamma_a} v \, ds + \int_{\Gamma_{\text{post}}} k_{\text{bind}} g|_{\Gamma_{\text{post}}} v \, ds \\ = \int_{\Omega_e} \frac{1}{\Delta t} g^0 v \, dx + \sum_i \int_{\Gamma_{\text{pre}}} v_v^i \delta^*(t - t_i) v \, ds \quad \forall v \in V_h \quad . \end{aligned} \quad (5.15)$$

Here, g^0 refers to the solution at the previous timestep $t_0 = (n-1)\Delta t$, and δ^* refers to a distribution that, similar to the dirac delta in Equation (5.5), has the property that the glutamate released from each vesicle coincides with its total mass when integrated in time. This distribution may, for example, be a box function which evaluates to $1/\delta_t$ over some interval $[t, t + \delta_t]$, or a Gaussian function parameterized by the length scale δ_t .

On the other hand, we implement the AMPA model (5.7) using an explicit Euler integration scheme:

$$m_{\text{AMPA}} = m_{\text{AMPA}}^0 + \Delta t \left(\alpha_{\text{AMPA}} g^0|_{\Gamma_{\text{post}}} \left(1 - m_{\text{AMPA}}^0 \right) - \beta_{\text{AMPA}} m_{\text{AMPA}}^0 \right) \quad . \quad (5.16)$$

The model is implemented and solved using FEniCS [17].

5.3 Results

In the following section, we present the results of our validation study regarding our glutamate model. Figure 5.2 illustrates our experimental setup. It shows the glutamate concentrations at three different time points of our numerical solution in the synapse. We start the simulation with the release of a vesicle from Γ_{pre} at $t = 0.01\mu\text{s}$. In our study, we compare two cases: glutamate release located close to

the site of the astrocyte at the bottom of the presynaptic terminal, and release at the opposite site of the terminal, far from the astrocyte. Figure 5.2 displays both cases.

At $t = 0.01 \mu\text{s}$, upon release of the glutamate into the synaptic cleft, Figure 5.2 shows highly localized concentrations of glutamate near the regions of release at the presynaptic terminal, indicated by the red regions of high contrast. After $0.1 \mu\text{s}$, the pronounced glutamate concentration profiles have become smoother and the distribution has significantly broadened. At $t = 0.5 \mu\text{s}$, the glutamate distribution has become diffusive, and it is clearly visible that glutamate is cleared from the synaptic cleft. It should be noted that the depiction in Figure 5.2 is compressed in height. In fact, the synapse is higher than it is wide by a factor of 20. Note that the apparent increased transport along the horizontal axis is an artifact of this compressed domain. In contrast to our expectations, there seems to be no apparent difference between

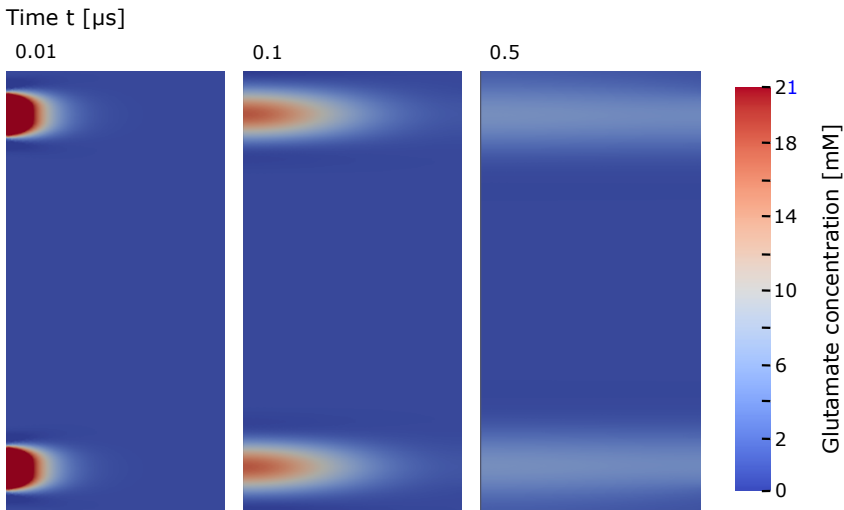


Fig. 5.2: Glutamate dynamics in the synaptic cleft. Glutamate distribution in the synaptic cleft is shown at three different time points. Vesicles are released at $t = 0.01 \mu\text{s}$ on the presynaptic terminal (left boundary) either near the astrocyte's location (bottom) or far away from it near the open boundary (top). Glutamate bridges the postsynaptic terminal (to the right) by diffusion. For the sake of visualization, the synapse is compressed in height.

the two distributions suggesting that the astrocyte's influence on the clearance of glutamate might be negligible compared to diffusion.

Figure 5.3 summarizes the glutamate fluxes through the membranes of interest and the resulting AMPA-related Na^+ current in a quasi-static approximation of the postsynaptic membrane potential. Figure 5.3A shows the glutamate flux J_{Astro} across the astrocyte's membrane Γ_a as a function of time. After the release near the astrocyte

(golden curve), the net flux of glutamate across the membrane increases rapidly and starts to decrease again after $0.25\mu\text{s}$ as the glutamate gets cleared from the synaptic cleft. In contrast to that, we do not measure a significant glutamate uptake through the astrocyte at all if the vesicle is released at the opposite end (teal curve). We note that shortly after the release, J_{Astro} becomes negative. According to the boundary condition in Equation (5.3), this corresponds to non-physical negative glutamate concentrations at the boundary. Since $g \geq 0$, this observation indicates numerical instabilities that may be attributed to the Gibbs phenomenon. Despite that, the concentration and J_{Astro} quickly stabilize and exhibit the expected behaviour.

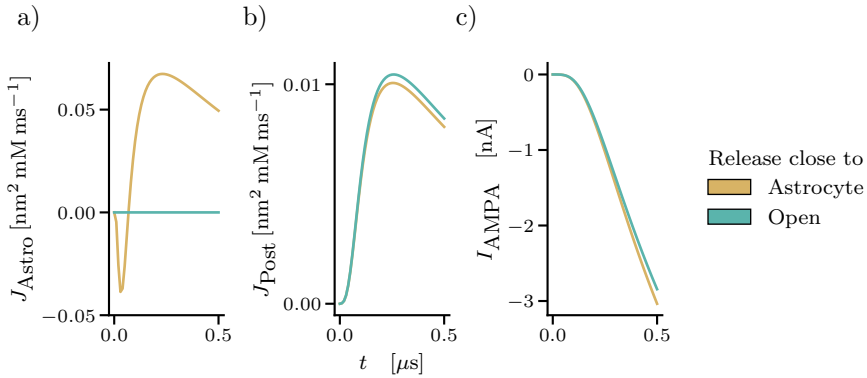


Fig. 5.3: Flux dynamics vs. time in the glutamate model. **a)**: Total glutamate uptake by the astrocyte. **b)**: Total glutamate flux through the postsynaptic terminal, J_{Post} , due to binding to the AMPA receptor. **c)**: Total Na^+ current I_{AMPA} as a result of AMPA activation caused by the arriving glutamate in case of a quasi-static membrane potential at $V_{\text{post}} = -65\text{mV}$.

Figure 5.3B depicts the glutamate flux through the postsynaptic membrane, J_{Post} , in time. J_{Post} has important implications for the excitation of the postsynaptic neuron because it indirectly reflects the activation of the AMPA receptors that control Na^+ channels on the membrane. The profile of glutamate uptake through the postsynaptic terminal is qualitatively similar to that of the astrocyte. On the falling branch of the curve however, we see that if the astrocyte is locally present, less glutamate reaches the postsynaptic terminal as a result of active clearance by the astrocyte. This validates our model with respect to the literature [3, 5, 4].

Figure 5.3C shows the magnitude of the AMPA-regulated Na^+ current across the postsynaptic terminal in time. Thus, it reflects the total activity of the AMPA receptors on Γ_{post} as glutamate approaches that membrane and binds to the receptors. I_{AMPA} is calculated from the AMPA gating variable, m_{AMPA} , using Equation (5.8). We assume that in the simulated period, the postsynaptic membrane potential has not deviated too far from its resting potential despite the finite AMPA current. With this quasi-stationary approximation, we justify $V_{\text{Post}} \approx -65\text{mV}$, the neuron resting

potential, and are able to give a coarse estimate of I_{AMPA} without having to couple our model. Similar to Tewari *et al.* [14], we choose $g_{\text{AMPA}} = 0.35\text{nS}$ and $V_{\text{AMPA}} = 0\text{mV}$. Negative signs indicate a net Na^+ current out of the dendrite instantiating depolarization across the membrane. As glutamate reaches the postsynaptic neuron, we see a growing increase in the AMPA-specific Na^+ current, as expected. In contrast to J_{Post} , I_{AMPA} does not saturate within the simulated time window. We note that while less glutamate reaches the postsynaptic neuron in the region of influence of the astrocyte (Figure 5.3B), unexpectedly, the resulting AMPA current I_{AMPA} of this region appears to be more pronounced.

5.4 Discussion

We developed a diffusion-based, spatio-temporal model of the neurotransmitter glutamate in glutamatergic hippocampal synapses. We carried out validation studies demonstrating that our model reproduces the astrocyte's role in glutamate uptake in the tripartite synapse. In addition, we observed that astrocytic glutamate uptake translates into a decrease in glutamate flux across the postsynaptic terminal, showing that astrocytes temper the excitatory signal that is transmitted to postsynaptic neurons. This is a widely recognized key role of astrocytes [3, 5, 4]. We also saw in our model that the binding of glutamate to AMPA receptors in the postsynaptic neuron results in a net AMPA-specific Na^+ current I_{AMPA} , initiating depolarization in the postsynaptic neuron. Thus, our model successfully translates synaptic chemical cues into an electrical signal in the postsynaptic neuron. Unexpectedly, we observed that the total postsynaptic glutamate flux, J_{Post} , inversely affects the strength of the AMPA-specific Na^+ current. This effect could be explained by the astrocyte causing a narrower glutamate distribution, resulting in a locally restricted but higher AMPA activation. As a consequence, the total Na^+ current might be stronger. The glutamate profiles in Figure 5.2, however, indicate otherwise. Moreover, our quasi-static approximation of I_{AMPA} does not resemble the actual Na^+ current dynamics accurately. Using the correct dynamic potentials, e.g. by coupling our glutamate model to the KNP-EMI model, might yield different results. Finally, we observed characteristics in our simulation results that indicate issues of numerical stability near the astrocyte during release. Similar instabilities might be causing the discrepancy in I_{AMPA} that we can not explain in the scope of our model. Thus, the next logical step would be to study the stability and convergence of our methods comprehensively.

Furthermore, we observed a significant difference in postsynaptic activity with and without the astrocyte. However, the effect is not as pronounced as we would have expected. Conversely, it appears rather minute. The reason for that might lie in our choice of the astrocyte's location in terms of distance from the neurons. In our model, we have chosen a distance of 50 nm, which is 2.5-fold larger than the width of the synaptic cleft. As a next step, we suggest situating the astrocyte closer to the neurons. Lastly, the astrocyte's role of clearing the synaptic cleft is expected to be most significant when it is saturated with glutamate, for example,

in bursting neurons. In this case, excessive concentrations of neurotransmitters can have a neurotoxic effect. In our study, we only considered single-vesicle release, but our model accounts for an arbitrary amount. Consequently, with longer simulated time windows, multi-vesicular release studies resembling spike trains of arbitrary frequency are an obvious and promising connecting factor for future work.

Other computational studies measuring glutamate flux in a synapse could not be found in the literature. However, some physiological studies may be used to contextualize our results. Although glutamate flux across an astrocyte is not directly measured *in vitro*, it can be carried out indirectly by measuring the changing glutamate concentration of a medium containing astrocyte cultures. In this regard, the studies by Farinelli and Nicklas [18] and Fonseca *et al.* [19] show similar glutamate clearance dynamics as our results (e.g., Figures 5.2 and 5.3, respectively). These astrocytic clearance dynamics are measured over a much longer time period. However, the observed pattern may be extended to our study in that there is an initial fast rate of glutamate clearance, followed by a plateau stage during which the rate of clearance slows as the relative glutamate concentration approaches 0 mM.

A clear extension to our study would be utilizing the model in tandem with the KNP-EMI model. Our model design integrates well into EMI or KNP-EMI frameworks by adding the AMPA-specific contribution to the Na^+ current, I_{AMPA} . In the EMI and KNP-EMI frameworks (e.g. [8]), the choice of the functional form of I_{ion} is subject to modelling, usually in form of a solution to a Hodgkin-Huxley type ODE system [20]. When integrating our model into the KNP-EMI framework, we suggest setting $I_{\text{ion}} = I_{\text{AMPA}}$ on the postsynaptic terminal (Γ_{post} in Figure 5.1) and Hodgkin-Huxley based models on the remaining postsynaptic membranes (Γ_{d}).

Considering further astrocyte-related mechanisms, such as the dual function of glutamate uptake and release [6], the KNP-EMI model is expected to be especially well-suited for modelling glutamate uptake. As a first step into modeling neurotransmitters within the KNP-EMI framework, we designed our model with simplicity in mind. For this reason, our model only features what we identified as the most relevant processes for signal transmission, excluding presynaptic glutamate re-uptake and astrocytic glutamate release. These mechanisms should, however, be considered in a refined model, because they are supposedly relevant for realizing glutamate buffers in the synapse. Additionally, the dual function mechanism is controlled in part by intracellular pH levels [21], which may be well handled by the ionic concentration and diffusion components of the KNP-EMI model.

In summary, we successfully developed a glutamate extension to the KNP-EMI model in the tripartite synapse. Our model exhibits all the relevant mechanisms necessary for signal transmission between neurons across the synaptic cleft. In our model, the astrocyte modulates the signaling molecule concentrations as expected. Their effect could be more pronounced, but we expect that our choice regarding the astrocyte's distance from the synapse had a significant influence on this outcome. Additionally, the resulting Na^+ current behaves contrarily to expectations in response to the astrocyte's influence. Future work on our model should address our concerns regarding this particular parameter choice and the numerical stability of the model.

References

1. Eric A Bushong, Maryann E Martone, Ying Z Jones, and Mark H Ellisman. Protoplasmic astrocytes in cal stratum radiatum occupy separate anatomical domains. *Journal of Neuroscience*, 22(1):183–192, 2002.
2. Kerri Smith. Neuroscience: Settling the great glia debate. *Nature (London)*, 468(7321):160–162, 2010.
3. Arthur M Butt. Atp: a ubiquitous gliotransmitter integrating neuron–glial networks. In *Seminars in cell & developmental biology*, volume 22, pages 205–213. Elsevier, 2011.
4. Christine R Rose, Lisa Felix, Andre Zeug, Dirk Dietrich, Andreas Reiner, and Christian Henneberger. Astroglial glutamate signaling and uptake in the hippocampus. *Frontiers in Molecular Neuroscience*, 10:451, 2018.
5. Jhunlyn Lorenzo, Roman Vuillaume, Stéphane Binczak, and Sabir Jacquir. Spatiotemporal model of tripartite synapse with perinodal astrocytic process. *Journal of Computational Neuroscience*, 48(1):1–20, December 2019.
6. David Attwell and Nicola B Hamilton. Do astrocytes really exocytose neurotransmitters? *Nature reviews. Neuroscience*, 11(4):227–238, 2010.
7. Ada J Ellingsrud, Andreas Solbrå, Gaute T Einevoll, Geir Halnes, and Marie E Rognes. Finite element simulation of ionic electrodiffusion in cellular geometries. *Frontiers in Neuroinformatics*, 14:11, 2020.
8. Ada J. Ellingsrud, Cécile Daversin-Catty, and Marie E. Rognes. *A Cell-Based Model for Ionic Electrodiffusion in Excitable Tissue*, pages 14–27. Springer International Publishing, Cham, 2021.
9. Andreas Solbrå, Aslak Wigdahl Bergersen, Jonas van den Brink, Anders Malthe-Sørensen, Gaute T Einevoll, and Geir Halnes. A kirchhoff-nernst-planck framework for modeling large scale extracellular electrodiffusion surrounding morphologically detailed neurons. *PLoS computational biology*, 14(10):e1006510, 2018.
10. *Modeling Excitable Tissue : The EMI Framework*. Reports on Computational Physiology, 7. 1st ed. 2021.. edition, 2021.
11. Thomas E Chater and Yukiko Goda. The role of ampa receptors in postsynaptic mechanisms of synaptic plasticity. *Frontiers in cellular neuroscience*, 8:401–401, 2014.
12. John D Clements, Robin AJ Lester, Gang Tong, Craig E Jahr, and Gary L Westbrook. The Time Course of Glutamate in the Synaptic Cleft. *Science*, 258(5087):1498–1501, 1992.
13. Peter Jonas. The Time Course of Signaling at Central Glutamatergic Synapses. *Physiology*, 15(2):83–89, 2000.
14. Shivendra G Tewari and Kaushik Kumar Majumdar. A mathematical model of the tripartite synapse: astrocyte-induced synaptic plasticity. *Journal of Biological Physics*, 38(3):465–496, May 2012.
15. Alain Detexhe, Zachary F Mainen, and Terrence J Sejnowski. Chapter 1, Kinetic Models of Synaptic Transmission. In C Koch and I Segev, editors, *Methods in Neural Modelling*, pages 1–25. MIT Press, Cambridge, MA, 2nd edition edition, 1998.
16. Shaimaa Mahmoud, Marjan Gharagozloo, Camille Simard, and Denis Gris. Astrocytes maintain glutamate homeostasis in the cns by controlling the balance between glutamate uptake and release. *Cells (Basel, Switzerland)*, 8(2):184, 2019.
17. MS Alnæs, J Blechta, J Hake, A Johansson, B Kehlet, A Logg, C Richardson, J Ring, ME Rognes, and GN Wells. The fenics project version 1.5, arch. numerical softw., 3, 9–23, 2015.
18. Stephen E Farinelli and William J Nicklas. Glutamate metabolism in rat cortical astrocyte cultures. *Journal of Neurochemistry*, 58(5):1905–1915, 1992.
19. Luís L Fonseca, Miguel AR Monteiro, Paula M Alves, Manuel JT Carrondo, and Helena Santos. Cultures of rat astrocytes challenged with a steady supply of glutamate: New model to study flux distribution in the glutamate-glutamine cycle. *Glia*, 51(4):286–296, 2005.
20. Alan L Hodgkin and Andrew F Huxley. A quantitative description of membrane current and its application to conduction and excitation in nerve. *The Journal of physiology*, 117(4):500, 1952.

21. Julia Langer, Niklas J Gerkau, Amin Derouiche, Christian Kleinhans, Behrouz Moshrefi-Ravasdjani, Michaela Fredrich, Karl W Kafitz, Gerald Seifert, Christian Steinhäuser, and Christine R Rose. Rapid sodium signaling couples glutamate uptake to breakdown of atp in perivascular astrocyte endfeet. *Glia*, 65(2):293–308, 2017.

Open Access This chapter is licensed under the terms of the Creative Commons Attribution 4.0 International License (<http://creativecommons.org/licenses/by/4.0/>), which permits use, sharing, adaptation, distribution and reproduction in any medium or format, as long as you give appropriate credit to the original author(s) and the source, provide a link to the Creative Commons license and indicate if changes were made.

The images or other third party material in this chapter are included in the chapter's Creative Commons license, unless indicated otherwise in a credit line to the material. If material is not included in the chapter's Creative Commons license and your intended use is not permitted by statutory regulation or exceeds the permitted use, you will need to obtain permission directly from the copyright holder.





Chapter 6

Inducing Flow Instabilities in Aneurysm Geometries via the Reynolds-Orr Method

Alessandro Contri, Christina Taylor, Justin Tso, and Ingeborg Gjerde

Abstract Ruptured intracranial aneurysms are the leading cause of hemorrhagic strokes. Although intracranial aneurysms are prevalent in as much as 4% of the adult population, most aneurysms do not rupture, and their growth and risk of rupture remains difficult to predict. Previous studies have identified abnormal wall shear stress patterns and blood pressure spikes, both features of unstable flows, as key factors in aneurysm behavior. While computational fluid dynamics has been enlisted to help study risk of rupture, no consensus has been established on how to impose unstable flow conditions. Here, we use Reynolds-Orr instability analysis to calculate flow perturbations that are capable of inducing unstable flow in 3D arterial geometries with and without aneurysms. These perturbations lay the foundation for future wall shear stress studies by providing mathematically consistent conditions for time-dependent Navier-Stokes simulations.

6.1 Introduction

Intracranial aneurysms are relatively common in adults, with a global prevalence of 2-3%. Intracranial aneurysm rupture leads to aneurysmal subarachnoid hemorrhage, which is fatal in about 60% of cases and carries major risk of brain damage and

Alessandro Contri
Department of Mathematical Sciences, Norwegian University of Science and Technology, NO

Christina Taylor
Department of Computational and Applied Mathematics and Operations Research, Rice University, USA

Justin Tso
Department of Biomedical Engineering, Johns Hopkins University, USA

Ingeborg Gjerde (corresponding author)
Department of Numerical Analysis and Scientific Computing, Simula Research Laboratory, NO
e-mail: ingeborg@simula.no

disability for survivors [1]. However, only 1-2% of intracranial aneurysms rupture annually, and most are asymptomatic [2]. The decision to treat unruptured aneurysms must therefore be carefully weighed against the risk of rupture, a metric that remains difficult to quantify.

Aneurysm growth and rupture have been linked to local hemodynamic conditions, with wall shear stress (WSS) primary among them [3]. Computational fluid dynamics (CFD) studies allow for the high-resolution investigation of WSS in patient-specific arterial geometries through simulations of the Navier-Stokes equations. Several CFD studies have investigated the role of WSS in aneurysm rupture with conflicting results. While some studies have attributed risk of rupture to high WSS at thin and hard aneurysm walls, more recent studies have found strong relationships with low WSS at aneurysm rupture points (reviewed in [4]). Meng *et al.* have noted that both high and low WSS may increase rupture risk: high WSS causes degeneration of the cellular matrix and cell apoptosis, while low WSS and recirculation promotes an inflammatory environment that weakens the arterial wall and drives aneurysm growth [5].

Several studies have found rapid fluctuations in blood pressure to be a common risk factor for aneurysm rupture. Wouter *et al.* found that 43% of ruptures occurred during stressful events, while Vlak *et al.* found high population-attributable risks for coffee drinking and vigorous physical exercise [6, 7]. Matsuda *et al.* also found high incidence of rupture in activities associated with the Valsalva maneuver, which results in sudden pressure changes across the aneurysm wall [8]. These perturbations in flow are highly relevant to aneurysm rupture, but are not accounted for in most CFD studies.

These flow instabilities can be investigated using definitions of instability based on kinetic energy, which originated with Reynolds and Orr [9]. Analysis using these definitions, as revisited by Scott, provides an exact relation between a base flow and the evolution of the kinetic energy of a perturbation. The method is nonlinear with no approximations and yields a well-posed linear symmetric eigenvalue problem that can be solved with standard methods. In the resulting eigenpairs the flow perturbations are captured in the eigenvectors, while negative eigenvalues indicate the potential for instability with respect to kinetic energy. In unstable eigenpairs, the magnitude of the eigenvalues indicates the initial growth rates of the perturbed kinetic energy. However, the most energetically unstable eigenpair is a function of both the magnitude of its eigenvalue and its eigenvector [9].

While the Reynolds-Orr eigenpairs may not exactly reflect physiological flow instabilities, they provide a reproducible way to induce flow instability. The readily available mathematical framework behind this approach allows this analysis to easily be reproduced in different arterial geometries. In this work, we investigate some of the nuances of using this approach to induce unstable flow on arterial geometries with and without aneurysms taken from the Aneurisk data set from Emory University [10].

In the remainder of this paper, we will first discuss the Reynolds-Orr method in more detail in Section 6.2.1 followed by the details of our time-dependent Navier-Stokes solver in Section 6.2.2. Next, we will present some of our initial findings on

using the Reynolds-Orr to induce instability in Section 6.3 before concluding with a discussion on our findings in Section 6.4.

6.2 Methods

In this section we consider the mathematical equations and the subsequent implementation of the problem at hand, part of which was previously presented in [11]. The artery is considered as a pipe with a no-slip wall and prescribed pressures at the inlet and outlets. The absolute pressure is disregarded as it does not change the relative pressure drop in the model.

6.2.1 Reynolds-Orr Instability

The derivation of the eigenvalue problem from which we hope to detect the most unstable modes, given the base flow, follows the one presented in [9]. The derivation is nontrivial for pressure boundary conditions; therefore, we consider here only Dirichlet boundary conditions for the velocity. Let (\mathbf{u}, p) be the solution to the following unsteady Navier-Stokes equations:

$$\partial_t \mathbf{u} - \nu \Delta \mathbf{u} + \mathbf{u} \cdot \nabla \mathbf{u} + \nabla p = \mathbf{f} \quad \text{in } \Omega \times (0, T], \quad (6.1)$$

$$\nabla \cdot \mathbf{u} = 0 \quad \text{in } \Omega \times (0, T], \quad (6.2)$$

$$\mathbf{u} = \mathbf{g} \quad \text{on } \partial\Omega \times (0, T], \quad (6.3)$$

$$\mathbf{u} = \mathbf{u}^0 \quad \text{on } \Omega \times \{0\}. \quad (6.4)$$

Let now the couple (\mathbf{w}, q) solve the same equations (6.4) with the same boundary condition \mathbf{g} , but different initial data \mathbf{w}^0 , such that $\mathbf{w}^0 \neq \mathbf{u}^0$. Define (\mathbf{v}, o) as the difference between the two solutions:

$$\mathbf{v} = \mathbf{u} - \mathbf{w}, \quad o = p - q. \quad (6.5)$$

Then, taking the two versions of (6.4) with the different initial data and subtracting them, (\mathbf{v}, o) satisfy:

$$\partial_t \mathbf{v} - \nu \Delta \mathbf{v} + (\mathbf{u} \cdot \nabla \mathbf{u} - \mathbf{w} \cdot \nabla \mathbf{w}) + \nabla o = \mathbf{0} \quad \text{in } \Omega \times (0, T], \quad (6.6)$$

$$\nabla \cdot \mathbf{v} = 0 \quad \text{in } \Omega \times (0, T], \quad (6.7)$$

$$\mathbf{v} = \mathbf{0} \quad \text{on } \partial\Omega \times (0, T], \quad (6.8)$$

$$\mathbf{v} = \mathbf{v}^0 = \mathbf{u}^0 - \mathbf{w}^0 \quad \text{on } \Omega \times \{0\}. \quad (6.9)$$

Following [9], the nonlinear term is rewritten as

$$\mathbf{u} \cdot \nabla \mathbf{u} - \mathbf{w} \cdot \nabla \mathbf{w} = \mathbf{u} \cdot \nabla \mathbf{u} - \mathbf{u} \cdot \nabla \mathbf{w} + \mathbf{u} \cdot \nabla \mathbf{w} \mathbf{w} \cdot \nabla \mathbf{w} \quad (6.10)$$

$$= \mathbf{u} \cdot \nabla \mathbf{v} + \mathbf{v} \cdot \nabla \mathbf{w} = \mathbf{u} \cdot \nabla \mathbf{v} + \mathbf{v} \cdot \nabla \mathbf{u} - \mathbf{v} \cdot \nabla \mathbf{v} \quad (6.11)$$

Multiplying (6.9) by \mathbf{v} , using (6.11) and integrating over Ω yields

$$(\partial_t \mathbf{v}, \mathbf{v}) + a(\mathbf{v}, \mathbf{v}) + c(\mathbf{u}, \mathbf{v}, \mathbf{v}) + c(\mathbf{v}, \mathbf{u}, \mathbf{v}) - c(\mathbf{v}, \mathbf{v}, \mathbf{v}) - b(\mathbf{v}, o) = 0. \quad (6.12)$$

where (\cdot, \cdot) denotes the standard $L^2(\Omega)$ inner product and

$$a(\mathbf{u}, \mathbf{v}) = \nu \int_{\Omega} \nabla \mathbf{u} : \nabla \mathbf{v}, \quad (6.13)$$

$$c(\mathbf{u}, \mathbf{v}, \mathbf{w}) = \int_{\Omega} (\mathbf{u} \cdot \nabla \mathbf{v}) \cdot \mathbf{w}, \quad (6.14)$$

$$b(\mathbf{u}, p) = \int_{\Omega} \nabla \cdot \mathbf{u} p. \quad (6.15)$$

Defining now the following space:

$$\mathbf{V} := \{\mathbf{v} \in H^1(\Omega)^3 : \nabla \cdot \mathbf{v} = 0 \text{ and } \mathbf{v} = 0 \text{ on } \partial\Omega\} \quad (6.16)$$

it can be observed from [9] that for any $\mathbf{w} \in \mathbf{V}$ one have

$$c(\mathbf{w}, \mathbf{v}, \mathbf{v}) = 0, \quad b(\mathbf{v}, o) = 0. \quad (6.17)$$

(6.12) can then be rewritten in the form

$$\frac{1}{2} \frac{\partial}{\partial t} \int_{\Omega} |\mathbf{v}|^2 = -\nu \int_{\Omega} |\nabla \mathbf{v}|^2 - \int_{\Omega} (\mathbf{v} \cdot \nabla \mathbf{u}) \cdot \mathbf{v} \quad (6.18)$$

$$= -\nu \int_{\Omega} |\nabla \mathbf{v}|^2 - \frac{1}{2} \int_{\Omega} \mathbf{v}^T (\nabla \mathbf{u} + \nabla \mathbf{u}^T) \mathbf{v}. \quad (6.19)$$

The first term of the equation can be seen as the time derivative of the kinetic energy of the flow and the right hand side describes its evolution. Following standard arguments (i.e. integration in time of the left hand side etc.) we can say that the flow \mathbf{u} is energy unstable at time $t = 0$ if there exists a $\mathbf{v}_0 \in \mathbf{V}$ such that

$$-\frac{1}{2} \int_{\Omega} \mathbf{v}_0^T (\nabla \mathbf{u}_0 + \nabla \mathbf{u}_0^T) \mathbf{v}_0 - \nu \int_{\Omega} |\nabla \mathbf{v}_0|^2 > 0. \quad (6.20)$$

At this point we define

$$\lambda_{\mathbf{v}} = \frac{B_{\mathbf{u}}(\mathbf{v}, \mathbf{v})}{a(\mathbf{v}, \mathbf{v})} \quad \text{with} \quad B_{\mathbf{u}}(\mathbf{v}, \mathbf{w}) = \frac{1}{2} \int_{\Omega} \mathbf{v}^T (\nabla \mathbf{u} + \nabla \mathbf{u}^T) \mathbf{w} \quad (6.21)$$

Comparing (6.19) with (6.21) we can reformulate an equivalent instability condition. Namely, the flow is unstable at $t = 0$ if there is a $\mathbf{v}_0 \in \mathbf{V}$ such that

$$\lambda_{\mathbf{v}_0} < 1. \quad (6.22)$$

Given that $a(\mathbf{v}, \mathbf{v}) = \nu \|\nabla \mathbf{v}\|^2$, we have in particular that if $\exists \mathbf{v}$ such that $\lambda = \inf_{0 \neq \mathbf{v} \in \mathbf{V}} \lambda_{\mathbf{v}} < -1$ and thus

$$\left(\frac{1}{\|\nabla \mathbf{v}\|^2} \right) \frac{\partial}{\partial t} \int_{\Omega} |\mathbf{v}|^2 = -2\nu(1 + \lambda_{\mathbf{v}}) > 0, \quad (6.23)$$

the flow is unstable. Recalling Poincaré's inequality, stating $\|\mathbf{v}\|^2 \leq C_P \|\nabla \mathbf{v}\|^2 \quad \forall \mathbf{v} \in \mathbf{V}$, we can deduce

$$\frac{\partial}{\partial t} \log \left(\int_{\Omega} |\mathbf{v}|^2 \right) \geq -\frac{2\nu}{C_P} (1 + \lambda_{\mathbf{v}}). \quad (6.24)$$

We conclude that the most negative $\lambda_{\mathbf{v}}$ leads to the most unstable mode. However, as noted in [9], the most unstable mode may not be the most persistent. Additionally, [9] proves that the solution to $\lambda = \inf_{0 \neq \mathbf{v} \in \mathbf{V}} \lambda_{\mathbf{v}}$ solves the eigenvalue problem $(\lambda, \mathbf{v}) \in (\mathbb{R}, \mathbf{V})$ such that

$$B_{\mathbf{u}}(\mathbf{v}, \mathbf{w}) = \lambda a(\mathbf{v}, \mathbf{w}) \quad \forall \mathbf{w} \in \mathbf{V}. \quad (6.25)$$

The detailed derivation can be found in [9].

6.2.2 Unsteady Navier-Stokes FEM Discretization

We looked to study the evolution in time of the potentially unsteady modes detected using the method described previously. In order to progress in time we needed to implement a time-dependent Navier-Stokes solver. To do so, we used a splitting method, which despite its low accuracy in time is fast and easy to implement from the computational point of view. The motivation behind splitting schemes is to consider the first two equations in 6.4 separately. We chose a modified version of Chorin's method [12], the so-called incremental pressure correction scheme (IPCS) [13], which gives improved accuracy compared to the original scheme at little extra cost.

The IPCS scheme involves three steps. First, we compute a tentative velocity \mathbf{u}^* by advancing the momentum equation (6.4) by a midpoint finite difference scheme in time, using the pressure p^n from the previous time interval. We also linearize the nonlinear convective term by using the known velocity \mathbf{u}^n from the previous time step: $\mathbf{u}^n \cdot \nabla \mathbf{u}^n$. The variational problem for this first step is

$$((\mathbf{u}^* - \mathbf{u}^n) \Delta t, \mathbf{v}) + (\mathbf{u}^n \cdot \nabla \mathbf{u}^n, \mathbf{v}) + a(\mathbf{u}^{n+\frac{1}{2}}, \mathbf{v}) - b(\mathbf{v}, p^n) \quad (6.26)$$

$$+ (p^n \mathbf{n}, \mathbf{v})_{\partial\Omega} - \nu (\nabla \mathbf{u}^{n+\frac{1}{2}} \cdot \mathbf{n}, \mathbf{v})_{\partial\Omega} = (\mathbf{f}^{n+1}, \mathbf{v}) \quad (6.27)$$

where

$$(\mathbf{u}, \mathbf{v})_{\partial\Omega} = \int_{\partial\Omega} \mathbf{u} \mathbf{v} ds, \quad \mathbf{u}^{n+\frac{1}{2}} = (\mathbf{u}^n + \mathbf{u}^{n+1})/2. \quad (6.28)$$

Since we are modeling flow in a "pipe" (the artery) with known inflow and outflow, the scheme has the hidden assumption that the derivative of the velocity in the direction of the channel is zero at the inflow and outflow, corresponding to a flow that is "fully developed," or that the flow field doesn't change significantly upstream or downstream of the domain.

The second step is to use the computed tentative velocity to compute the new pressure p^n :

$$(\nabla p^{n+1}, \nabla q) = (\nabla p^n, \nabla q) - \Delta t^{-1} (\nabla \cdot \mathbf{u}^*, q) \quad (6.29)$$

Finally, we compute the corrected velocity \mathbf{u}^{n+1} :

$$(\mathbf{u}^{n+1}, \mathbf{v}) = (\mathbf{u}^*, \mathbf{v}) - \Delta t (\nabla(p^{n+1} - p^n), \mathbf{v}). \quad (6.30)$$

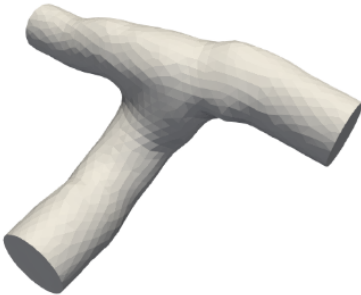
In summary, we solve the incompressible Navier–Stokes equations efficiently by solving a sequence of three linear variational problems in each time step. The FEM space chosen to solve the problem is $(\mathbf{u}_h, p_h) \in (\mathbf{V}_{\Gamma, h}^2, \mathbf{V}_h^1)$ where, if we let \mathbf{V}_h^k denote the space of C^k piecewise polynomials of degree k on a regular mesh of the domain Ω , the vector valued polynomial space is

$$\mathbf{V}_{\Gamma, h}^k = \{\mathbf{v} \in (\mathbf{V}_h^k)^3 : \mathbf{v}|_{\partial\Omega \setminus \Gamma} = 0\}. \quad (6.31)$$

6.3 Results

For our numerical experiments we used a single artery mesh both with and without an aneurysm. These geometries are shown in Figure 6.1.

Case 0



Case 1

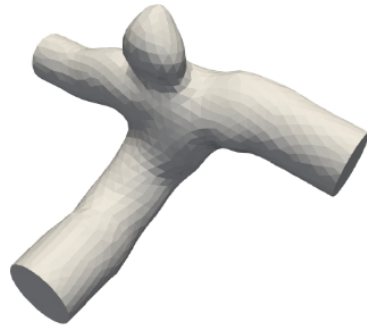


Fig. 6.1: The artery geometry without (Case 0) and with (Case 1) an aneurysm used for our numerical experiments.

As previously stated, eigenvalues with negative sign and magnitude greater than one are necessary to induce energy instability. Eigenpairs were computed using a shifted power iteration with LU preconditioning to target eigenvalues near -1. We observed that without a sufficient pressure drop, eigenvalues less than or equal to -1 were not guaranteed. Using $\Delta p = 600\text{Pa}$ (4.5mmHg) and 1000Pa (7.5mmHg) both yielded at least two eigenvalues less than -1 in both the healthy artery and terminal aneurysm. Tables 6.1 and 6.2 show the eigenvalues reported by the solver. Figures 6.2 and 6.3 show example perturbations associated with the $\Delta p = 600\text{Pa}$ pressure drop case.

Table 6.1: Eigenvalues for the healthy artery without an aneurysm for different pressure drop values.

N	$\Delta p=600\text{Pa}$ (4.5mmHg)	$\Delta p=1000\text{Pa}$ (7.5mmHg)
0	-1.116	-1.778
1	-1.091	-1.623
2	-0.874	-1.319
3	-0.775	-1.163
4	0.871	1.265
5	0.964	1.402

Table 6.2: Eigenvalues for the artery with an aneurysm for different pressure drop values.

N	$\Delta p=600\text{Pa}$ (4.5mmHg)	$\Delta p=1000\text{Pa}$ (7.5mmHg)
0	-1.154	-1.865
1	-1.125	-1.697
2	-0.903	-1.404
3	-0.785	-1.191
4	0.875	1.160
5	0.970	1.279
6	*	1.443

* The 600Pa pressure drop did not yield a sixth eigenvalue near ± 1 .

With the eigenpairs in hand, it remained to simulate the kinetic energy evolution of the eigenpairs with eigenvalues less than -1. The Navier-Stokes equations are notoriously difficult to simulate especially in the face of physical instabilities. In the case of our scheme a severely prohibitive time step was needed to ensure numerical stability. The prohibitive time step coupled with a lack of computing resources

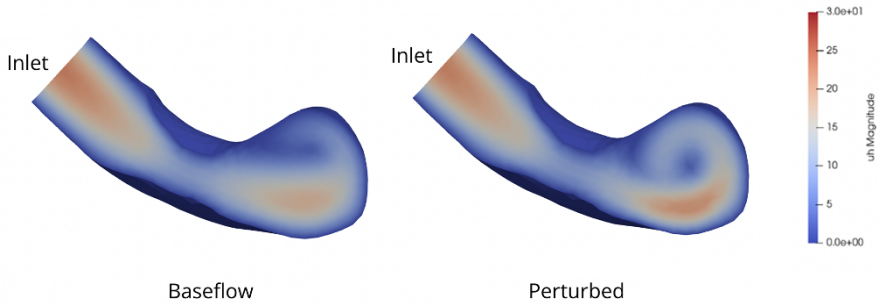


Fig. 6.2: Example of the base flow without and with perturbation added in the healthy artery case for $\Delta p = 600\text{Pa}$.

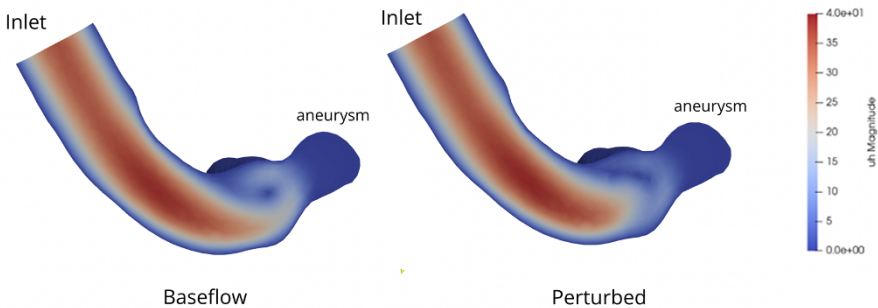


Fig. 6.3: Example of base flow without and with perturbation added in the aneurysm case for $\Delta p = 600\text{Pa}$.

restricted us from being able to perform in-depth analysis of the kinetic energy evolution. However, we were able to calculate the kinetic energy evolution for the above eigenpairs over a very short time period. Figures 6.4 and 6.5 show the L2 norm of the velocity (the kinetic energy) of the solutions over a time period of 0.1 seconds.

6.4 Discussion

From our initial results, only four eigenpairs seem to induce unstable flow as indicated by increasing kinetic energy despite there being 16 negative eigenvalues. However, as shown in Figure 6.4 for the 1000Pa case with $\lambda = -1.319$, it seems possible for the kinetic energy to initially decrease before increasing. This is not completely unexpected as [9] showed the kinetic energy can oscillate, though in their experiments

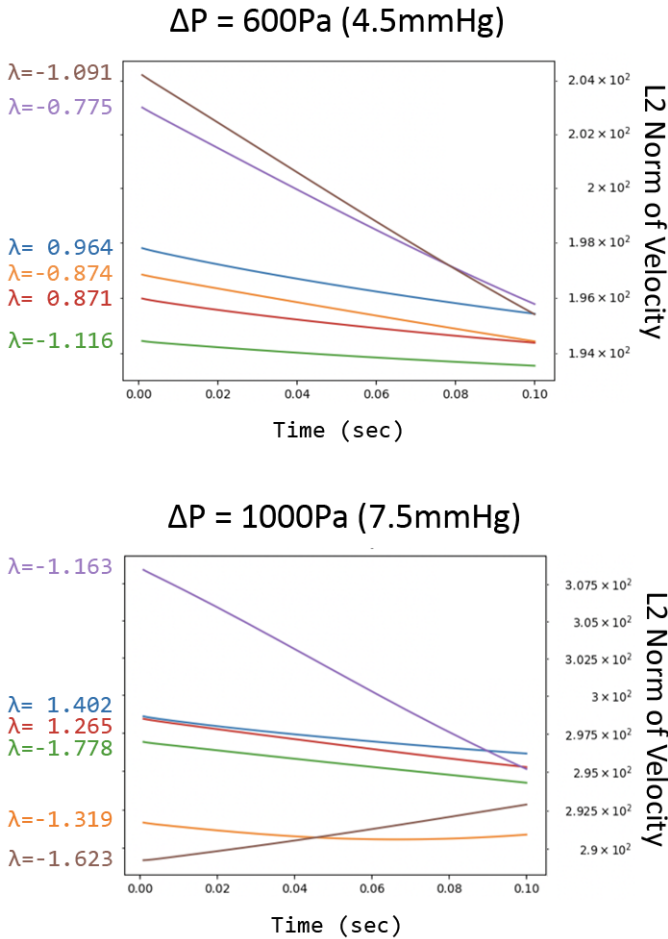


Fig. 6.4: Evolution of the L2 norm of the velocity in time for healthy artery eigenpairs.

this oscillation was coupled to an overall decay after an initial increase in energy. Our short simulation time may not have been sufficient to capture instabilities that require more time to develop. Additionally, as was noted in [9] a larger magnitude negative eigenvalue does not necessarily guarantee the most unstable mode due to the instability’s additional dependence on the gradient of the perturbed velocity. In Figure 6.5 this can be seen in the 1000Pa case by the eigenpair with $\lambda = -0.785$ inducing an initial increase in energy while the eigenpair with $\lambda = -1.154$ did not.

While the restrictive time step required by the Navier-Stokes solver did not allow us to complete all initial goals of this project, we have been able to show some preliminary results showing that perturbations computed using the Reynolds-Orr method can induce energy instability for a given geometry. Future work would entail longer simulations to confirm whether all negative eigenvalues with sufficient

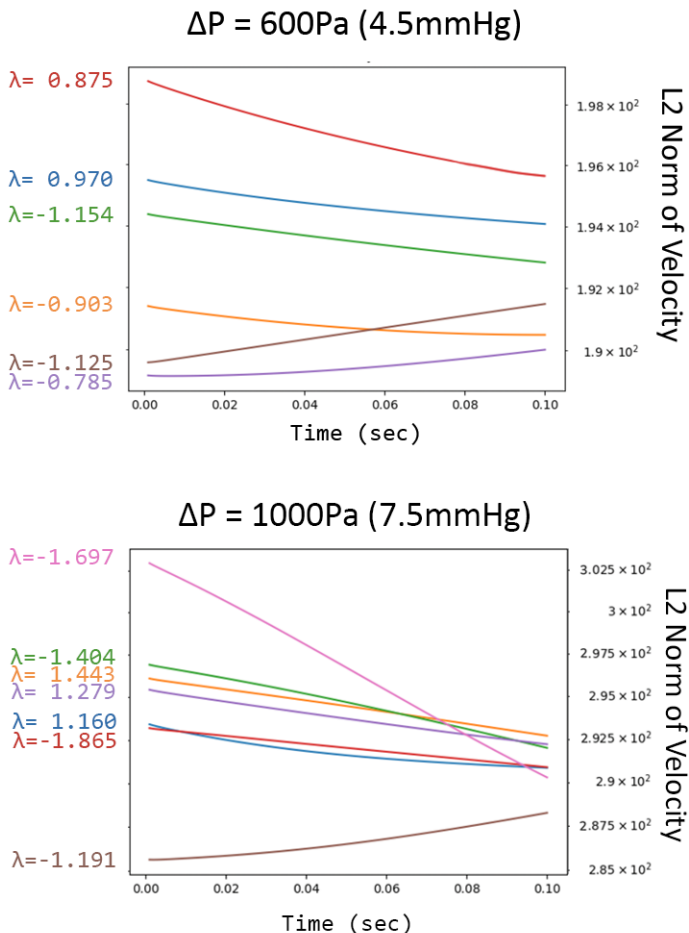


Fig. 6.5: Evolution of the L2 norm of the velocity in time for the aneurysm eigenpairs.

magnitude do lead to instability eventually. Additionally, we have completed the work started in [11] by correcting errors that had previously made when calculated the eigenmodes. The codes produced here provide the framework needed to continue studying aneurysm rupture risk through the Reynolds-Orr instability analysis when provided sufficient computing resources.

References

1. Marilyn M Rymer. Hemorrhagic stroke: intracerebral hemorrhage. *Missouri medicine*, 108(1):50, 2011.
2. Gabriel JE Rinkel, Mamuka Djibuti, Ale Algra, and J Van Gijn. Prevalence and risk of rupture of intracranial aneurysms: a systematic review. *Stroke*, 29(1):251–256, 1998.
3. Mahsa Dabagh, Priya Nair, John Gounley, David Frakes, L Fernando Gonzalez, and Amanda Randles. Hemodynamic and morphological characteristics of a growing cerebral aneurysm. *Neurosurgical focus*, 47(1):E13, 2019.
4. Yuichi Murayama, Soichiro Fujimura, Tomoaki Suzuki, and Hiroyuki Takao. Computational fluid dynamics as a risk assessment tool for aneurysm rupture. *Neurosurgical focus*, 47(1):E12, 2019.
5. H Meng, VM Tutino, J Xiang, and A Siddiqui. High wss or low wss? complex interactions of hemodynamics with intracranial aneurysm initiation, growth, and rupture: toward a unifying hypothesis. *American Journal of Neuroradiology*, 35(7):1254–1262, 2014.
6. Wouter I Schievink, John M Karemaker, Loes M Hageman, and Dries JM van der Werf. Circumstances surrounding aneurysmal subarachnoid hemorrhage. *Surgical neurology*, 32(4):266–272, 1989.
7. Monique HM Vlak, Gabriel JE Rinkel, Paut Greebe, Johanna G van der Bom, and Ale Algra. Trigger factors and their attributable risk for rupture of intracranial aneurysms: a case-crossover study. *Stroke*, 42(7):1878–1882, 2011.
8. Masayuki Matsuda, Kazuyoshi Watanabe, Akira Saito, Ken-ichi Matsumura, and Masaharu Ichikawa. Circumstances, activities, and events precipitating aneurysmal subarachnoid hemorrhage. *Journal of Stroke and Cerebrovascular Diseases*, 16(1):25–29, 2007.
9. L Ridgway Scott. Kinetic energy flow instability with application to couette flow. Technical report, Technical Report TR-2020-07, 2020.
10. AW Bergersen, HA Kjeldsberg, and K Valen-Sendstad. Kvslab. <http://ecm2.mathcs.emory.edu/aneuriskweb/index>, 2021. Accessed August 2022.
11. Nanna Berre, Gabriela Castro, Henrik Kjeldsberg, Rami Masri, and Ingeborg Gjerde. A computational study of flow instabilities in aneurysms. In *Simula SpringerBriefs on Computing*, pages 63–75. Springer, Cham, 2022.
12. Alexandre Joel Chorin. The numerical solution of the navier-stokes equations for an incompressible fluid. *Bulletin of the American Mathematical Society*, 73(6):928–931, 1967.
13. Katuhiko Goda. A multistep technique with implicit difference schemes for calculating two- or three-dimensional cavity flows. *Journal of computational physics*, 30(1):76–95, 1979.

Open Access This chapter is licensed under the terms of the Creative Commons Attribution 4.0 International License (<http://creativecommons.org/licenses/by/4.0/>), which permits use, sharing, adaptation, distribution and reproduction in any medium or format, as long as you give appropriate credit to the original author(s) and the source, provide a link to the Creative Commons license and indicate if changes were made.

The images or other third party material in this chapter are included in the chapter's Creative Commons license, unless indicated otherwise in a credit line to the material. If material is not included in the chapter's Creative Commons license and your intended use is not permitted by statutory regulation or exceeds the permitted use, you will need to obtain permission directly from the copyright holder.





Chapter 7

Impact of Pathological Vascular Remodelling on Right Ventricular Mechanics

Jiaxin (Katie) Cui*, Mariluz Rojo Domingo*, Ryan Konno*, Claudia A Manetti*, George Kagugube*, Oscar Odeigah, and Joakim Sundnes

* These authors contributed equally to this work

Abstract Pulmonary arterial hypertension (PAH) is a rare disorder characterized by elevated blood pressure and pulmonary vascular resistance, often followed by right ventricular hypertrophy and heart failure. The effect of PAH and its treatments on the mechanics, function, and remodelling of the right ventricle (RV) is currently not well understood. To study cardiac biomechanics and functionality as PAH progresses, we implemented a computational model of the heart simulating right ventricular maladaptive remodelling. Our Windkessel-based model, which accounts for direct ventricular interaction and the presence of the pericardium, is utilized to simulate various disease stages of PAH. We find that the pericardium has a larger effect on heart performance than ventricular interaction through the septum. We also examined the effectiveness of two treatments, ventricular assist device (RVAD) and atrial septostomy, on diseased hearts. We show that while both pulsatile and continuous RVADs restore cardiac function, pulsatile RVAD improves cardiac output 29.4% more than continuous RVAD. We also demonstrate that atrial septostomy improves

Jiaxin (Katie) Cui

Department of Biomedical Engineering, Viterbi School of Engineering, University of Southern California, USA

Mariluz Rojo Domingo

Department of Bioengineering, University of California, San Diego, USA

Ryan Konno

Department of Mathematics, Simon Fraser University, CA

Claudia A Manetti

Maastricht University, NL

George Kagugube

University College London, UK

Oscar Odeigah

Department of Computational Physiology, Simula Research Laboratory, NO

Joakim Sundnes (corresponding author)

Department of Computational Physiology, Simula Research Laboratory, NO e-mail: sundnes@simula.no

cardiac output by 19.5%. Our model can be further extended by simulating the heart's response to other treatments such as extracorporeal membrane oxygenation (ECMO), and by incorporating ventricular remodelling growth simulations and finite-element ventricular modelling.

7.1 Introduction

Pulmonary arterial hypertension (PAH) is characterized by high blood pressure and high pulmonary vascular resistance in the arteries in the lungs [1]. As the pressure and resistance in the pulmonary arteries and capillaries rises, the right ventricular afterload is elevated. Over time, there is a larger demand for work done by the heart to achieve the same level of cardiac output as that of a healthy one. To increase the amount of contractile force generated by the heart, the right ventricle (RV) undergoes abnormal enlargement and increases its wall thickness, stiffness, and contractility. This phenomenon, which is observed in almost all PAH patients, is referred to as right ventricular hypertrophy [2]. Moreover, the heart compensates for the elevation in pulmonary arterial pressure and resistance via vascular proliferation and remodelling of small pulmonary arteries [3]. In advanced stages of PAH, the severe dilation of the RV causes septal bowing, i.e., a leftward shift of the septum that lowers left ventricular volume and limits left ventricular filling. Hence, left ventricular output is reduced and, in turn, cardiac output and mean arterial pressure decrease [4]. All these compensatory mechanisms enable the heart to maintain its performance in the early stages of PAH; however, sustained structural and functional changes in the RV can eventually become detrimental to cardiac function and may even result in right heart failure and death of a patient [5].

Although life-threatening, PAH remains incurable. Treatment strategies are available to alleviate the vascular symptoms (e.g., vasoconstriction) [6], and to delay disease progression by unloading the RV. Therapies proven to be effective in PAH patients include: drugs in the form of vasodilators, inotropes and anticoagulants; extracorporeal membrane oxygenation (ECMO) devices; mechanical support via a right ventricular assist device (RVAD); atrial septostomy; or lung transplantation. [7]. Multiple *in situ* and *in silico* investigations focus on PAH, yet there is still a gap in our understanding of the biomechanic and hemodynamic effect of PAH on the RV and its subsequent remodeling (and failure). [3, 4, 8, 9, 10] Furthermore, the progressive remodeling of the RV is inevitably influenced by its surrounding environment; in other words, the septum, the pericardium, the left ventricle (LV), and baroreflex must be considered in order to investigate RV performance in PAH as accurately as possible. Some computational studies have already looked into changes in heart function with ventricular interdependence under the influence of pericardium and baroreflex. [11, 12, 13] Nonetheless, most rigorous biomechanical and hemodynamic models have yet to be utilized for research involving treatments of PAH and right ventricular remodelling. Our objective was to develop a realistic computational model that simulates the heart conditions in a PAH setting to gain

insight into the various maladaptations characteristic of this condition as well as the effect of PAH treatments on RV mechanics. Our theoretical analysis supplements experimental research techniques to further enhance our knowledge of PAH therapies and how the progressive adverse remodeling impacts the biomechanics and hemodynamics of the heart.

7.2 Methods

In this work, we implement a closed-loop, lumped-parameter model of the heart and the circulatory system [8, 12] to study the impact of increased pulmonary vascular resistance on RV hemodynamics. This Windkessel-based model captures the effects of PAH at different severities while accounting for direct ventricular interaction via the interventricular septum, the pericardium constraint, baroreflex, and the heart's dynamic growth and remodelling in response to varying loads. Moreover, our model is utilized to examine two treatment options for PAH-induced RV dysfunction. In particular, we investigate the impact of RVAD and atrial septostomy on cardiovascular hemodynamics in the PAH setting.

7.2.1 Base Model of PAH

Our model of the cardiovascular system combines elements of the cardiac anatomy with those of the systemic and pulmonary circulations. The pressure, volume, and blood flow through the circulatory system are represented using a set of ordinary differential equations. The relationship between the pressure and volume for each component in the circulatory system can be represented linearly by

$$V = CP + V_d,$$

where V is volume, P is pressure, C is the compliance of the vessel, and V_d is the volume of the vessel at zero pressure. While C and V_d of the arteries and veins are typically constant (unless there are physiological or pathological changes), C and V_d of the heart chambers are time-varying periodic functions that represent active contraction [14]. The circulatory system model consists of individual elastic chambers and a series of resistors and diodes with fixed and variable capacitors branching from the main circuit (Figure 7.1) [15]. The systemic and pulmonary vasculatures are divided into their corresponding resistive and fixed capacitive components due to their elastic nature. Heart valves reinforce uni-directional blood flow, so they are represented as diodes. In addition, the mitral and tricuspid valves exhibit non-negligible resistive elements to block blood flow between heart chambers. Systole and diastole, the two phases of the cardiac cycle, are captured by variable capacitors that represent the heart chambers.

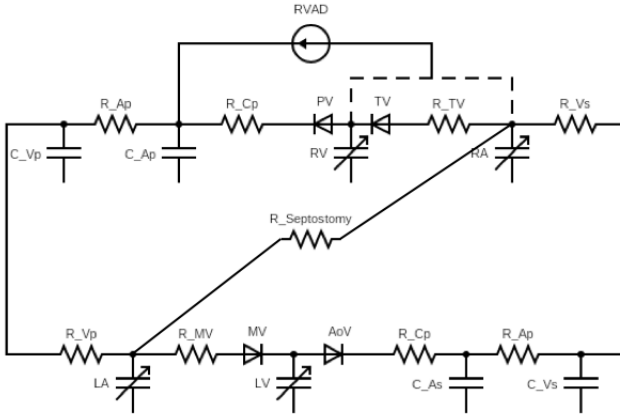


Fig. 7.1: Base Windkessel circulation model describing the coupling between the heart and the systemic and pulmonary circulation, including RVAD and atrial septostomy treatments.

The volume of each individual compartment is related to the rate of inflow and outflow via

$$\frac{dV_i}{dt} = Q_{in} - Q_{out}, \quad (7.1)$$

where V_i is the volume of chamber i , and Q_{in} and Q_{out} represent the flow in and out of the chamber, respectively. We approximate the blood flow at each component, which is driven by pressure difference, to be linearly dependent on pressure through the following relation:

$$Q = \frac{P_{upstream} - P_{downstream}}{R}, \quad (7.2)$$

where R is the resistance of the given connection.

Ventricular and atrial pumping characteristics are modelled by modifying time-varying elastance, $e(t)$. Mathematically, instantaneous ventricular pressure $P(t)$ can be related to instantaneous ventricular volume $V(t)$ via

$$P(t) = [P_{es}(V) - P_{ed}(V)] e(t) + P_{ed}(V), \quad (7.3)$$

where

$$P_{es}(V) = E_{es}(V - V_0), \quad (7.4)$$

$$P_{ed}(V) = \alpha(e^{\beta(V-V_0)} - 1), \quad (7.5)$$

$$e(t) = \begin{cases} \frac{1}{2} \left[\sin \left(\frac{\pi}{T_{es}} t - \frac{\pi}{2} \right) + 1 \right], & \text{if } 0 < t < \frac{3T_{es}}{2} \\ 0.5 \exp \left\{ \left(t - \frac{3T_{es}}{2} \right) / \tau \right\}, & \text{otherwise.} \end{cases} \quad (7.6)$$

Here, P_{es} is end-systolic pressure, P_{ed} is end-diastolic pressure, E_{es} is end-systolic elastance, T_{es} is time required to achieve end-systole, τ is the time constant of relaxation, and V_0 , α , β , are constant model parameters in the end-diastolic pressure-volume relationship. The parameters of the base model were adapted, based on Punnoose *et al.* [8], to capture different stages of PAH (mild, moderate, severe, and very severe, i.e., cardiogenic shock). We initialized the model with standard parameters for a healthy heart, and then varied its parameters to match those of the corresponding phase. When the parameters were altered for each diseased state, common RV function metrics, such as the stroke volume, the ejection fraction and cardiac output, changed too. We could thus observe a distinct pressure-volume relationship for each degree of right-sided heart failure before implementing any treatments. Overall, the most relevant parameters in the circulation model include systemic and pulmonary vessel resistance, compliance and elastance. The varying effects of most of these parameters on the model's behaviour was further explored by performing a sensitivity analysis.

7.2.2 Ventricular Interaction and the Pericardium

In this study, we aimed to improve the realism of the previously described lumped-parameter model by accounting for the interventricular interaction via the septum wall. The left and the right ventricles act independently of each other; their time-varying volume-elastance relation is represented by the system shown above in Equation 7.6. Following Santamore *et al.* [11], three time-varying elastances (right ventricular free wall E_{rvf} , left ventricular free wall E_{lvf} , and septum wall E_s) were considered, so that the interdependence between the two ventricles was simulated by our model. The pressures of both ventricles at the end of diastole (P_{ed}) becomes

$$P_{edLV}(V) = \alpha(e^{B_{lv}(V-V_0)} - 1), \quad (7.7)$$

where

$$B_{lv} = B_{l0} + m_{rl}V_{rv}, \quad (7.8)$$

and

$$P_{edRV}(V) = \alpha(e^{B_{rv}(V-V_0)} - 1), \quad (7.9)$$

where

$$B_{rv} = B_{r0} + m_{lr}V_{lv} \tag{7.10}$$

B_{l0} and B_{r0} represent the ventricular coefficients when the volume is equal to zero. m_{rl} is the sensitivity of A_{lv} to changes in right ventricular volume while m_{lr} is the sensitivity of A_{rv} to changes in left ventricular volume. The pressure development in each ventricle during systole is a function of pressure in the opposite ventricle. For the end-systolic relation, the pressure at the end of systole (P_{es}) of both ventricles is formulated as

$$P_{esLV} = \frac{E_s E_{lvf}}{E_s + E_{lvf}} (V_{lv} - V_{l0}) + \frac{E_{lvf} P_{rv}}{E_s + E_{lvf}}, \tag{7.11}$$

$$P_{esRV} = \frac{E_s E_{rvf}}{E_s + E_{rvf}} (V_{rv} - V_{r0}) + \frac{E_{rvf} P_{lv}}{E_s + E_{rvf}}. \tag{7.12}$$

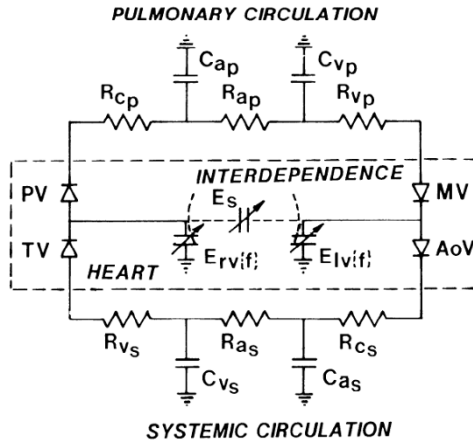


Fig. 7.2: Circuit used to simulate cardiovascular system with interaction from Santamore *et al.*[11]

We then proceeded to extend our model to account for the presence of the pericardium, a fibrous sac that encloses the four chambers of the heart. We followed the implementation from Burkoff *et al.* [12] in which the pericardial pressure ($P_{pericard}$) is assumed to be equal to an exponential function of the sum of instantaneous LV and RV volumes: $P_{pericard} = \alpha_p \exp[\beta_p (V_{lv} + V_{rv})]$.

7.2.3 Right Ventricular Remodelling and Baroreflex

The heart continuously regulates its output to match the needs of the body, but it also adapts its anatomy and behavior to changes in pulmonary arterial pressure. During PAH, the heart undergoes long-term deformations in the form of an increase in contractility, and subsequent augment in right ventricular wall volume, V_{wall} . Altered contractility, which is associated with changes in sarcomere length from the ideal optimal value, is evaluated in our model using the formulation from Arts *et al.* [16]. The sarcomere length can be calculated as

$$\lambda = \left(1 + 3 \frac{V_{rv}}{V_{wall}} \right)^{1/3}, \quad (7.13)$$

and the change in contractility required to reach such sarcomere length [17] is computed as

$$C = \frac{1+a}{1+a e^{b(L_0-L_{s,max})}}, \quad (7.14)$$

where $a = 0.2$, $b = 4\mu m^{-1}$ [16], L_0 is the desired sarcomere length, and $L_{s,max}$ is the maximum sarcomere length throughout the cycle. Once C has been calculated, wall volume (V_{wall}) and right ventricular contractility ($E_{es,rv}$) are respectively updated in an iterative process. Mathematically, a linear approximation from the previous iteration is used in both cases: $E_{es,rv}^n = C E_{es,rv}^{n-1}$ and $V_{wall}^n = C V_{wall}^{n-1}$.

A more short-term cardiac adaptation to changes in heart rate and contractility is baroreflex control. This homeostatic mechanism increases the heart rate when arterial pressure decreases, and vice versa [18]. Changes in the heart rate were simulated using the linear approximation [13] $T_r = G_{baro}(P_{ao} - 120) + 0.855$, where T_r is the cardiac period, P_{ao} is the systolic aortic pressure and G_{baro} (the baroreflex gain) is fixed at $0.005 s/mmHg$.

7.2.4 Atrial Septostomy

Atrial septostomy is a palliative treatment for medically refractory PAH. The procedure involves using a catheter to intentionally create a hole, called an atrial septostomy defect (ASD), in the interatrial septum. The direct blood flow from the right atrium into the left atrium increases cardiac output, thus alleviating right atrium pressure. As a result, the overall outflow resistance and afterload experienced by the right-side of the heart is reduced, enhancing survival. We account for atrial septostomy in our model by introducing a new lump-parameter for septostomy resistance, R_{sept} , and adding blood flow through the interatrial septal orifice governed by $Q_{sept} = K A \sqrt{|\Delta P|}$, where $A = \pi R^2$ is the area of the septostomy in cm^2 , ΔP is the pressure gradient across the orifice in $mmHg$, and $K = 2.66$.

7.2.5 Right Ventricular Assistive Device (RVAD)

PAH often leads to right ventricular failure, so often assistive devices (RVADs) are required. These devices can be used in a continuous flow capacity, where the flow continuously provides support to the RV independent of time; or as a pulsating RVAD, where the flow is time dependent and in sync with the cardiac cycle. Both continuous and pulsatile flow pumps have previously been tested computationally and experimentally [9, 19]. Additionally, the RVAD can be implemented in either the right ventricle or right atrium. To implement the RVAD into the model, we add an additional flow, Q_{rvad} . The flow into the pulmonary artery will then be given by

$$\frac{dV_{pa}}{dt} = Q_{pa} - Q_{pv} + Q_{rvad}. \quad (7.15)$$

RVAD will take fluid from the right ventricle or atrium, which results in either

$$\frac{dV_{rv}}{dt} = Q_{tr} - Q_{pvv} - Q_{rvad} \quad (7.16)$$

or

$$\frac{dV_{ra}}{dt} = Q_{sv} - Q_{tr} - Q_{rvad}, \quad (7.17)$$

respectively. The form of Q_{rvad} depends on the type of RVAD. The continuous flow RVAD only depends on the difference in pressure between the source (the right atrium or ventricle) and the pulmonary artery. Analytically, this can be approximated using a linear relationship [8], where Q_{rvad} is time independent. We also implement the pulsatile flow pump as described in Gohean *et al.* [9], which has demonstrated better performance compared to the continuous flow pumps [19], when properly synchronized. Now Q_{rvad} is time dependent and follows the formulation in Gohean *et al.* [9], given as

$$Q_{rvad}(t, \Delta P) = \begin{cases} \frac{2V_s}{T_l} \left(\frac{1}{2} - \frac{1}{2} \cos \left(\frac{2\pi(t-T_d)}{T_l} \right) \right) & \text{if } t \in [T_d, T_d + T_l], \\ 0 & \text{otherwise.} \end{cases} \quad (7.18)$$

where T_d is the time delay from the start of the cardiac cycle, T_l is the duration of the pulse, and V_s is the stroke volume in mL . The time, t , is normalized to the start of the cardiac cycle.

7.3 Results

We successfully implemented a ventricular hemodynamic model and simulated PAH based on data from Punnoose *et al.* [8] to study the effects of this aggressive dis-

ease on RV hemodynamics. The right and left ventricular hemodynamic parameters reproduced by our model are reported in Table 7.1.

Table 7.1: Stroke volume (SV), cardiac output (CO), and ejection fraction (EF) from the model for healthy, severe PAH, continuous RVAD treatment, and pulsatile RVAD treatment. Stroke volume is given in *ml* and cardiac output in *L/min*.

Condition	Left ventricle			Right ventricle		
	SV	CO	EF	SV	CO	EF
Healthy	72.722	4.363	0.717	72.722	4.363	0.687
Severe PAH	33.003	1.980	0.617	33.002	1.980	0.209
Continuous RVAD	46.594	2.795	0.646	22.840	1.370	0.155
Pulsatile RVAD	56.302	3.378	0.658	19.901	1.194	0.152

An important indicator of the severity of PAH is RV function and morphology [20]. Figure 7.3 shows pressure-volume loops (PV loops) corresponding to various severities of PAH. The shapes of the PV loops, which provide information on cardiac performance, load and coupling, change with progression of PAH. To simulate the different stages of PAH, the elastance, resistance and compliance parameters as well as the heart rate were modified based on values from previous studies [8]. As the disease progresses, resistance in the pulmonary artery increases, heart rate increases, and end-systolic elastance increases in the left ventricle, while it decreases in the right ventricle. For the LV, the normal shape of the PV loop is rectangular, whereas it is usually rounded for the RV. For both ventricles, the PV loops become more narrow, which is indicative of reduced stroke volume.

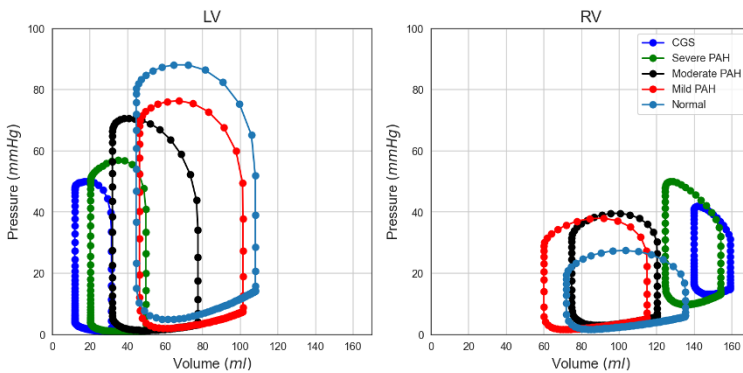


Fig. 7.3: PV loops for healthy and diseased hearts, from mild PAH to PAH-induced heart failure. Dark blue represents the most severe case, cardiogenic shock (CGS).

7.3.1 Sensitivity Analysis

A sensitivity analysis was a useful tool to determine the correlation between input model parameters and the resulting hemodynamic features of the system. By altering each model parameter, one at a time, we were able to better interpret the model outputs when the inputs were changed in PAH treatment simulations. The model behavior changed drastically when the pulmonary arterial resistance (R_{pa}) was altered, as illustrated in Figure 7.4. The R_{pa} values plotted correspond to 0.25, 0.50, 0.75 and 1 mmHg.s/mL. As R_{pa} increased (as in PAH), the stroke volume decreased substantially. The total mechanical energy generated by ventricular contraction also decreased, since the area encompassed within the PV loops (i.e., the stroke work) decreased with higher R_{pa} values. In addition to pulmonary arterial resistance, other parameters that also had a considerably high impact on the model outputs were RV end-systolic elastance and the exponential parameter (β) for the right ventricular end-diastolic PVR (7.5).

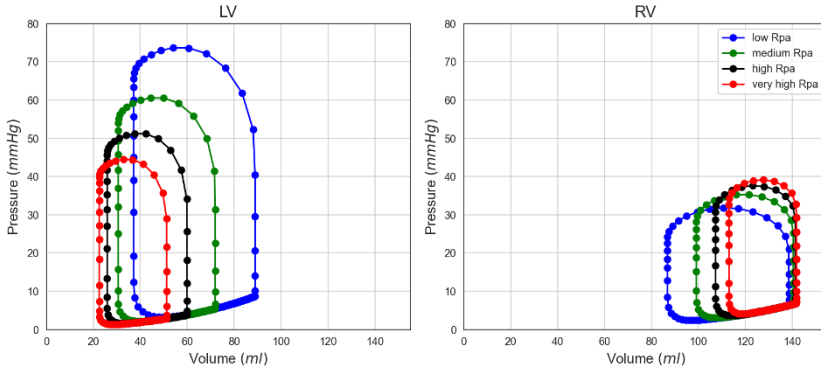


Fig. 7.4: PV loops for several degrees of pulmonary arterial resistance.

7.3.2 Ventricular Interaction and the Pericardium

As explained in subsection 7.2.2, we aimed to improve the realism of the model by including the interaction via the interventricular septum. We implemented three time-varying elastances with the same values used by Santamore *et al.* [11], and simulated different degrees of PAH by changing the values of resistance as in Punnoose *et al.* [8], and keeping the same values of elastance from Santamore *et al.* [11]. Figure 7.5 shows the different pressure-volume (PV) loops of the left and right ventricles when the interventricular interaction is turned on. The overall behavior of the PV loops is the same as those without interaction: there is a leftward shift of the LV PV loop and a

rightward shift of the RV PV loop with increasing PAH severity. This is likely due to the RV expanding and pushing against the LV, causing the right ventricular volume to increase and the left ventricular space to decrease, eventually leading to ventricular septum bowing. Compared to Figure 7.3, Figure 7.5 displays PV loops that shift more uniformly along an axis as severity increases. One possible explanation for this behaviour is the use of the same elastance values for the ventricular interaction simulations at each severity level. This behaviour, however, is not as strongly evident as in the previous simulations, which could be explained by the fact that we kept the same elastance from Santamore *et al.* [11] for each PAH degree, and because we used a combination of two parameter sets (Punnoose *et al.*[8] and Santamore [11]). We can still conclude that the introduction of the interventricular interaction does not lead to strong changes for this model. This result is in agreement with other studies that report small effects from the septum [11].

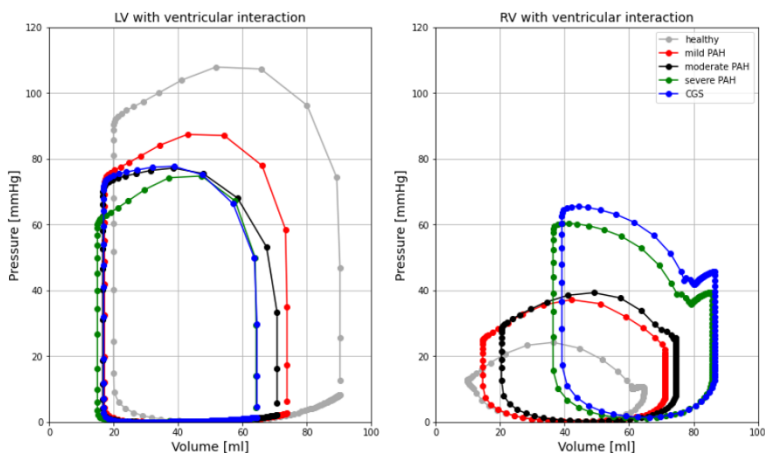


Fig. 7.5: Pressure-Volume loops with different degrees of PAH when the ventricular interaction via the septum is included. Dark blue represents cardiogenic shock (CGS).

Secondly, the presence of the pericardium represents an additional constraint to both ventricles. Figure 7.6 shows the effect of the pericardium in a healthy PV loop. When this element was added to our model, it lead to a reduction in the overall left ventricular stroke volume and an increase in the end-diastolic pressure of the right ventricle. The PV loop shifts slightly upward off the end-diastolic pressure-volume relationship (EDPVR), which is representative of the heart's ventricular passive compliance curve. In addition, the stroke volume is smaller and the peak pressure is lower in presence of pericardium. The stroke volume reduction observed in our model is consistent with physiological and clinical observations that the pericardium constricts heart dilation in the diastolic phase.

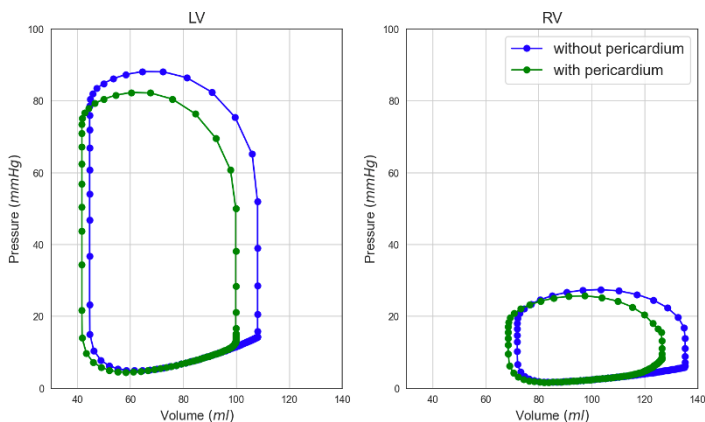


Fig. 7.6: Pressure-Volume loops of healthy condition with and without pericardium

7.3.3 Remodelling the Right Ventricle

Including the remodelling effects of the RV resulted in improved performance of the heart. Computing the change in contractility, as described by Equation 7.14, yielded improved model output for an increase in pulmonary pressure (Figure 7.7). Additionally, the arterial baroreceptor reflex system changed the model behavior in presence of PAH. The heart rate and contractility (heart rate effect shown in Figure 7.8), which are two parameters that have a significant effect on the model’s output, are adjusted by the baroreflex to control fluctuations in aortic blood pressure. Thus, impaired baroreflex control of the heart in PAH would typically contribute to worse outcome of the disease.

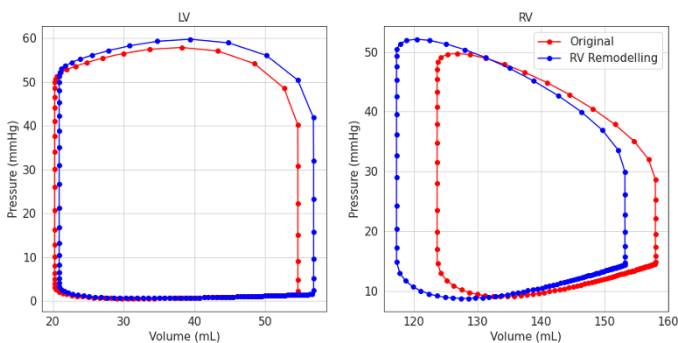


Fig. 7.7: Effect of remodelling the RV on the pressure volume relationship in the left and right ventricle.

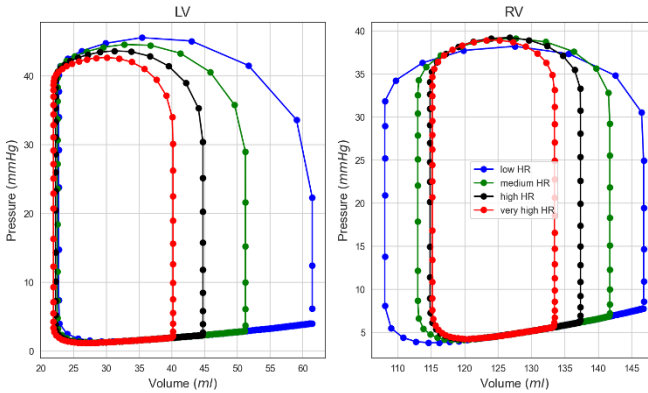


Fig. 7.8: Heart rate control, characteristic of baroreflex, has a high impact on the shapes of the PV loops.

7.3.4 Atrial Septostomy

Consistent with the left- and right-ventricular hemodynamics behavior observed in Punnoose *et al.*, our atrial septostomy defect simulation with resulting right-to-left shunt yields minimal leftward shifts in both the right atrial and right ventricular pressure-volume (PV) loops toward lower volumes and pressures [8]. Simultaneously, a rightward shift in the left atrial and left ventricular PV loops reflect increased filling pressures and end-diastolic volumes as shown in Figure 7.9.

Based on the results from our model, atrial septostomy significantly increased left ventricular stroke volume as a result of elevated end-systolic pressure and expanded end-diastolic volume. Meanwhile, the left ventricular end-diastolic pressure and end-systolic volume experienced no significant change with atrial septostomy. Collectively, these results indicate atrial septostomy causes an increase in left ventricular cardiac output with negligible change in the systemic vascular resistance. The right ventricular pressure, volume, and stroke volume remained largely the same with or without atrial septostomy and are thus determined to be minimally responsive to atrial septostomy treatment.

Prior to atrial septostomy treatment, the left and right atria are isolated, pressurized elastic chambers, with the right atrium having a higher pressure than the left atrium. The chamber pressure values are within reasonable ranges of 1 to 7 mmHg for the right atrium and 1 to 6 mmHg for the left atrium, as the atria are low pressure chambers meant for gathering blood from veins. After atrial septostomy treatment, however, we observed an increase of the end-systolic pressure and the end-diastolic volume in the left atrium as well as a slight decrease in the right atrium end-systolic pressure and end-diastolic volume. This is likely due to the two atria being connected via the atrial septal defect post-surgery, driving the pressures in the left and right atria to an equilibrium.

Our model observed a decrease in interatrial pressure gradient. This is demonstrated in Table 7.2 by a 34% elevation in left atrial end-diastolic pressure to match an 11% decrease in right atrial end-diastolic pressure. This outcome aligns with our prediction that the two atrial chambers will reach a pressure equilibrium when two heart chambers are connected via the atrial septal defect.

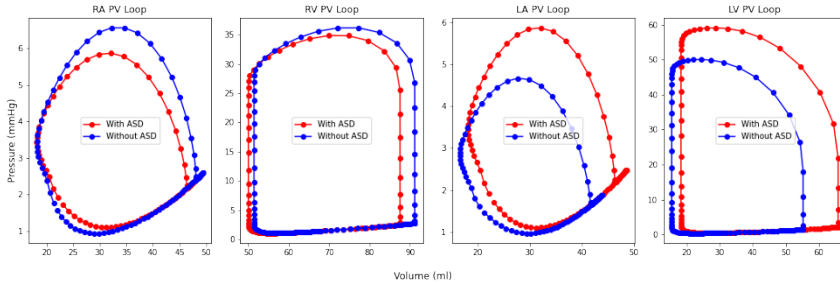


Fig. 7.9: Effect of atrial septostomy (ASD) on the pressure-volume relationship in each heart chamber.

Table 7.2: Heart chamber end-diastolic pressures (EDP) with and without atrial septostomy.

Heart Chamber	EDP, no septostomy (mmHg)	EDP, septostomy (mmHg)	Pressure Ratio
Right Atrium	3.142	2.795	0.8897
Right Ventricle	2.237	2.046	0.9147
Left Atrium	2.084	2.795	1.3415
Left Ventricle	1.160	1.687	1.4550

7.3.5 Right Ventricular Assistive Device

We find that our RVAD implementation behaves similarly to the one in Punnoose *et al.* [8] and Gohean *et al.* [9] (Table 7.1 and Figure 7.10). Simulated PAH reduced left ventricular cardiac output, stroke volume and ejection fraction (Table 7.1). This is evident in Figure 7.10, with a leftward shift in the left ventricular PV loops indicating left ventricular unloading. This is improved by pulsatile and continuous RVAD at a flow rate of 3.5 L/min from the right atrium or ventricle, indicated by a rightward shift in the left ventricular PV loops for both treatments, with the pulsatile flow performing better than the continuous flow RVAD (Figure 7.10 right). Conversely,

the right ventricular end-systolic and diastolic pressures increase in the simulated PAH. As shown in Figure 7.10 (left), a rightward shift in the PAH PV loop is seen, which is not improved by either the pulsatile or continuous RVAD.

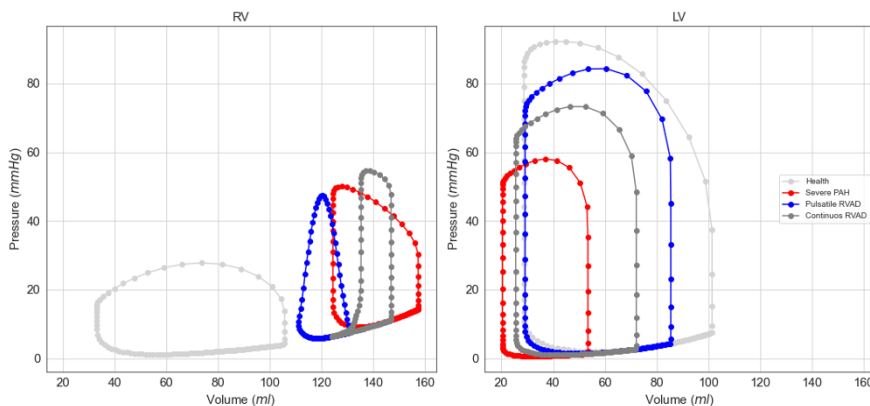


Fig. 7.10: Ventricular PV loops in healthy, severe PAH and treatment cases. The right ventricular PV loops for severe PAH shift to the left, but are partially recovered by pulsatile or continuous RVAD (left). Left ventricular PV loops in healthy, PAH and treated simulations of hemodynamics (right).

7.4 Discussion

In this study, we have modeled the influence of PAH on the mechanics of the circulatory system at various stages of the disease, based on the results from Punnoose *et al.* [8]. A sensitivity analysis demonstrated the significant dependence of our model on the resistance in the pulmonary artery, but many factors beyond resistance, such as contractility and stiffness, have an effect on the model too. To improve upon the base model, the addition of the interaction between the ventricular walls through the septum [11] and the effects of the pericardium [13] were included. We find a larger influence from the pericardium, which agrees with previous results [11, 13]. Further, we investigated long and short term adaptations of the heart to the increase in pressure of the pulmonary artery, as well as the effect of treatments to PAH. Specifically, the target of our computational study was to provide insight into how atrial septostomy and RVAD affect heart function [8, 9].

Our model exhibited hemodynamic effects of atrial septostomy similar to those observed in Punnoose *et al.* for all four heart chambers. This validated our implementation to study the effect of atrial septostomy on PAH-induced right-side heart failure [8]. Results from our simulation indicate that atrial septostomy indeed

restores the heart to a healthier functional state under the assumption of *ceteris paribus*, consistent with clinical observations. The end-diastolic pressure-volume relationship (EDPVR) on the PV loop represents the passive compliance of the heart ventricles. With atrial septostomy, the EDPVR remained the same in both the left and right ventricles, implying that the heart ventricular tissue stiffness is not affected by the treatment. The end-systolic pressure-volume relationship (ESPVR), which represents ventricular tissue contractility, remained the same for the left ventricle and decreased for the right ventricle with atrial septostomy treatment, denoting less contractility. The introduction of atrial septostomy in the interatrial septum likely decreased the right ventricle's need to contract to maintain the same cardiac output under PAH. Collectively, these data suggest that, while atrial septostomy does not change the myocardium intrinsic biomechanical properties, the surgical procedure seems to promote cardiac output, improve heart performance, and reduce heart failure symptoms. Summed together, our model provided results consistent with current clinical understanding of atrial septostomy effects on cardiovascular biomechanics, physiology, and literature.

The RVAD resulted in improved cardiac performance for a severe PAH setting by restoring cardiac output and ejection fraction in the LV. In our simulations, we observe better performance from the pulsatile flow compared to the continuous flow pumps. Despite the improved performance, the pulsatile flow pumps typically suffer from durability issues [9], so continuous pumps must be investigated too. Using this model, the influence of both types of pumps on the hemodynamics can continue to be studied in future research.

Our model was able to capture the effects of PAH on heart function, but there are some limitations to our work. Our ability to investigate the growth and remodelling was limited by the fact that we didn't account for the three-dimensional structural effects from the heart chambers, which alter the anatomy and behavior of the RV. To overcome this limitation, our framework could incorporate a 3D finite element model of the ventricles [21]. This extension of the lumped-parameter model would provide a more detailed characterization of ventricular mechanics as well as a more realistic representation of ventricular interaction via the septum. On the other hand, the limited literature sources with specific experimental data relevant to our study partly affect the accuracy of our results. There is significant variability in the biomechanical data between different cardiac studies, which makes it challenging to incorporate elements from multiple studies and unify them in one model [8, 11]. Conducting our own *in vivo* experiments could be useful to obtain more reliable parameters for the model. That is, experimental measurements would be a key next step to corroborate the results and develop an improved version of our model.

7.5 Conclusion

In this computational study, we have implemented a closed-loop lumped-parameter model of the heart and circulatory system for studying the cardiovascular adaptations

in the RV to PAH. We demonstrated that RVAD and atrial septostomy are effective treatments to improve left ventricular filling and cardiac output. We also extended our base model to account for direct ventricular interaction via the interventricular septum and the presence of the pericardium, showing that the pericardium has a larger effect relative to the ventricular interaction. Our present implementation lays the foundation for the addition of more components to the model that would augment its realism even further. We believe that highly complex computational models will continue to be critical to achieve our vision of dynamically simulating and characterizing ventricular mechanics in PAH.

References

1. Marc Humbert, Olivier Sitbon, and Gérald Simonneau. Treatment of pulmonary arterial hypertension. *New England Journal of Medicine*, 351(14):1425–1436, 2004.
2. S Frances, M Louis Handoko, and Anton Vonk-Noordegraaf. The unknown pathophysiological relevance of right ventricular hypertrophy in pulmonary arterial hypertension, 2019.
3. Deborah McCollister, Shannon Shaffer, David B Badesch, Arthur Filusch, Elke Hunsche, René Schüler, Ingela Wiklund, and Andrew Peacock. Development of the pulmonary arterial hypertension-symptoms and impact (pah-sympact®) questionnaire: a new patient-reported outcome instrument for pah. *Respiratory Research*, 17:72, 2016.
4. Mads Dam Lyhne, Jacob Gammelgaard Schultz, Peter J MacMahon, Faris Haddad, Mannudeep Kalra, David Mai-King Tso, Alona Muzikansky, Michael H Lev, and Christopher Kabrhel. Septal bowing and pulmonary artery diameter on computed tomography pulmonary angiography are associated with short-term outcomes in patients with acute pulmonary embolism. *Emergency Radiology*, 26(6):623–630, 2019.
5. Adriano R Tonelli, Vineesha Arelli, Omar A Minai, Jennie Newman, Nancy Bair, Gustavo A Hresi, and Raed A Dweik. Causes and circumstances of death in pulmonary arterial hypertension. *American journal of respiratory and critical care medicine*, 188(3):365–369, 2013.
6. John J Ryan, Jessica Huston, Shelby Kutty, Nathan D Hatton, Lindsay Bowman, Lian Tian, Julia E Herr, Amer M Johri, and Stephen L Archer. Right ventricular adaptation and failure in pulmonary arterial hypertension. *Canadian Journal of Cardiology*, 31(4):391–406, 2015.
7. Anna R Hemnes. Pulmonary arterial hypertension. <https://rarediseases.org/rare-diseases/pulmonary-arterial-hypertension/>, 2021. Last accessed 24 July 2022.
8. Lynn Punnoose, Daniel Burkhoff, Stuart Rich, and Evelyn M Horn. Right ventricular assist device in end-stage pulmonary arterial hypertension: insights from a computational model of the cardiovascular system. *Progress in cardiovascular diseases*, 55(2):234–243.e2, 2012.
9. Jeffrey R Gohean, Mitchell J George, Thomas D Pate, Mark Kurusz, Raul G Longoria, and Richard W Smalling. Verification of a computational cardiovascular system model comparing the hemodynamics of a continuous flow to a synchronous valveless pulsatile flow left ventricular assist device. *ASAIO journal*, 59(2):107–116, 2013.
10. Deborah Morley, Kenneth Litwak, Paul Ferber, Paul Spence, Robert Dowling, Bart Meyns, Bartley Griffith, and Daniel Burkhoff. Hemodynamic effects of partial ventricular support in chronic heart failure: results of simulation validated with in vivo data. *The Journal of thoracic and cardiovascular surgery*, 133(1):21–28, 2007.
11. William P Santamore and Daniel Burkhoff. Hemodynamic consequences of ventricular interaction as assessed by model analysis. *The American journal of physiology*, 260(1 Pt 2):H146–57, 1991.
12. Daniel Burkhoff and John V Tyberg. Why does pulmonary venous pressure rise after onset of lv dysfunction: a theoretical analysis. *The American journal of physiology*, 265(5 Pt 2):H1819–28, 1993.
13. Ying Sun, Mazen Beshara, Richard J Lucariello, and Salvatore A Chiaramida. A comprehensive model for right-left heart interaction under the influence of pericardium and baroreflex. *The American journal of physiology*, 272(3 Pt 2):H1499–515, 1997.
14. Hiroyuki Suga, Kiichi Sagawa, and Artin A Shoukas. Load independence of the instantaneous pressure-volume ratio of the canine left ventricle and effects of epinephrine and heart rate on the ratio. *Circulation research*, 32(3):314–322, 1973.
15. Nico Westerhof, Jan-Willem Lankhaar, and Berend E Westerhof. The arterial windkessel. *Medical & biological engineering & computing*, 47(2):131–141, 2009.
16. Theo Arts, Tammo Delhaas, Peter Bovendeerd, Xander Verbeek, and Frits W Prinzen. Adaptation to mechanical load determines shape and properties of heart and circulation: the circadapt model. *American Journal of Physiology-Heart and Circulatory Physiology*, 288(4):H1943–H1954, 2005.

17. Theo Arts, Frits W Prinzen, LH Snoeckx, Jons M Rijcken, and Robert S Reneman. Adaptation of cardiac structure by mechanical feedback in the environment of the cell: a model study. *Biophysical Journal*, 66(4):953–961, 1994.
18. KG Cornish, MW Barazanji, TANG Yong, and JP Gilmore. Volume expansion attenuates baroreflex sensitivity in the conscious nonhuman primate. *American Journal of Physiology-Regulatory, Integrative and Comparative Physiology*, 257(3):R595–R598, 1989.
19. George V Letsou, Thomas D Pate, Jeffrey R Gohean, Mark Kurusz, Raul G Longoria, Larry Kaiser, and Richard W Smalling. Improved left ventricular unloading and circulatory support with synchronized pulsatile left ventricular assistance compared with continuous-flow left ventricular assistance in an acute porcine left ventricular failure model. *The Journal of thoracic and cardiovascular surgery*, 140(5):1181–1188, 2010.
20. Manuel J Richter, Steven Hsu, Athiththan Yogeswaran, Faeq Husain-Syed, István Vadász, Hossein A Ghofrani, Robert Naeije, Sebastian Harth, Friedrich Grimminger, Werner Seeger, et al. Right ventricular pressure-volume loop shape and systolic pressure change in pulmonary hypertension. *American Journal of Physiology-Lung Cellular and Molecular Physiology*, 320(5):L715–L725, 2021.
21. Arnold D Gomez, Huashan Zou, Megan E Bowen, Xiaoqing Liu, Edward W Hsu, and Stephen H McKellar. Right ventricular fiber structure as a compensatory mechanism in pressure overload: a computational study. *Journal of Biomechanical Engineering*, 139(8):081004, 2017.

Open Access This chapter is licensed under the terms of the Creative Commons Attribution 4.0 International License (<http://creativecommons.org/licenses/by/4.0/>), which permits use, sharing, adaptation, distribution and reproduction in any medium or format, as long as you give appropriate credit to the original author(s) and the source, provide a link to the Creative Commons license and indicate if changes were made.

The images or other third party material in this chapter are included in the chapter's Creative Commons license, unless indicated otherwise in a credit line to the material. If material is not included in the chapter's Creative Commons license and your intended use is not permitted by statutory regulation or exceeds the permitted use, you will need to obtain permission directly from the copyright holder.

